SENSING AND ACTUATION OF BEAD-TAGGED BIOMATERIALS ON STANDARD CMOS SUBSTRATES

By

Faisal T. Abu-Nimeh

A DISSERTATION

Submitted to
Michigan State University
in partial fulfillment of the requirements
for the degree of

DOCTOR OF PHILOSOPHY

Electrical Engineering

2011

ABSTRACT

SENSING AND ACTUATION OF BEAD-TAGGED BIOMATERIALS ON STANDARD CMOS SUBSTRATES

By

Faisal T. Abu-Nimeh

Magnetic molecular-level sensing and manipulation are emerging as lab-on-chip platforms. These platforms entail low-cost, low-power, high efficiency, and portable implementations. Biomaterials are usually attached to magnetic beads and used in bio-analysis applications such as sorting, counting, purification, and assembly. Some of the potential applications are 2D biological or artificial tissue assembly at the micro-scale level.

Here, we present the design and demonstration of a self-contained device for sensing and manipulating biomaterials tagged with magnetic beads. The core elements of the device consist of all-integrated programmable magnetic coil arrays for pseudo-parallel sensing and actuation, which are capable of maneuvering small (bead-bound) bio-objects individually and larger ones collaboratively. Our design does not require any external magnetic sources. It relies on the magnetic field generated by planar on-chip coil arrays. The coil arrays are selectively and dynamically controlled. Each element, composed of the coil and its logical control circuitry, can detect bio-objects in the order of 1μm diameter, or manipulate them using eight-level programmable AC or DC magnetic fields. All array sensing and actuation components are shared and multiplexed to reduce the overall imprint. The components are isolated and tuned to work at 900MHz by incorporating high-speed switching (up to 40MHz) for seamless pseudo-parallel execution.

In addition, we present a new and unique on-chip biomedical proof-of-concept application. Adopting trends in neuroscience, we employ the magnetic beads to initiate and elongate

neuronal axons in vitro *on-chip*. This application domain will assist in better understanding and studying the process of neuroregeneration, propel future clinical applications, and provide the foundation of techniques needed to wire "neuronal circuits" using living cells.

To my family.

ACKNOWLEDGMENTS

I would like to express my sincere gratitude to my parents, my wife Zaina, and my family who have provided me with everything I needed and have been at my side throughout this endeavor. I am deeply thankful for their support and love, without that I certainly would not have been able to accomplish and finish this work. And thanks to my daughter Raneem who showed me a new perspective on life.

First, I would like to thank my committee members. Most importantly Prof. Fathi Salem, my advisor, whom I worked with since my capstone project during my bachelor's degree. His kind personality and vast knowledge gave me the energy to continue this labor to the end. Thanks to Profs. Mason, Xing, and Chakrabartty for the discussions and support. Also, I would like to thank Prof. Kyle Miller, who enlightened me about neuronal cultures and gave me the opportunity to have a hands-on experience in magnetic beads.

Second, I would like to thank Miller's lab members, especially, Phillip Lamoureux, who constantly provided me with the things I needed for my on-chip biological experiments. Thanks to Prof. Wen Li for allowing me to use her lab equipment to conduct my experiments. Also, I am grateful to AMSaC, Microtechnology, and AMI lab members for their discussions and help throughout my journey.

Finally, I would like to thank everyone who helped me throughout this journey. I couldn't list all the names here, however, It would have been impossible to reach this point without their support. I am very grateful to all who gave me part of their time, knowledge, and help.

TABLE OF CONTENTS

LIST OF TABLES

LIST OF FIGURES

Chapter 1

Introduction to Biomedical designs on standard CMOS substrates

1.1 Introduction

Conventional micro and nano magnetic particles have become a unique tool for analyzing biomaterials. Since the mid 1800's several USA patents like [1, 2, 3] appeared on magnetic separation and arrogation. Most techniques used until the early 1990's were based on bulky equipment and large magnetic particles. The introduction of nano superparamagnetic beads few decades ago revolutionized the process of biomedical analysis and became a new tool in numerous scientific and clinical applications, e.g., cell counting, protein isolation, infection detection, sorting, in-vitro diagnostic (IVD) immunoassays, and more. During the same period of time, electronic design and fabrication processes became more advanced and utilized complementary metal-oxide-semiconductor (CMOS) to drive low-cost, low-power, and high efficiency chips.

In this thesis, we design, develop, and test a platform based on standard CMOS technology to create a high-precision, economical, and high throughput lab-on-chip (LOC) device suitable for sensing and actuation of bead-tagged biomaterials. The platform is also utilized to demonstrate a unique biomedical application, on-chip axonal elongation.

1.2 Literature Review and Contributions

1.2.1 Review of the state-of-the-art

Current state-of-the-art designs of magnetic bead sensing and actuation include capillaries or microfluidic channels and pumps [4, 5, 6] to guide the biomaterial samples into chambers or fenced regions for manipulation. Lee et al. [4, 7, 8] started with a simple ring trap and a matrix of wires to trap and move a single bead to a desired location, then they designed a hybrid system using a Polydimethylsiloxane (PDMS) microfluidic structure on top of a CMOS die to sequentially move multiple beads to a certain location using an 8x8 coil array. Also, [9] introduced a device that is capable of moving a collection of beads, enclosed by capillaries, using a line of integrated coils. Other approaches, e.g., [10], used mechanical structures such as spin valve arrays where the magnetic bead can be trapped, or use micro-magnetic-tweezers to guide a bead through a pre-defined path, e.g., [11]. Additionally, [12] built a line of coils on a Printed Circuit Board (PCB) device. Their device also used a microfluidic channel on top of the PCB to guide the beads from one coil to another.

The main limitation in these implementation is that there is no capability of (pseudo-)parallel movement of beads. Prior work have demonstrated only sequential bead movement (at most every 10-20 m seconds [4], which means other beads would change position over

Table 1.1: Comparison with current state-of-the-art in magnetic bead manipulation

	This Work	[4]	[8]	[9]	[12]
Current	40mA	20mA	11mA	40mA	400 A/mm^2
Source	Shared	Shared	Dedicated	-	-
Coil	80μm	20μm	25μm	400μm	3.5mm
Array	8x8	8x8	5x5	Line	Line
Bead	2.8μm	8.5μm	8.5μm	15μ	1μm
Technology	CMOS 0.5μm 3M2P	CMOS 0.18μm 6M1P	SiGe 3M	CMOS 0.35μm 4M2P	PCB
Manipulation	Multiple Pseudo-Parallel	Multiple Sequential	Single	Single	Single
Freq.	40MHz	50Hz	-	-	-
Force	600pN	40pN	50pN	fN	-
Package	Standard	μFluidic PDMS	μFluidic PDMS	μFluidic	μFluidic

the coil array). In this work, we apply a force to multiple beads (pseudo-)simultaneously in the order of (1/40M=) 250n seconds. Thus one can move multiple beads at several locations (pseudo-)simultaneously. Additionally, we distinguish our design from the aforementioned present-state-of-the-art, as summarized in Table 1.1, by introducing a new programmable manipulation platform using high-speed switches on a closely stacked coil array, which can simultaneously transport and move magnetic beads in a pseudo-parallel fashion. The coils are carefully laid out and stacked to generate overlapping magnetic fields, using larger DC currents, to assure coil-to-coil transport. And non-overlapping fields, using smaller DC currents, to assure valid trapping. Additionally, the pseudo-parallel manipulation platform allows the programmable array to individually move multiple small objects or collaboratively transport larger ones.

On-chip magnetic bead sensors usually require an external magnetic source to generate the reference magnetic field [13, 14]. Or they use the CMOS Hall effect to sense magnetic particles using "Hall" arrays and chambers [15, 16]. Additionally, [17] uses a photo-diode configuration to detect beads lying above the center of the coil. The main limitation of this setup is that the beads are detected only when they pass through a very small region (namely, center of the coil). Moreover, [18, 19, 20] starts with a single LC cross coupled oscillator to detect beads and expands it to an array of sensors by replicating the active transistors for four sensing sites. In this work, we share a single pair of cross coupled active transistors across the entire array by utilizing high speed switches for pseudo-parallel sensing.

Finally, state-of-the-art designs have been limited to sensing only [18], actuation (manipulation) only [4], or designs which require a user intervention or special micro-fluidic packaging. Here, we present programmable compact coil arrays for dynamic pseudo-parallel sensing and manipulation by multiplexing a shared core (specifically the core consist of cross-coupled active transistors for enabling oscillation and sensing, a DC current source, and an AC currentsource). All components of our design are integrated on the same die and used for sensing and/or actuation without the need for specialized post processing, magnetized materials, or specialized packaging. Our integrated platform introduces new possibilities to sense and manipulate [21, 22] multiple small magnetic particles, at different spatial locations, in pseudo-parallel fashion or large single particles with a collaborative execution scheme of the array of coils. Each "cell" in the array can generate 8 programmable magnetic field levels or sense magnetic beads with a diameter of at least 1μm; thus, giving the user more functionality and flexibility in a unified standard package that does not require microfluidic pumps and structures. Nevertheless, It is possible to integrated PDMS structures on top of the simplified packaging if the targeted application requires such setup.

1.2.2 Main contribution of this thesis

The list below itemizes the contributions which differentiates this work from current state-of-the-art:

1. Tri-mode lab-on-chip device capable DC actuation, AC actuation, and RF sensing of magnetic beads using a shared micro-coil array and shared DC, AC, and RF cores.
2. Pseudo-parallel manipulation scheme using high-speed switches (up to 40MHz) for simultaneous maneuvering and transport of magnetic beads.
3. Novel biomedical application: on-chip axonal elongation using magnetic beads.
4. Simplified open-cavity design to alleviate micro-fluidic complexity and facilitate on-chip biological cultures studies.

1.3 CMOS scalability, reliably, and compatibility

The main driver of the Integrated Circuits (ICs) industry are microprocessor chip makers who mainly target consumer electronics, personal computers, laptops, and smart phones. However, due to their mass production, availability, and price competitiveness, CMOS dominated the semiconductor business for the past two decades. As a result, the prices of CMOS devices went down as their production went up. Consequently, other industries including biomedicine have been taking advantage of this well established technology and utilized its scalability, reliability, and compatibility to deliver miniaturized biomedical instruments for the masses.

1.3.1 Scalability

Feature size and channel length in CMOS have been shrinking steadily. According to the so-called Moore's law, the number of transistors in integrated circuits approximately doubles every two years. The largest semiconductor chip maker Intel, e.g., has kept up with this pace for the past 40 years. Fig. 1.1 shows the feature size of the transistor verses the production year. As the number of transistors double every two years more functionality is being added to integrated circuit chips, thus, making them more capable. This makes CMOS technology more appealing to other industries like biomedicine.

Biomedical applications are quite sophisticated they often require a direct interface with organic matter such as cells, chemical compounds, or living tissue. Such requirements not only demand a high degree of circuit intelligence but also precise power, temperature, and size specifications. Using CMOS allows us to exploit the large number of transistors available on a single die to increase functionality, drive down the cost while meeting specifications and demands.

Most digital designs can be trivially reduced in size using common frequency and channel scaling techniques without the need to completely redesign the integrated circuitry. On the contrary, analog designs don't follow the same trend and often require further design considerations and adjustments. Consequently, they don't scale as easy as their digital counter parts. In biomedical applications, mixed signal (Analog/Digital/RF) designs are dominant due to the sophisticated interface between the living cells and the electronics connected to them. Thus, CMOS scaling can be utilized in the digital portion of the design.

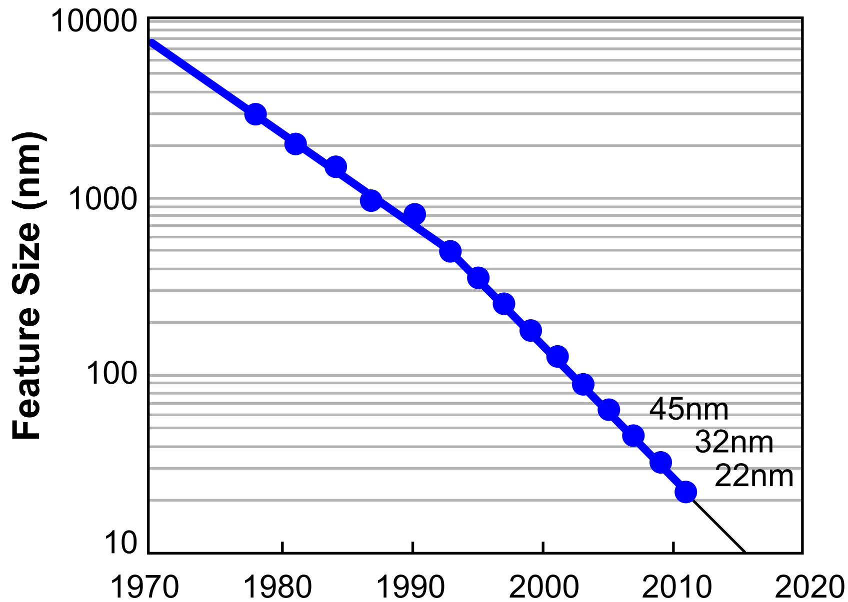

Figure 1.1: The decreasing rate of transistor dimensions is 0.7x every two years. For interpretation of the references to color in this and all other figures, the reader is referred to the electronic version of this dissertation.

1.3.2 Reliably

Most biomedical applications require stable functionality over a very long period of time. For example, heart pacemakers are expected to live seven to ten years depending on the implant. Thus, lifetime and longevity are crucial aspects when considering such devices. CMOS has proven itself over the years to produce reliable high-yield chips. Most devices designed in CMOS have an average life span of ten years. The most common reasons which cause physical failure in CMOS chips are electromigration, time-dependent gate oxide breakdown (TDGOB), and hot carriers injection (HCI).

Electromigration is the gradual displacement of the ions in a conductor as a result of the current flowing through it. This effect is very important in our application because of the use of on-chip coils where each coil is supplied with a variable electrical current to generate a distinct magnetic field. When high current densities are used, integrated circuits are more likely to fail earlier than expected. Using a mathematical model developed by Jim Black of Motorola, one can predict the mean time to failure (MTTF) for a semiconductor circuit due to electromigration. The model is known as Black's equation[23]:

$$MTTF = Aj^{-n}e^{\left(\frac{Q}{kT}\right)}, \tag{1.1}$$

where A is a predefined constant based on experimental data, j is the current density, n is a model parameter, Q is the activation energy, k is the Boltzmann constant, T is the temperature in Kelvins. Therefore, careful measures and design techniques should be followed when using large current densities j to avoid electromigration. It is apparent that current density j and the temperature T are the main factors in the design process which affect electromigration. Therefore, for an interconnect to remain intact at high temperatures, the maximum current density of the conductor must necessarily decrease. These considerations are discussed in Section 3.2.1.

Time-dependent gate oxide breakdown, which is also referred as Time Dependent Dielectric Breakdown, is the failure where the gate oxide breaks down as a result of long-term low electric field. The breakdown is caused by the development of a conducting path through the gate to the substrate due to electrons tunneling as a result of operating MOS at a voltage higher than the one specified by the foundry. When there is a conducting path between the gate and the substrate, it is not possible to control the current flow between the drain and source by means of the gate voltage; consequently, creating faulty logic in the circuit which renders the (biomedical) device useless. Hu et al. [24] created a mathematical model which fits the TDGOB of several devices:

$$t_{BD} = \frac{t_{BD1} \cdot t_{BD2}}{t_{BD1} + t_{BD2}}, \tag{1.2}$$

where t_{BD1} and t_{BD2} are the lifetimes predicted by the E-model (thermochemical, the breakdown occurs due to field enhanced bond breakage) and the 1/E model (hole-induced breakdown) respectively and can be approximated as follows:

$$t_{BD1} = t_1 \cdot \exp\left(-\gamma \cdot E_{ox}\right), \tag{1.3}$$

and

$$t_{BD2} = t_2 \cdot \exp\left(G/E_{ox}\right), \tag{1.4}$$

all fitting constants (t_1, t_2, and γ) can be obtained from [24]. Accordingly, the design has to adhere to foundry design rules for gate voltages and proper operating temperature to guarantee proper life span for the device. It is important to note that these approximate models start deviating when the thickness of the oxide becomes very thin e.g. 5nm. Therefore, one cannot engineer a device to fit these models; thus, the best practice is to follow the guidelines supplied by the process developer and foundry when setting voltage specifications.

Hot carrier injections are electrons or holes which have gained high kinetic energy while being accelerated by a strong electric field in a MOS transistors. Because of this high kinetic energy, hot carriers could get injected in places where they should not be, thus, making the transistor behave different that expected. The transistor's transconductance slowly degrades causing the threshold voltage to change, hindering it from forming a channel in the drain region. This causes digital circuits (as well as threshold sensitive analog circuits) to fail prematurely due to logical errors caused by the threshold shift. It is difficult to mathematically model hot carrier damage rates. Most models are not sufficiently accurate in predicting such rates. The reader is referred to [25] for more details on HCI and other reliability mathematical models.

1.3.3 Compatibility

There are several points where CMOS has to be compatible with biomedicine. First, low power: when CMOS was initially introduced, the complementary logic made it so appealing because an engineer had to design half the circuit and the other half is simply the complement. This methodology also allows half the circuit to be switched on while the other is completely off. As a result, the power is substantially reduced compared to other technologies like BJTs (Bipolar junction transistors). Low power designs make it possible to create devices that can run for years without replacing the power source, e.g., battery. Moreover, they can be designed to harvest power from their surroundings without requiring bulky or additional components; thus, making them very attractive to the biomedical applications.

Second, biochemical compatibility: most CMOS substrates are protected and passivated with Silicon Dioxide (SiO_2) and Silicon Nitride (Si_3N_4). These two chemical compounds are employed to create biocompatible platforms for growing cultures[26, 27] or create implantable devices[28, 29].

In this work, we compare growing neuronal cultures on plain silicon nitride and on pretreated silicon nitride. We also measure the growth yield and choose a suitable protocol for subsequent experiments. Fig. 1.2 shows an image of neuron cultures created from drosophila embryos grown on a CMOS coil array. Section 6.3 details the process of growing neurons

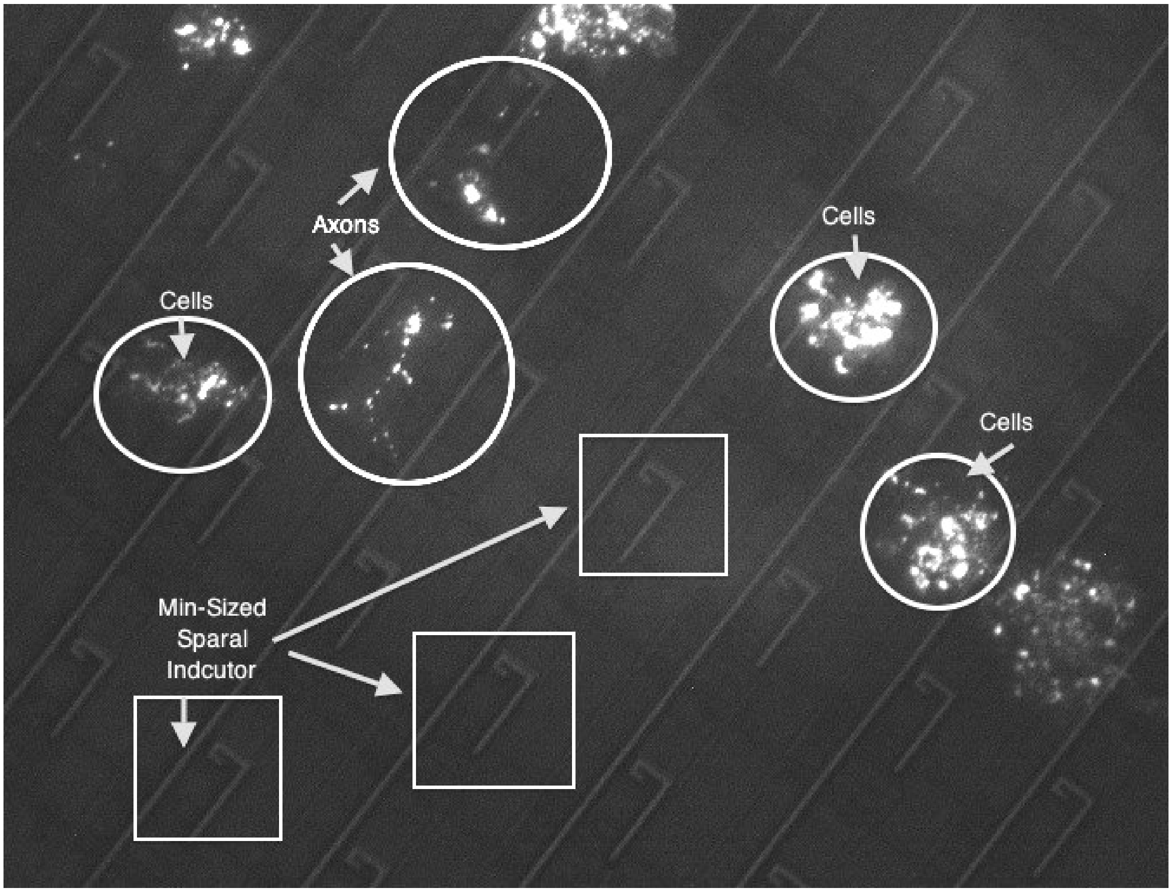

Figure 1.2: Drosophila neuronal cultures grown on a CMOS chip treated with polyornithine has a higher yield than neurons grown on plain silicon nitride. The image was taken 24 hours after placement on chip.

on-chip and how to provide a more compatible substrate for better yield.

1.4 Point-of-Care testing and personalized medicine

Point of care testing (POCT) is medical testing near the site of patient care. It allows quicker medical response, convenience, and better results. Most POCT devices are built to be mobile, disposable or reusable, and support a wide range of tests without the need for bulky laboratory equipment, see Fig. 1.3[30]. The key objective of POCT is to provide economical and quick devices that can be deployed in remote areas or any place where sophisticated

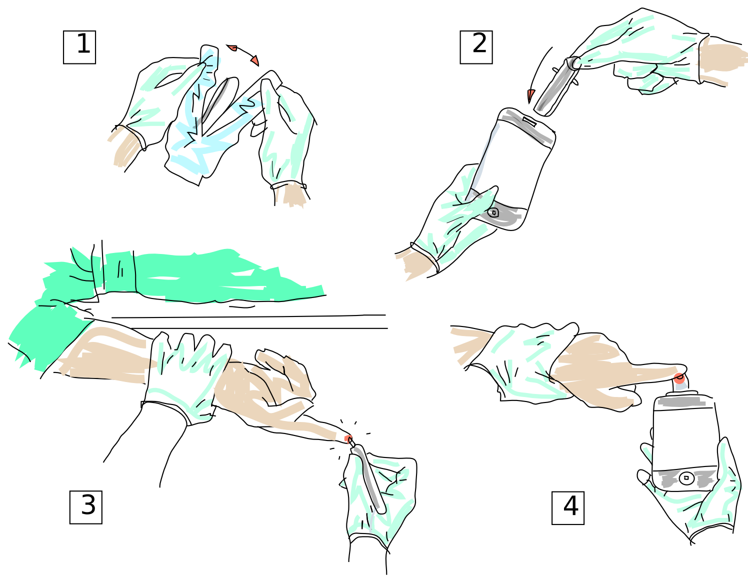

Figure 1.3: 1. A disposable strip is used by a health provider. 2. The strip is calibrated using a portable hand held device. 3. Point of care testing at the site of the patient is conducted. 4. Real-time results and measurements are reported.

lab equipment are not present or available at hand. As a result, the proper treatment can be implemented at the same time and place, leading to an improved clinical outcome for the patient and the medical provider. A good example of POCT and personalized medicine is the use of portable blood glucose meters, which allow diabetic patients to actively monitor their blood sugar at their convenience without the need to leave their homes or see a specialist. Consequently, achieving faster results, better care and awareness, and lower cost. Designing such devices require small footprint, low power, low cost, and high throughput. In this work, we utilize the CMOS features discussed in 1.3 to create a lab-on-chip platform capable of detecting and manipulating magnetic bead-tagged biomaterials. This device can be used for research and development or clinical studies.

1.5 Thesis Organization

The thesis is organized as follows: Chapter 1 introduces the overall technical subject, lists CMOS features, example applications, challenges, and motivation. A summary of current state-of-the art is also discussed in this chapter. In chapter 2, we describe and introduce magnetic beads, list their physical and chemical properties, and the forces acting on a magnetic bead suspended in a fluidic sample. Chapter 3 is where we introduce our manipulation and sensing devices with supportive simulations and lab experiments. Each component is explained and discussed separately in a dedicated section to show our scientific contribution at the circuit and at the system levels. In Chapter 5, our customized packaging method is summarized and supported with a lab experiment to show its effectiveness. Chapter 6 demonstrates and introduces a unique biomedical application "on-chip axonal elongation" using magnetic beads where our device is used to accelerate the growth rate of an axon in vitro. Finally, Chapter 7 lists our contributions and lays out future steps needed to improve this effort.

Chapter 2

Superparamagnetic Beads

2.1 Introduction

Micro- and nano-sized magnetic particles have been used extensively in biomedical analysis in recent years due to their compactness, versatility, and reliability [31, 32, 16, 33, 34]. Most of the time, the application of interest imposes the bead's size, coating, and iron mass content.

First, magnetic bead diameters come in different sizes ranging from 100s [35] of nano meters to a few micro meters [36]. However, the target biomaterial size (e.g. protein, blood cell, etc) decides the appropriate diameter of the bead. Second, the iron mass content (e.g. 15.26 mg/mL for the Adembeads [37]) is determined by the amount of force needed to maneuver the biomaterial, for example, the more iron content the better the magnetic manipulation. Lastly, the biochemical coating provides flexibility in terms of binding to different antibodies, peptides, etc. Therefore, the targeted bio-material, the surrounding (fluidic) medium, and the substrate help identify the kind of coating to be used in an experiment or an application. These characteristics have a direct impact on the forces affecting the magnetic beads in an aqueous environment.

The magnetic beads used and/or modeled in this work are Dynabeads MyOne (diameter $1\mu m$), Dyabeads M-280 ($2.8\mu m$ diameter), Dyabeads M-450 ($4.5\mu m$ diameter), and AbC^{TM}($6\mu m$ diameter). The selection criteria were based on the size and the iron mass content of the bead, where the target bio-material size was around 1 to $20\mu m$ and the forces needed were in the nano- and pico- newtons ranges.

2.2 Physical and chemical properties

Typical superparamagnetic micro and nano spheres (beads) are made of Silicon Dioxide (SiO_2) or polystyrene matrices and iron oxide crystals. They are usually synthesized with different compositions which include magnetite (Fe_3O_4), maghemite (Fe_2O_3, γ-Fe_2O_3), or ferromagnets like Fe and Co.

There are several methods and protocols [38, 39, 40] to create coated magnetic beads. The most common methods are coprecipitation and thermolysis. There are other methods like microemulsion and hydrothermal which are used less nowadays. First, coprecipitation is done by adding a base under inert atmosphere around room temperature to aqueous Fe^{2+}/Fe^{3+} salt solution to get iron oxides like Fe_3O_4 or γ-Fe_2O_3. However, the challenge in this process is to control the particle size and achieve an accepted particle distribution. Second, thermolysis is thermal decomposition caused by heat which breaks chemical bonds in the compound (organometallic) undergoing decomposition.

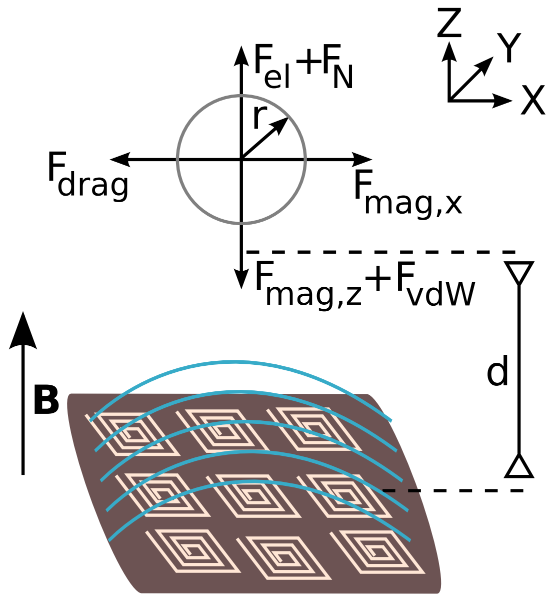

Figure 2.1: Forces affecting beads in aqueous experiments. The gravity force is not shown and it is in the same direction as F_{mag}, F_{mag} is the magnetic force, F_N is the normal, F_{el} is the electrostatic double layer , F_{vdW} is the van der Wals, and F_{drag} is the drag force.

2.3 Forces

Now we introduce and discuss the major forces, shown in Fig. 2.1, a bead encounters in aqueous experiments:

2.3.1 Gravity

The main force responsible for sedimenting the magnetic bead is the gravitational force. This force is simply given as

$$F_G = mg, \tag{2.1}$$

where m is the mass of the bead, g is the gravitational acceleration.

2.3.2 Magnetic Force

A (magnetic) bead in a magnetic field, say $\vec{H}$, becomes magnetized and acquires a moment $\vec{m}$ given by

$$\vec{m} = V_m \vec{M} = V_m(\Delta\chi \vec{H}), \tag{2.2}$$

where V_m is the volume of the bead, $\vec{M}$ is known as the magnetization of the bead, and $\Delta\chi$ is the difference in the relative magnetic susceptibility between the magnetic bead and the surrounding medium. It is important to note that the bead's magnetization becomes saturated in practice, and thus the magnetic moment saturates independent of further increases in the applied field ($\vec{H}$). As a result, the amount of magnetic force generated by passing DC currents through the coils is limited by the magnetic moment of the bead.

Now the magnetic force acting on the (magnetized) bead is due to the field generated by the on-chip spiral coils. We begin with the magnetic potential energy, say U, for trapping a magnetic bead, given as (see [41])

$$U = -\frac{1}{2}\vec{m} \cdot \vec{B}, \tag{2.3}$$

where $\vec{m}$ is the magnetic moment as defined in (2.2) and $\vec{B}$ is the (external) magnetic flux density. The moment of (2.2) is re-expressed as

$$\vec{m} = \frac{V_m(\Delta\chi)}{\mu_0}\vec{B}, \tag{2.4}$$

where μ_0 is vacuum permeability, and $\vec{B}$ is the assumed acquired magnetic field by the bead. The magnetic force is thus defined as the spatial gradient descent of the potential energy, i.e.,

$$\vec{F}_m = -\nabla U = \frac{1}{2}\frac{V_m(\Delta\chi)}{\mu_0}\nabla B^2, \tag{2.5}$$

where B^2 is the dot product of the magnetic field vector with itself. Note that, when the relative susceptibility is positive the generated magnetic force acts in the negative direction of the gradient.

2.3.3 Drag Force

Any object moving through a fluid encounters a hydrodynamic resistance which opposes its motion. This resistance is called the drag force, and it is directly related to the viscosity of the medium the object is traveling in. Assuming that the bead is a perfect sphere moving in a medium with a low Reynolds number (R_0), the drag force is approximated as

$$\vec{F}_d = -6\pi r_h \eta \vec{v}_s \cdot f_D, \tag{2.6}$$

where r_h is the hydraulic radius of the bead, η is the dynamic viscosity of the fluid, $\vec{v_s}$ is the velocity of the bead relative to the fluidic environment, and f_D is the drag coefficient. Temperature plays a significant role in keeping the viscosity of the medium constant. The dependence of viscosity on temperate can be captured using different models [42, 43]. Consequently, the application of interest, which determines the medium and the targeted bio-sample should enforce careful temperature control in order to maintain the pre-calculated viscosities and drag forces.

The drag coefficient has a significant effect on the bead while it is moving near a solid wall (i.e. the substrate surface of the chip). An expression introduced in [44] models the relationship between the drag coefficient, the radius, and the (minimum) distance (say, d) between the surface and the bead as

$$f_D = \left[1 - \frac{9}{16}\left(\frac{r_h}{r_h + d}\right) + \frac{1}{8}\left(\frac{r_h}{r_h + d}\right)^3 - \frac{45}{256}\left(\frac{r_h}{r_h + d}\right)^4 - \frac{1}{16}\left(\frac{r_h}{r_h + d}\right)^5\right]^{-1}. \tag{2.7}$$

It is noted that the drag coefficient equals 1 far away from any surface, and increases as it approaches a surface. To capture the significance of this coefficient, assume that the distance (d) between the bead and the surface approaches zero; as a result of that, the drag force increases more than twofold.

Using this expression and (2.6), one can estimate the expected amount of drag force which would hinder the movement of the bead/bio-material prior to the fabrication of the CMOS coil array. Therefore, the specifications of the coil (i.e. the number of turns and track width) and DC circuity (i.e. the amount of current passed through the coil) have to be adjusted carefully to overcome this drag force. Other parameters like the radius of the bead and its velocity can be adjusted by changing the type of bead and/or microfluidic flow.

2.3.4 DLVO Forces

DLVO forces result from a theory named after Derjaguin, Landau, Verwey, and Overbeek [45, 46]. They separately suggested that interactions between small particles in aqueous solutions can be explained by the exchanges between two forces: (1) the van der Waals force [47] which is the total dipole-dipole force, dipole-induced dipole force, and dispersion forces and (2) the electrostatic double-layer force [48] where two parallel layers of charge surround the surface of the chip. The first layer is the surface charge and it comprises ions adsorbed directly onto the object due to chemical interactions. The second layer is made of ions attracted to the surface charge by the electric or coulomb force, thus, isolating the first layer.

First, the van der Waals force entails biochemical bindings (i.e. of antibodies) as a form of non-covalent bonds by means of Lifshitz-van der Waals interactions [49]. Additionally, the van der Waals energy interaction between a spherical shape (i.e the bead) and a flat surface (i.e. the surface of the chip) is approximated by

$$W = -\frac{Ar_h}{6d^2}, \tag{2.8}$$

where A, the Hamaker constant of the bead, is dependent on the material of the bead, the surface, and the medium. d is the (minimum) distance away from the surface of the chip (in the vertical z-direction $\hat{e}_z$). The van der Waals force is modeled as

$$F_{vdW} = W \left[\frac{1}{1 + 14d/\lambda_{ret}} \right] \cdot \mathbf{\hat{e}_z}, \tag{2.9}$$

where λ_{ret} is the characteristic wavelength of interaction [50]. It becomes significant when the beads are close to each other or to the chip's surface.

The second DLVO force is the electrostatic force. It is induced through adsorption of ions present in the liquid and dissociation of surface groups (silanol groups for glass or silica surfaces). When the double-layers of two approaching objects overlap (e.g., bead and chip's surface) an electrostatic force is created; it can be either repulsive or attractive [51, 52]. This force can be written as

$$F_{el} = \frac{2\pi\epsilon\kappa r_h}{1-\exp(-2\kappa d)}\Big[2\psi_s\psi_b\exp(-\kappa d) \mp \left(\psi_s^2+\psi_b^2\right)\exp(-2\kappa d)\Big]\cdot\hat{\mathbf{e}}_{\mathbf{z}}, \tag{2.10}$$

where ϵ is the permittivity of the fluid medium, ψ_s is the surface potential of the chip, ψ_b is the surface potential of the bead, and κ is the Debye-Hückel inverse double-layer thickness, which is defined as

$$\kappa = \left(\sqrt{\frac{\epsilon kT}{2000 N_A e^2 i}}\right)^{-1}, \tag{2.11}$$

where k is the Boltzmann constant, T is the thermodynamic temperature in Kelvins, N_A is the Avogadro constant, e is the charge, and i is the ionic strength of the electrolyte medium (Mole/l).

The van der Waals forces are initially attractive, however, the electrostatic double-layer force is either attractive or repulsive depending on the surface charge. A net repulsive DLVO force is desired between the beads and the surface of the chip to ensure stability of the colloid[53]. Lack of such stability might result in beads aggregations and/or adhesions to the chip's surface. Finally, the ionic strength i and the pH of the medium are important in order to predict the DLVO forces affecting the beads. For example, in order to successfully grow cell cultures (e.g. neurons) on the surface of the chip, the medium surrounding the culture will mandate a very limited range of pH and ionic strengths. Consequently, these limitations will make the coating of the beads and the surface of the chip as one of the major issues to be addressed in order to grow a successful culture as well as diminish undesired DLVO forces.

2.3.5 Other Forces

There are also a collection of forces which cause random Brownian motion. Brownian motion causes the random movement of small objects while they are suspended in liquid. This motion should be taken into account when trapping or tethering magnetic beads at a specific location using on-chip coils. In this scenario, the magnetic bead "drifts away" or diffuses from the point of interest if there is no magnetic force trapping it in place (e.g, when the coil is momentarily switched-off to save power or actuate at another spatial location). Therefore, to estimate the random distance traveled by the bead and the amount of time it takes the bead to escape from the magnetic trap, we compute the diffusion constant, say D. To this end, one uses the Stokes-Einstein equation [54] for spherical particles moving through liquids with low (Reynolds number) R_0 as follows:

$$D = \frac{k_B T}{6\pi\eta r}, \tag{2.12}$$

where k_B is Boltzmann's constant, T is the thermodynamic temperature in Kelvins, and r is the radius of the bead. Accordingly, the total brownian distance traveled is computed as the root mean-square displacement (RMSD) [55] as

$$\sqrt{\langle x^2 \rangle} = \sqrt{q_i D t}, \tag{2.13}$$

where $\langle x^2 \rangle$ is the averaged $\sum\limits_{i=0}^{n} x_i^2$ (sum of all square displacements), t is the time in seconds, and q_i is a numerical constant which depends on dimensionality. For example, if the bead is restricted to move in one dimension (i.e., 1D) then $q_1 = 2$, for 2D, $q_2 = 4$, and for 3D $q_3 = 6$, etc. As a result, it is obvious from (2.12) and (2.13) that the displacement is inversely proportional to the square root of the radius of the bead. In this work, the bead is considered to move in the X-Y plane only and it doesn't experience a brownian displacement larger than the radius of the on-chip coils. Finally, the switching period (for the pseudo-parallel execution) of a coil should be smaller than the time it takes a bead to diffuse from the center of the coil (trap) to its outer edge. Therefore, instead of keeping a coil switched on all the time to trap a certain bead, one can optimally select a switching period to trap a bead before it diffuses out of range; thus, saving power and reducing the amount of heat generated.

Finally, Fig. 2.2 summarizes the forces discussed above in terms of the radius of the magnetic bead used. First, the gravity force is mainly canceled by the buoyancy and is neglected when transporting beads on the surface of the chip. Second, two magnetic forces (Magnetic1 and Magnetic2) were generated from different coil variants to illustrate the range of forces, these can be increased by incrementing the amount of current (therefore B) through the coil. Third, the drag force becomes more prominent for nano-scale sized beads. In this work, the size of the bead is in the micro-range (i.e. 10^{-6}). Fourth, the van der Waals force (FvdW) and electrostatic double-layer force (FeL) make up the DLVO forces which can hinder the movement and transportation of the beads when configured incorrectly.

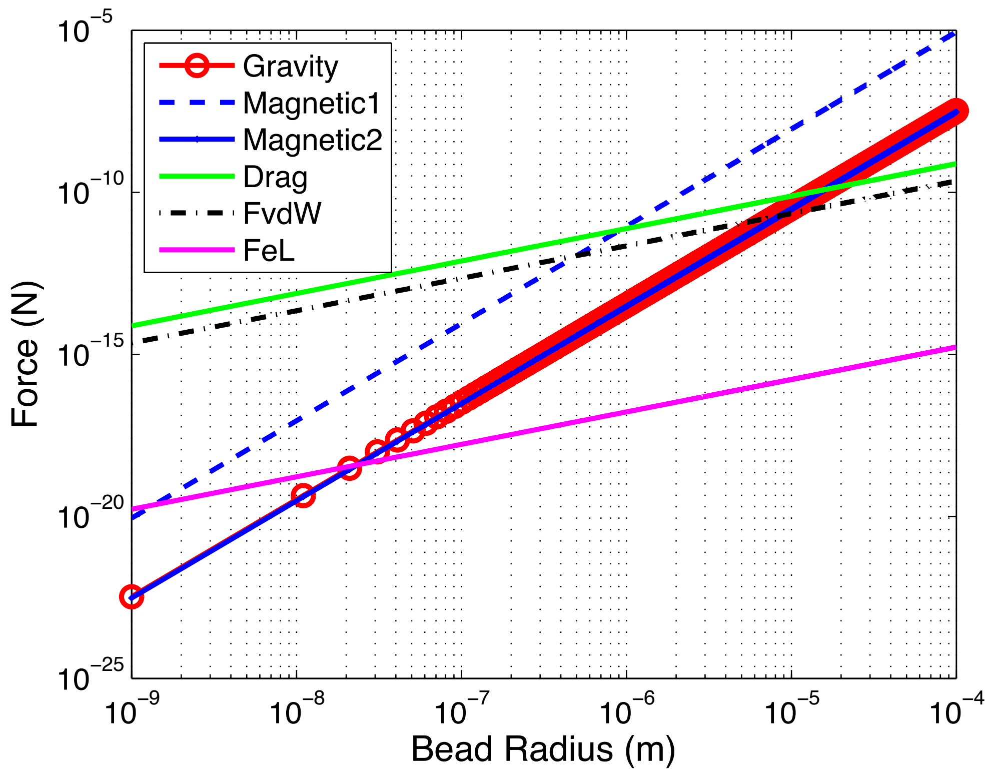

Figure 2.2: Summary of forces acting on a bead with various radii. The parameters in the equations estimated as: $g = 9.82m/s$, $B1 = 1.43e^{-2}T$, $\nabla B1 = 187.75T/m$, $B2 = 6.25e^{-4}T$, $\nabla B2 = 14.42T/m$, $\Delta\chi = 1$, $d = 10e^{-9}m$, $\eta = 1$, $v = 1e^{-6}m/s$, $A = 3.4e^{-21}$, $\lambda = 90e^{-9}m$, $\epsilon = 7e^{-10}$, $k = 1.38e^{-23}J/K$, $T = 298K$, $N_A = 6.02e^{23}$, $e = 1.602e^{-19}C$, $i = 0.03mol/l$, $\psi_s = -3e^{-3}V$, and $\psi_b = -26e^{-3}V$.

Chapter 3

Integrated Circuits and Systems Design and Implementation

3.1 Introduction

Low cost lab-on-chip platforms are establishing a new venue for clinical diagnostics specifically in point-of-care testing (POCT) and in-field deployment. They are becoming more attractive due to their portability, inexpensiveness, disposability, robustness, reliability, and high throughput. By using very small sample volumes (in the order of 1-100μL) one can identify, diagnose, or separate samples with very high precision using superparamagnetic beads.

Binding biomaterials to magnetic beads is relatively simple. It requires a standard preparation protocol which depends on the surface coating of the bead. Manufacturers [37, 56, 35, 36] offer variety of coatings to enable easier binding and faster deployment. For further discussion on the use of magnetic beads in analyzing biological and chemical samples, the reader is referred to a recent review by M. Gijs et al. [5].

3.2 DC Manipulation

In this section we introduce the design of 8x8 magnetic manipulation coil-arrays, fabricated in standard 0.5μm CMOS technology, suitable for bio-medical applications. The spacing between any two coils is 0.9μm, which is the smallest DRC (Design Rule Checking) value permissible in this technology. By placing digital switches and controllers to the outer sides of the array, one can stack the coils of the array closely to enable shaping the overall magnetic field profile and consequently the forces over the array. The system-level block diagram depicted in Fig. 3.1 consists of four major components: the 8x8 coil array, 3-to-8 row and column decoders, a variable power bi-directional current source, and the global digital logic control. First, the global control is responsible for: (a) coordinating the generated magnetic fields by providing the correct signals to the decoders and the current source, (b) providing a flexible interface to allow programmable off-chip algorithms for control and manipulation, (c) fast switching with a period of 25n seconds for pseudo-parallel collaborative or single-coil manipulation. Second, the row/column decoders and digital logic (a) facilitate single coil selection (b) minimize interconnect coupling and noise, and (c) lower the overall number of I/O pins of the package. Third, an eight-level bi-directional current source to generate different magnetic flux densities and directions for refined maneuvering. The last component is the actual coil-array where electric current is passed through a pre-selected coil location to generate an electromagnetic field using on-chip multi-layered inductors.

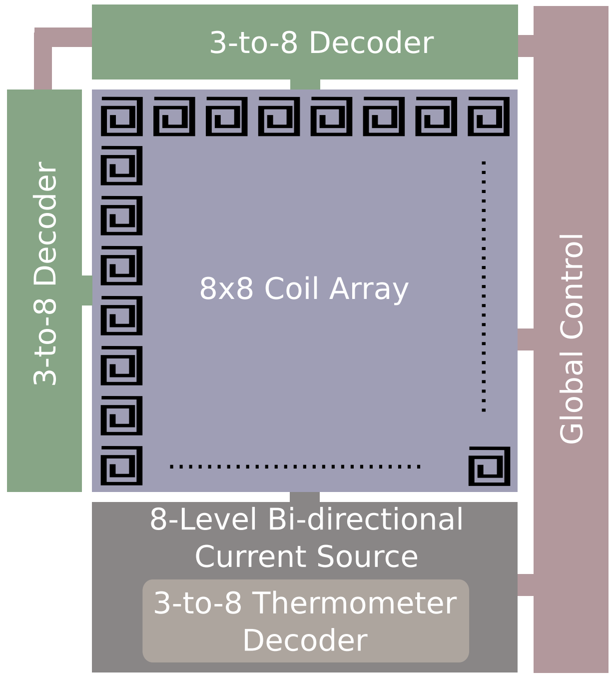

Figure 3.1: System-level block diagram.

3.2.1 Programmable Current Source

NMOS transistors are used to sink currents through a coil. The resistance of the path (including the coil) as well as the width/length of the transistor set the amount of current which can be sunk, thus, eliminating the need for a dedicated resistor to set a reference current. However, the maximum current drawn has to conform with the technology's current density limits in order to keep the substrate at room temperature and protect the metal layers and oxides from overheating and melting.

We have cascaded a set of eight NMOS transistors in parallel to create a binary controllable current sink. A simplified depiction of this configuration is shown in Fig. 3.2. It operates as follows: a user selects a single coil from the 8x8 array using *row* and *column* decoder signals. Next, the direction (polarity) of the current is selected (e.g. counter-clockwise or clockwise) using S and $\bar{S}$. The parallel NMOS block as well as the current direction

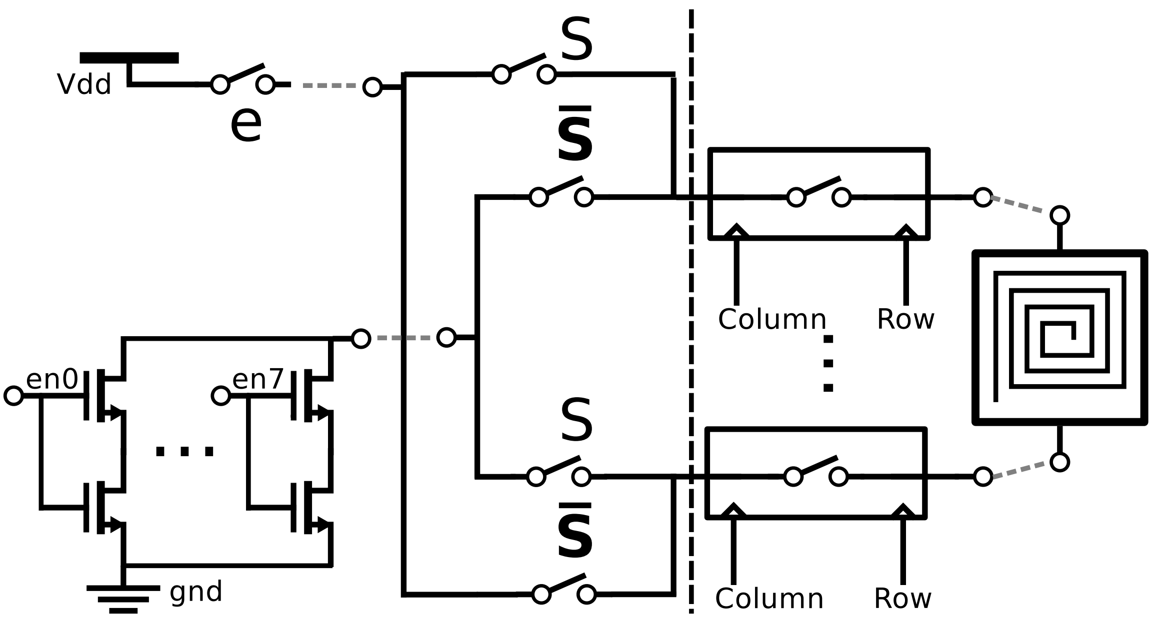

Figure 3.2: Variable power bi-directional current sink with a simplified coil path. The 'e' signal is an "enable" signal which can be used to switch on/off the entire DC actuation path. The components on the left of the dashed line are shared across the entire array to save area.

(polarity) switches are shared across the whole array to reduce real-estate. An eight bit word *en*[0:7] is used to adjust the amount of current required for actuation. Fig. 3.3 shows a post-layout simulation, with parasitic capacitance and resistance extracted, of one of the programmable current sinks implemented. When the signal S is high the direction of the current is positive (counter-clockwise for the spiral coil) and vise versa.

The non-linearity of the steps are a result of the parallel NMOS arrangement. The forces generated from the coil and exerted on the beads are inherently nonlinear, regardless of these steps, see (2.5). This non-linearity is exploited to create larger forces for the initial motion/magnetization of the bead then refined to smaller steps as we increase the amount of current sunk by the parallel NMOS transistors. If linear current sources are desired, one can carefully resize the parallel NMOS transistors in a custom design.

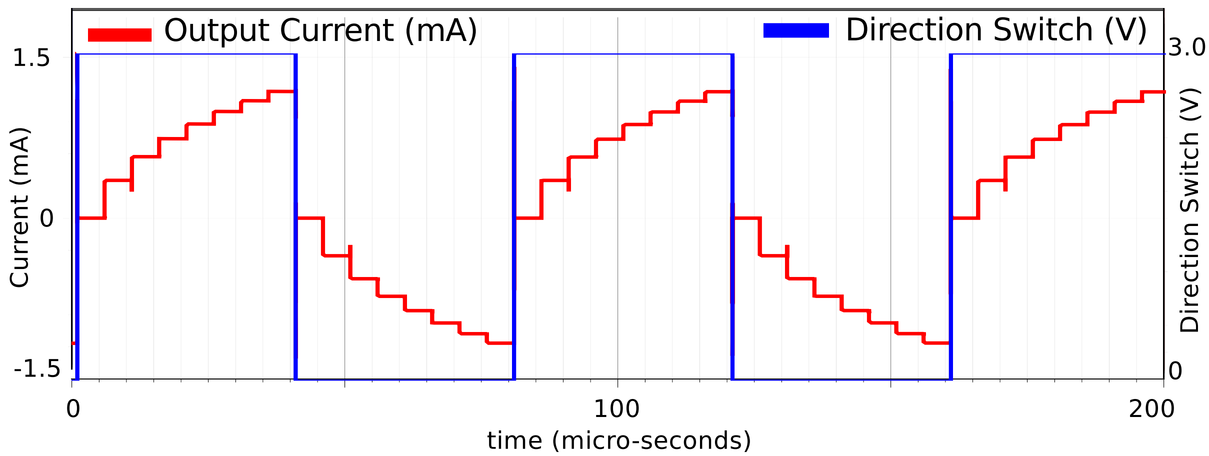

Figure 3.3: Post layout simulation of one of the programmable current sources implemented on chip. The magnetic field direction can be changed using the positive current stairs or the negative ones.

3.2.2 Digital Logic

To individually access each coil in the 8x8 array, two 3-to-8 decoders link any inductor load to the programmable current source. The decoders allow each input to enable one of the eight rows or columns available. For pseudo-parallel manipulation schemes, a high-speed control signal (switching up to 40 MHz) is used to link a specific cell to the driving circuity and it consists of a dedicated transmission gate as well an AND gate, see Fig. 3.4. If cross-talk is tolerated in an application, a single NMOS switch can be used to minimize the size and logic of the control circuitry [21]. However, due to the noise and coupling generated by the neighboring coils, using NMOS switches exhibits a negative influence on the performance of the array.

In Fig. 3.2, the components on the left of the dashed line are shared across the whole array to save space on the die. The components on the right are intentionally duplicated for every single coil in the array. When designing a coil array's schematic, it might be intuitively appealing to use a shared ground rail to interconnect all coils. However, it is crucial to

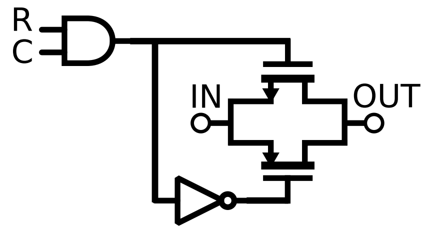

Figure 3.4: A dedicated AND gate and a transmission gate are used to isolate signals from/to each coil in the array.

separate and isolate the ground paths to minimize ground bouncing [57]. The array operates in a pseudo-parallel scheme using high speed switches which hammer the ground node with large and fast changing currents. This causes the ground node to move, thus, affecting the performance of the system with unintentional transients, electromagnetic interference (EMI) radiations, and inductive coupling with neighboring coils. The main cause of this repercussion is due to the rapid changing of the magnetic flux (Φ_m) in the interconnects. However, the magnetic flux is directly proportional to the magnetic field passing through a loop area or a boundary as

$$\Phi_m = \oint_c \mathbf{A} \cdot d\ell, \tag{3.1}$$

where the magnetic flux Φ_m is defined as the line integral of the magnetic vector potential $\mathbf{A}$ passing through a surface bounded by contour c traced along an infinitesimal vector element $d\ell$. Therefore, in order to reduce the flux, which causes ground bouncing, the path back to ground should be reduced. As a result, we separated the ground path for each coil using two dedicated switches. This makes the overall loop area around ($\mathbf{A}$) shrink, causing the total magnetic flux to be reduced. Additionally, a second measure is employed in the layout to reduce noise by creating a patterned metal1-poly ground shield [58] beneath each coil in the array. This reduces coil-substrate coupling and increases the performance of the coil (namely, the coil's Q-value).

3.2.3 Actuator

A square shape spiraling inductor is selected in this design to meet “Non-Manhattan-shape” DRC requirements for this CMOS technology. In another coil array design, a similar coil array is created with different specifications. The side length of a single coil is approximately 80μm and it produces larger forces and utilizes larger DC currents.

To foresee the forces and the magnetic flux densities generated by each coil we used a Finite-Element-Method (FEM) simulator to precisely model the CMOS substrate, metal layers, and passivation layers, using the process’ proprietary specifications. We consequently obtained the most predictive results as depicted in the sample of Fig. 3.5. Here, the X-Axis represents the distance from the center of the 30μm x 30μm coil, the Y-Axis is the magnitude of the magnetic flux density (B). Note that the generated field, without a bead present on top of the coil, will have two maxima near the coil’s center (shown via the solid red curve) because the spacing between the metal windings cannot be reduced below the DRC requirements. However, for distances at and above 2μm (shown via the dash-dotted green curve), this effect disappears. Consequently, a 2μm silicon oxide and silicon nitride layers, provided by the fabrication house, are applied. Such layers also serve as a protection covering for the platform. While the silicon nitride layer is bio-compatible with some experiments, other alternative chemicals like Parylene-C can also be deposited post fabrication to meet the application’s requirements. Moreover, when adding a 1μm bead on the surface of the chip, aligned to the center of the coil, the magnetic flux density is increased and focused toward the bead. This increase is due to the coupling between the coil and the bead. Also, the result magnetic field is not perfectly centered because the coil’s winding doesn’t perfectly end at the center.

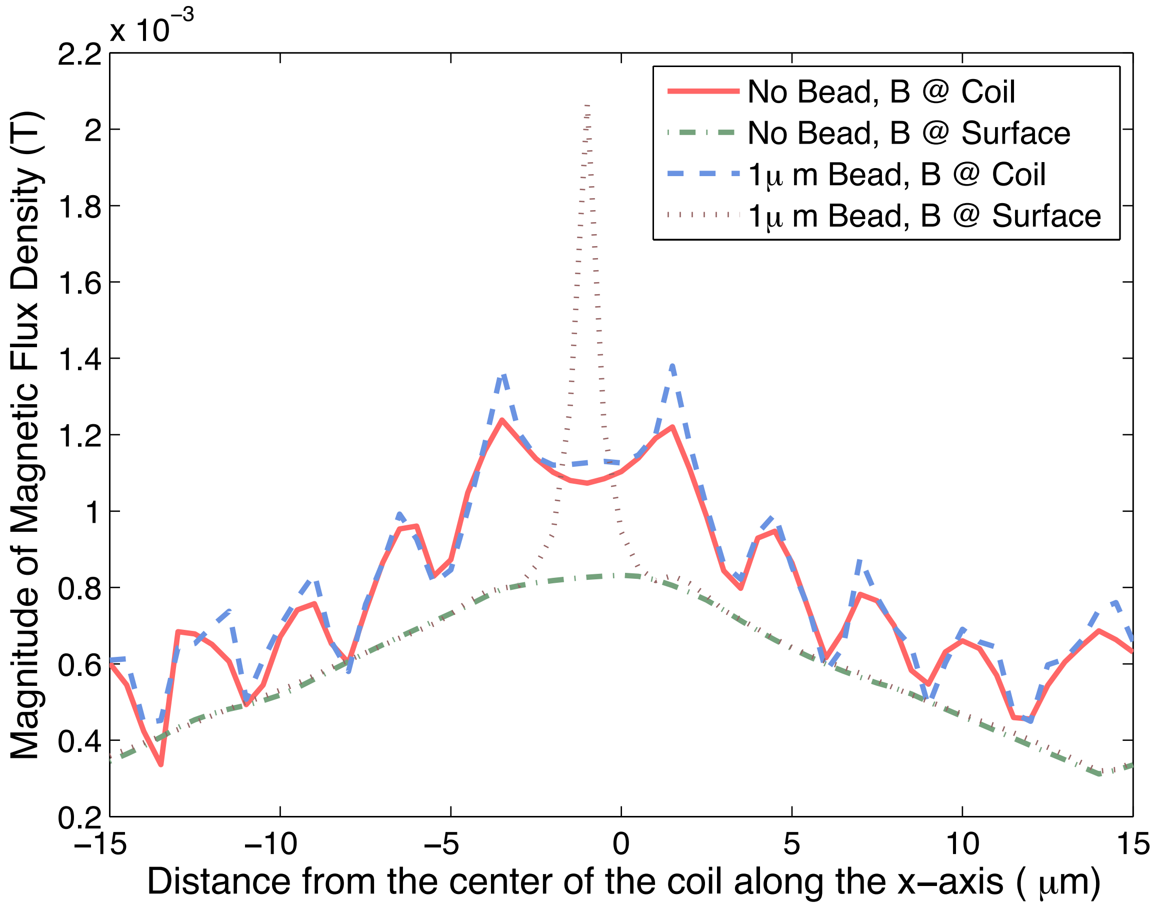

Figure 3.5: FEM simulation of the 30x30 coil's magnetic flux density at the surface of the chip and near the metal winding.

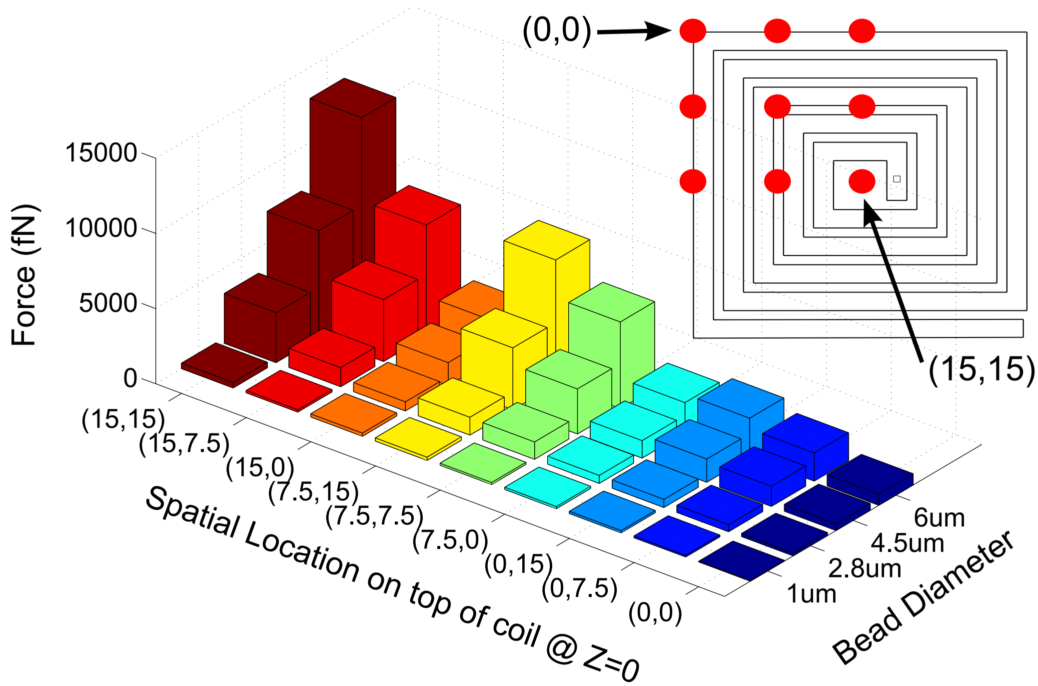

Figure 3.6: FEM simulation of the coil's magnetic force generated on various beads using 1.5mA using the 30μm x 30μm coil. The beads were placed on different spatial locations on the surface of the chip.

To predict the forces acting on the bead, we use different Invitrogen DYNAL®magnetic bead [36] sizes, which are modeled in the FEM simulator using the physical specifications as well as the B-H hysteresis curves provided by the manufacturer. Using the simulator, a current of 1.5mA is passed through the 30μm x 30μm coil generating different magnetic flux densities. The force acting on the surface of the bead is calculated, using the "virtual work" method and depicted in Fig. 3.6. The beads were placed on the surface of the chip (i.e Z=0) and then moved in the X-Y plane. From a top-view perspective, a bead located at (0,0) is placed at the upper left corner of the coil and experiences the weakest magnetic force. A bead located at (15,15) is placed at the center of the coil and experiences the largest magnetic force.

Similarly, for 80μm x 80μm the magnetic flux density is simulated, shown in Fig. 3.7,

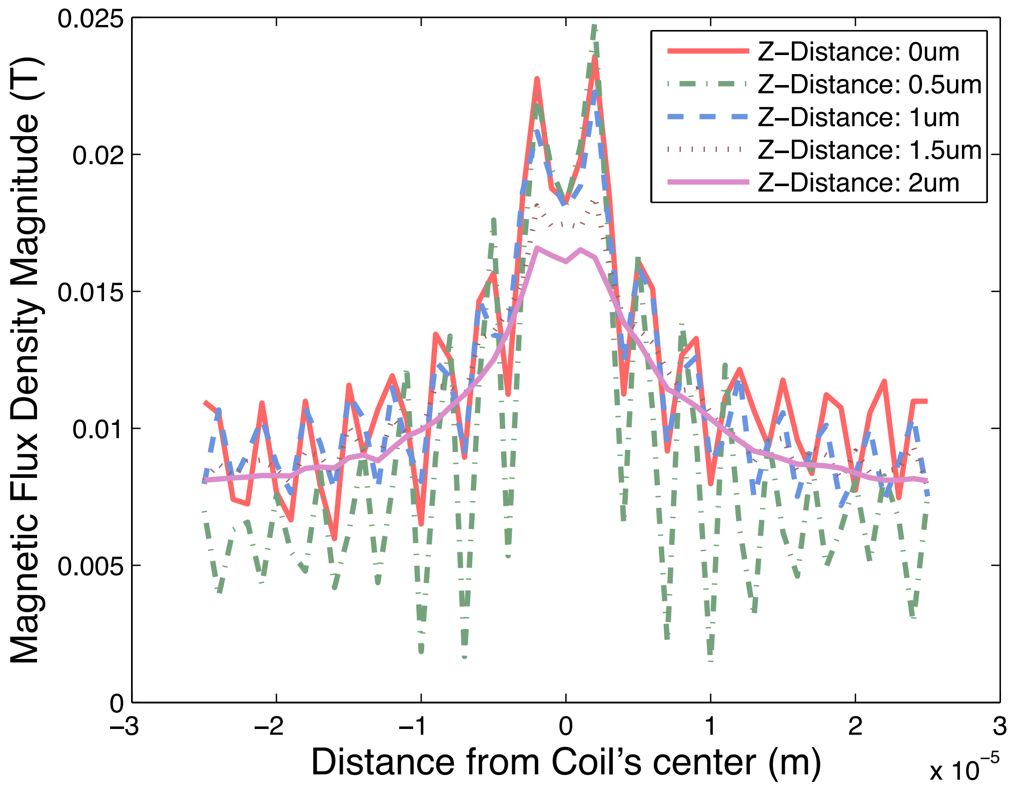

Figure 3.7: FEM simulation of the 80x80 coil's magnetic flux density at the surface of the chip and near the metal winding.

using the same FEM simulator. The DC current is 40mA and the largest magnetic flux around the center is 17mT. The amount of force generated from these coils is much larger than the previous one. A second simulation is conducted to measure the magnetic force, shown in Fig. 3.8, on a 2.8μm beads at the surface of the chip. The bead is placed at the center of the coil and at the upper left corner. The smallest and largest forces at the corner are (38.86fN at 1mA) and (62.18pN at 40mA) respectively.

3.2.4 Arrays

To target larger forces (up to 1nN) a larger on-chip coil actuator is designed as discussed in section 3.2.3. The 0.5μm bulk CMOS technology used supports three metal layers. The

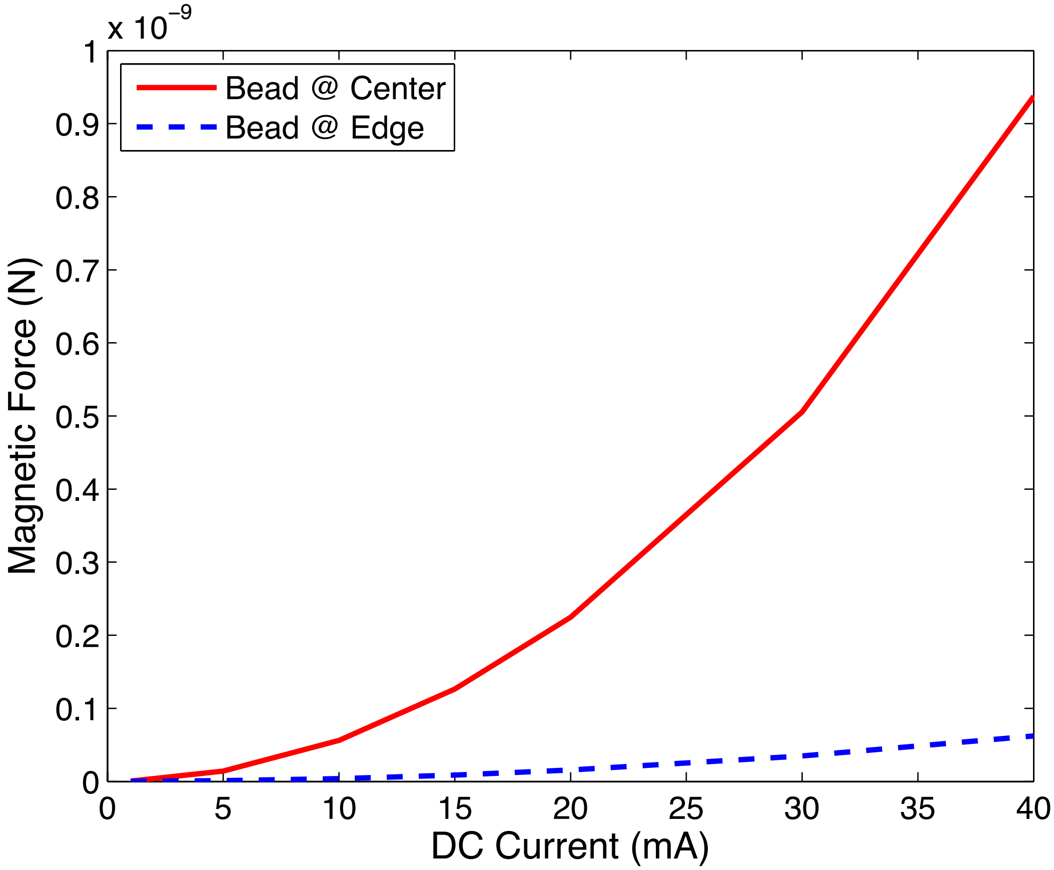

Figure 3.8: FEM simulation of the coil's magnetic force generated on 2.8μm bead using the 80μm x 80μm coil. The bead was placed in the upper left corner (edge) and the center locations on the surface of the chip (i.e. Z=0).

Table 3.1: Coupling coefficients and mutual inductances

K=-9.19m M=-10.33p	K=-35.52m M=-39.95p	K=-9.19m M=-10.33p
K=-38.28m M=-43.06p	Center Coil	K=-38.28m M=-43.06p
K=-9.19m M=-10.33p	K=-35.52m M=-39.95p	K=-9.19m M=-10.33p

upper most two metal layers (metal3 and metal2) are used to create the coil's windings and the lower most layer (metal1) is used for routing (e.g. interconnecting the coil's two ports to their corresponding switches), see Fig. 3.9. Careful routing techniques are required to (a) minimize the coupling across interconnects (b) accommodate the largest number of coils in the array while keeping the distance between any two coils at minimum, namely 0.9μm (c) shorten the routing path to keep the interconnect resistance at minimum. Finally, there is a trade-off between the size of the coil, the number of metal layers available in the CMOS technology, and the maximum current density allowed per via. Thus, one has to balance between all these parameters to achieve the desired force and array size.

Owing to the fact that the coils are closely stacked, mutual inductances and coupling coefficients must be considered when building the entire array. In order to quantify these effects, a 3x3 sub-array snippet is formed of coil sizes of 30μm x 30μm. Table 3.1 lists the mutual inductance values (M) and coupling coefficients (K) computed by ASITIC [59] as seen by the coil in the center of the 3x3 snippet.

Integrating all modules together on the same die requires careful examination in terms of routing, isolation, and coupling among neighboring coils. Moreover, the modular design should consider distributing heat equally across the entire array to maintain consistent interactions with the bio-objects of interest. The system, shown in Fig. 3.10, has three different

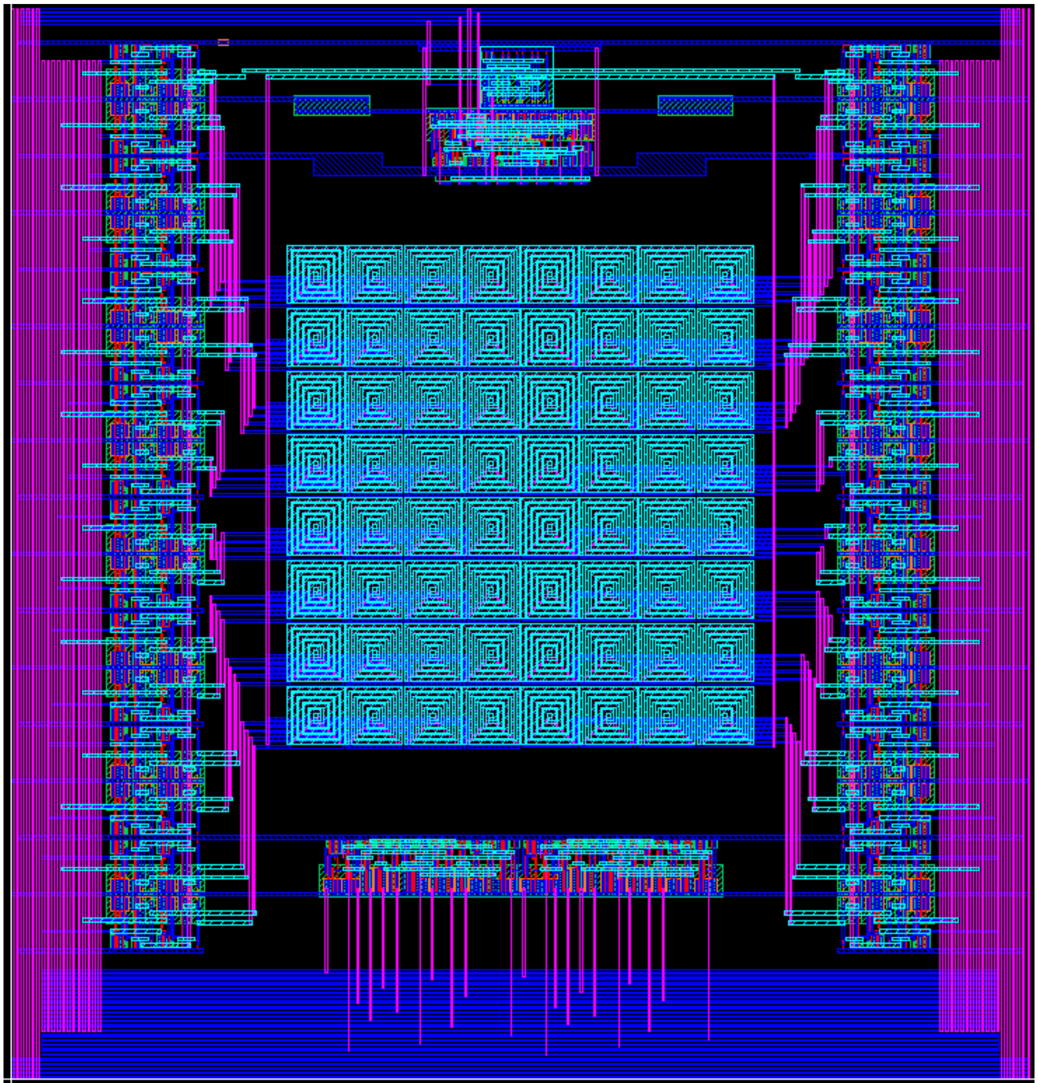

Figure 3.9: Layout of stacked coil array. The array is centered in the middle and surrounded by digital switches from the left and right sides. The DC current source along with the thermometer decoder are placed on the top. The digital row/column decoders are placed at the bottom.

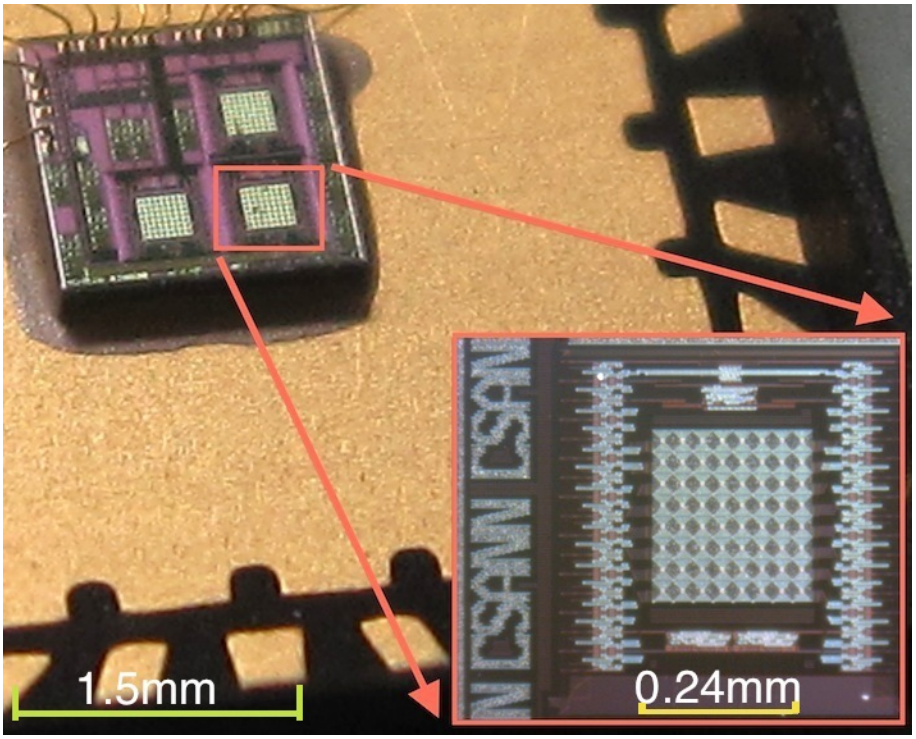

Figure 3.10: Photograph of 1.5mm x 1.5mm CMOS die as an open cavity device.

8x8 arrays; each one uses different routing and isolation techniques, DC driving circuitry, and configuration. This prototype is fabricated in 0.5μm 3-Metal-2-Poly CMOS. It consumes 9mW using a 5v power supply. We used the 1.5mmx1.5mm die to accommodate all three 8x8 arrays. Each coil array occupies 248μm x 248μm and requires a 100μm x 260μm digital overhead (switches, decoders, etc). A second prototype, also fabricated in 0.5μm 3-Metal-2-Poly CMOS, has similar specifications but larger coils, improved grounding and isolation, and larger DC currents to generate larger forces. This prototype, however, consumes 31mW using the same power supply voltage running at power level (000) and 200mW when running at full power (i.e. 111).

Two different experiments are conducted to quantify the forces generated by the 30μm x 30μm coils and one experiment for the 80μm x 80μm coils. The first experiment is to test that the coils are capable of generating magnetic forces on micro-scale objects before submergence into fluids. Therefore, we used an Atomic Force Microscopy (AFM) system by "Nanosurf" called "EasyScan 2 AFM" [60] with a magnetized cantilever (MAGT) [61] fabricated by "AppNano". The cantilever's tip height is around 15μm and its radius of curvature (ROC) is around 35nm. The principle used in measuring the force is called Magnetic Force Microscopy (MFM) where the stray magnetic field generated by the coil array interacts with the magnetized tip by moving the flexible cantilever up/down as shown in Fig. 3.11. Using this technique the magnetic force or force gradients are measured for the coil array using AC or DC (current) modes. For this experiment, the DC "Static" mode was used in the measurements.

Measuring a force using a cantilever is based on Hooke's law where the cantilever acts like a spring with a constant k and responds to a force F (in equilibrium) as follows

$$z = \frac{F}{k}, \tag{3.2}$$

where z is (proportional to) the deflection of the lever. As a result, when measuring the deflection using the laser sensor, one can directly measure the force generated by the coil array acting on the tip. Also, the force F can be computed as in section 2.3.2 using (2.5) but the magnetic moment $\vec{m}$ is the moment of the cantilever and $\vec{B}$ is the stray magnetic field from the coil array.

Because we are using the DC mode, the sensitivity of the measurement is limited by the deflection sensor's noise. There is an additional pink noise associated with the type of the detector being used (e.g. piezoresistive) and the 60Hz power line/fluorescent light noise. These factors should be considered while studying MFM measurements. Nowadays, most commercial AFMs come with dedicated filters to eliminate and reduce these noise sources.

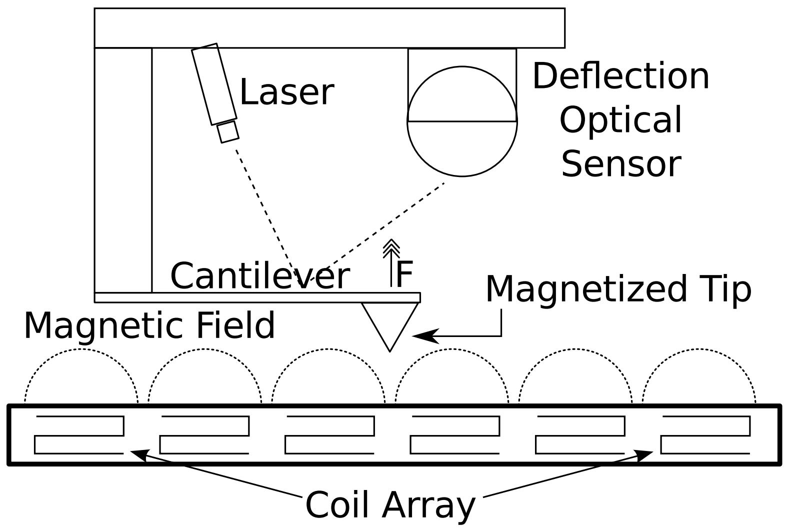

Figure 3.11: Concept drawing showing how an AFM system can be used to measure the magnetic field generated by the coil array. The cantilever flexes according the magnitude of the field generated on the magnetized tip. The optical sensor detects the laser deflection caused by the movement.

To measure the magnetic force generated by the 30μm x 30μm coils, the cantilever's tip is placed on top of a coil, specifically, the upper left corner using a micro-positioner stage. Next, a 7μm x 7μm region, the maximum area allowed using the current AFM system, is scanned while keeping the AFM's Z-controller fixed at a pre-specified height. During the scan, the deflection of the cantilever is recorded and then multiplied by the spring constant to produce the force as depicted in Fig. 3.12. In this experiment, the single coil was switched on when the AFM scan reached half of the 7x7 block. Thus, the right half of the figure (colored mainly in green) depicts the coupling forces between the cantilever's magnetic tip and the coil (while it was switched off). In contrast, the left half of the figure (colored mainly in blue) depicts when the coil is switched on and exerting a magnetic force on the cantilever's tip, which caused it to deflect forward.

Second, a lab experiment is conducted to validate the transport forces acting on a single bead in the X-Y plane. The setup is very similar to the one shown in Fig. 5.3. While the

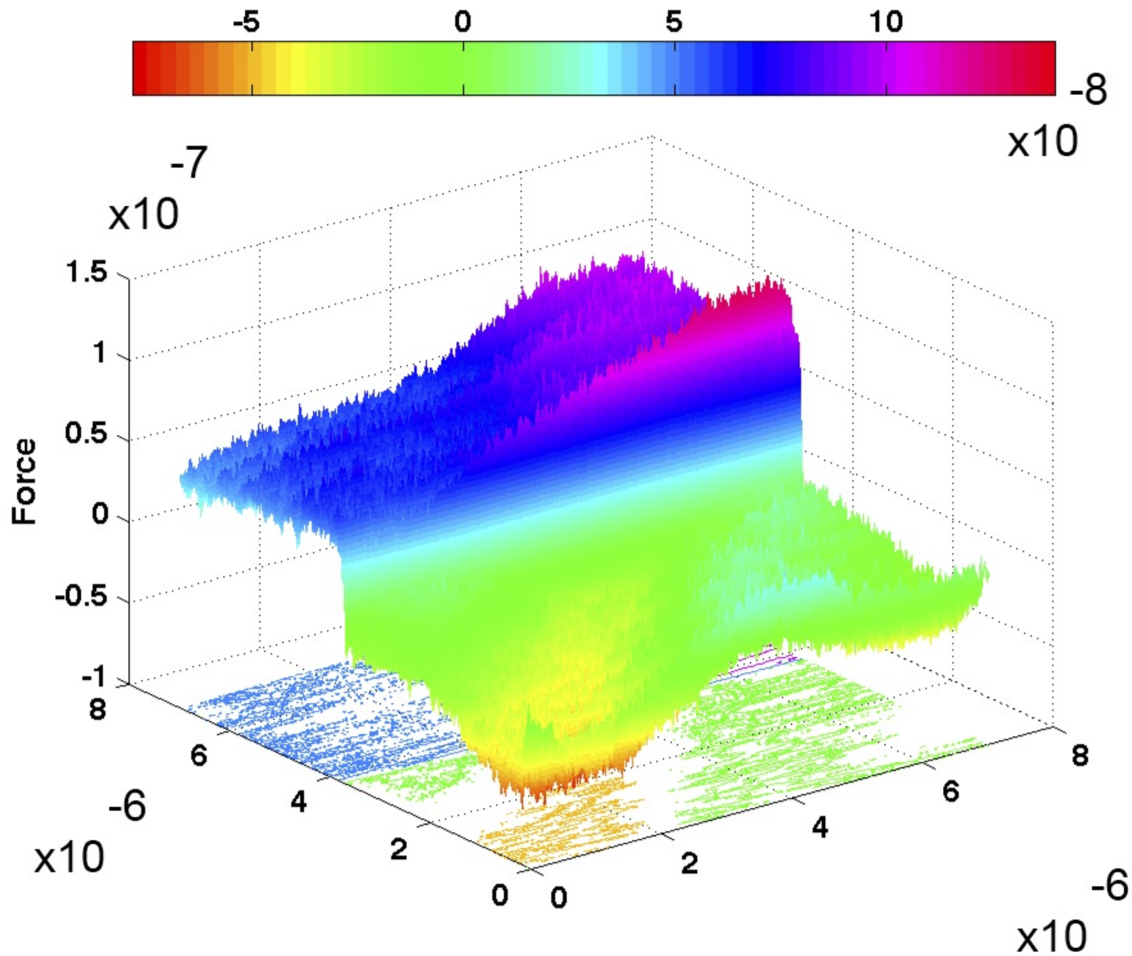

Figure 3.12: Magnetic Force Microscopy measurement of a 7μm x 7μm region on top of the coil. The coil was switched on in the middle of the scanning process.

30μm x 30μm coils are switched off, small droplets (5μL) of a diluted 1μm Tosylactivated magnetic beads solution are inserted in the PBS solution using a pipette. Then a small (1 minute) grace period is observed in order for the beads to settle in the fluid or on the surface of the chip. Using a microscope, one visually locates a magnetic bead on the 8x8 array and programs a specific coil to attract the bead toward it. Fig. 3.13 shows multiple frames taken from a video sequence while a bead is being manipulated to the right. In frames 4, and 5 the bead is attracted closer to the surface by switching on the coil to the left. In the remaining frames, the bead is transported to the right by switching off the coil on the left and switching on the coil on the right. The total distance traveled in this experiment was 16μm in 3.3 seconds, which is an average velocity of 4.85μm/s. The magnetic force generated in this experiment cannot be compared with the simulations conducted in section 3.2.3 because the bead did not fully move to the center of the coil. This is due to several possible factors: The X-Y transitional forces are not strong enough to influence the bead, the bead found a preferred chemical binding site and attached itself to it, or the equilibrium forces acting on the bead are not maximized at the center of the coil. This latter possibility is caused by the fact that the main vdd/gnd rails (power supply and ground rails), which are exposed, are contributing to the transition. Careful vdd-gnd shielding is required to alleviate this influence.

The last experiments are performed on the 80μm x 80μm coil array. The setup is very similar to the previous experiment except that the medium used here is deionized water, and the beads' size is 2.8μm in diameter with Protein-G coating. The 2.8 micron beads have more iron content than the one used in the previous experiment.

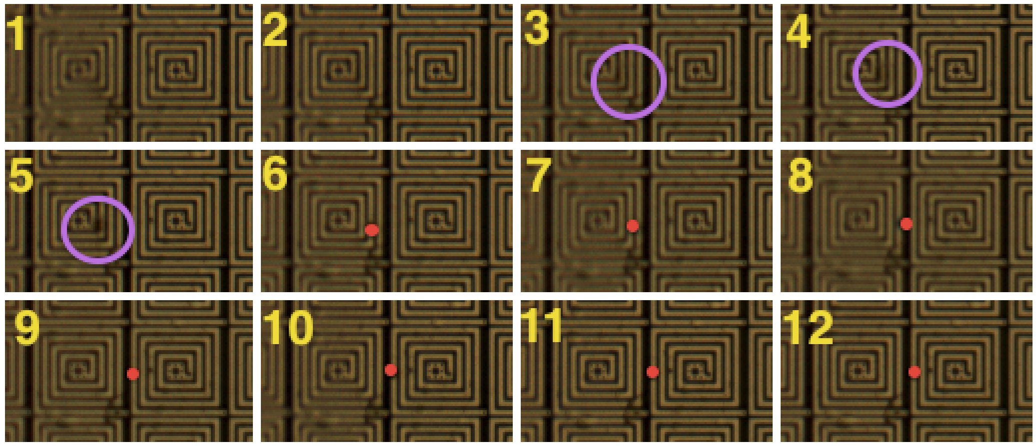

Figure 3.13: A montage of a series of video frames showing how a magnetic bead is attracted (downward) toward a coil then moved to the right by switching on the neighboring coil.

3.2.4.1 Bead Transport

A proof of concept of bead transport is demonstrated in a supplementary video at (`http://www.msu.edu/~asd1815/videos.html` titled [on_transport]) and as a montage in Fig. 3.14. Initially, the beads are randomly moving on top of the coil array then the upper right coil is switched on. The beads that lie above the coil immediately move to the center, and the beads at the neighboring coil are transported to the right. Next, the upper right coil is switched off and its neighbor is switched on. The beads that aggregated on top of the upper right coil are now transported to the neighboring coil. Note, that a collection of beads attached to a debris lying on top of the third coil, from the right, is also transported. Lastly, the neighboring coil below is switched on and the beads are transported to the next row. The forces in this experiment were chosen to affect the immediate neighboring coils only. If the bead doesn't lie in that area then it would not be transported. Finally, a bead lying at the edge of the coil reached the center in 1.75s. Therefore, the average velocity is approximated to be 22.8μm/s and the average magnetic force is 602pN. The debris' average velocity from the third coil to the second is approximately 2.1μm/s and the average magnetic force is 55pN. These forces are comparable with the simulation results provided in Fig. 3.8, i.e. the bead lying at the edge initially faces a 62pN magnetic force and quickly reaches 940pN. Therefore, on average a bead on the edge of the 80μm x 80μm coil will approximately encounter an average of 600pN.

3.2.4.2 Pseudo-parallel Manipulation

In addition, we demonstrate more abilities of these platforms in another video at (`http://www.msu.edu/~asd1815/videos.html` titled [on_msu]) and as a montage in Fig. 3.15. The movie clip demonstrates two features: (1) pseudo-parallel manipulation; where the beads are collectively used to draw the letter "M" simultaneously. This parallel movement of the beads is a result of careful coil-array layout and isolation, dedicated high-speed switches, and precise magnetic forces that do not span beyond the pre-specified spatial location. (2) Pre-defined bead diffusion delay, which allows the user to program the array to wait for a specified amount of time for the beads to diffuse in order proceed with the next operation. This feature is observed after drawing "M" and before drawing "S", and after drawing "S" and before drawing "U." Algorithm 1 explains how the coil array is used to draw the letters in the word MSU. The switching speed for this experiment was chosen to be 16MHz, the byte codes (e.g. LTR_M) represents the spatial location of the coil to be switched on. The length of the byte code represents the total number of coils to be switched on in pseudo-parallel fashion. For example, to draw the letter "M" 21 coils in the array are activated simultaneously. If the coil location is present in the byte code then it will be switched on and actuated "REFRESH_RATE" times to trap the beads for a longer period of time in that position. Once the letter "M" is drawn the, procedure "CALL_DIFFUSION_DELAY" is executed to allow the beads to diffuse before drawing the next letter.

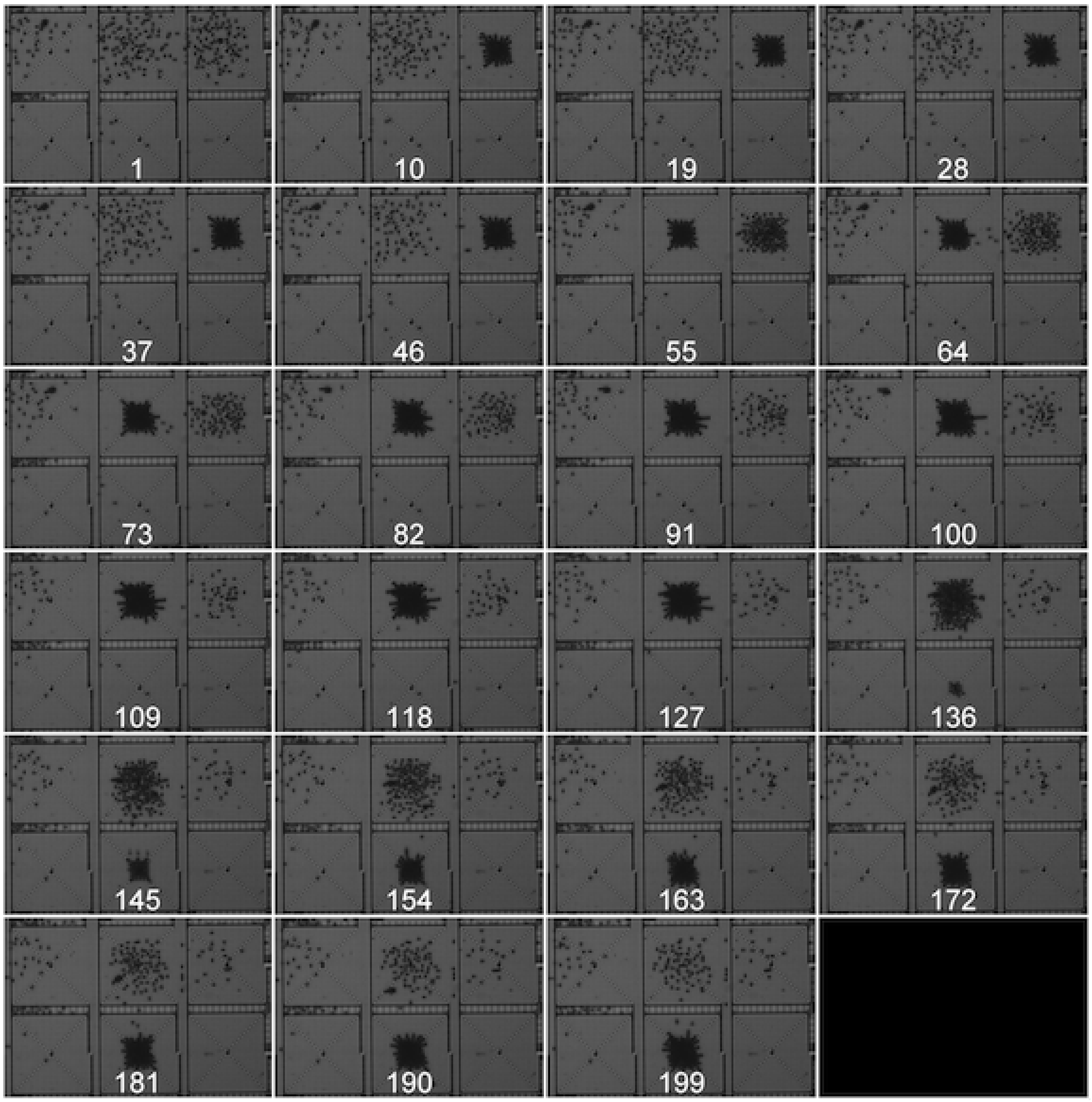

Figure 3.14: A montage of a series of video frames showing how magnetic beads are transported from one location to another.

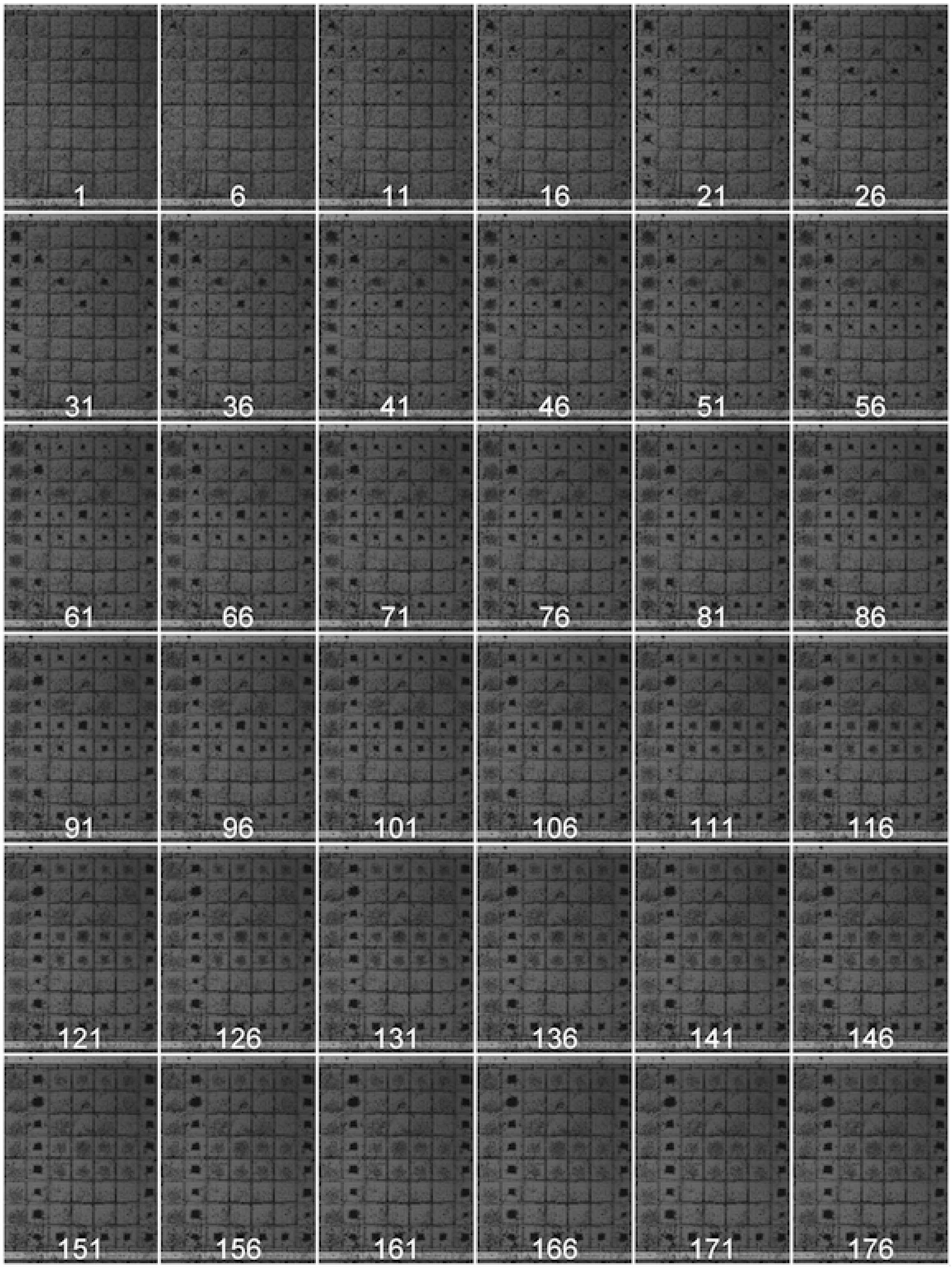

Figure 3.15: A montage of a series of video frames showing how magnetic beads can draw the letters M S U sequentially using pseudo-parallel scheme.

Algorithm 1 Draw MSU On-Chip

DEFINE $LTR_M[21] = 0xC0, 0xF0, 0xC1, 0xC9, ...$
DEFINE $LTR_S[30] = 0xC8, 0xD0, 0xD8, 0xE0, ...$
DEFINE $LTR_U[20] = 0xC8, 0xF0, 0xC9, 0xF1, ...$
DEFINE REFRESH_RATE = 100
DEFINE REFRESH_DELAY = 2ms
DEFINE SWITCHING_FREQ 16MHz
if $LETTER = M$ **then**
  $LOOP_{COUNT} \Leftarrow LENGTH(LTR_M)$
  $BYTE\_2\_OUTPUT \Leftarrow LTR_M$
else if $LETTER = S$ **then**
  $LOOP_{COUNT} \Leftarrow LENGTH(LTR_S)$
  $BYTE\_2\_OUTPUT \Leftarrow LTR_S$
else if $LETTER = U$ **then**
  $LOOP_{COUNT} \Leftarrow LENGTH(LTR_U)$
  $BYTE\_2\_OUTPUT \Leftarrow LTR_U$
end if
while $LETTERS\_2\_DRAW \neq 0$ **do**
  for $REFRESH = 0 \rightarrow REFRESH\_RATE$ **do**
    for $i = 0 \rightarrow LOOP_{COUNT}$ **do**
      $OUTPUT \Leftarrow BYTE\_2\_OUTPUT[i]$
    end for
  end for
  CALL_DIFFUSION_DELAY( )
end while

Unlike the previous experiment on the 30μm x 30μm array, the one on the 80μm x 80μm array does not suffer from weak bead transitions because: (1) there are two dedicated switches per coil as shown in Fig. 3.2 whereas the previous experiment used a single switch with the second coil node (i.e ground node) was directly shared across the entire array, (2) the vdd/gnd rails are shielded using auxiliary metal layers and placed as far as possible from the array, (3) the amount of DC current is increased in this experiment to generate larger magnetic forces in order to move and trap magnetic beads at the center, and (4) the medium (nonionized water) and magnetic bead coating (Protein-G) reduced the amount of DLVO forces between the beads and the surface of the chip.

Another a lab experiment is conducted on the 6x6 micron coils to validate the translational forces of a bead in the X-Y plane. Before conducting the experiment, the bonding wires between the CMOS die and plastic package are coated with Parylene-C because of its biocompatibility, insulation capabilities, and cost effectiveness [62]. Also, it serves as protection layer on the surface of the chip from a wide range of chemicals. The Parylene deposition process took 1 hour 31 minutes and 40 seconds. The Dimer mass was 3.1348 grams. Next, while the coils are switched off, small droplets (5μL) of a diluted 2.8μm Protein-G Dyna beads solution are injected in the deionized water solution, on top of the chip, using a pipette. Then a small (20 seconds) grace period is observed in order for the beads to settle on the surface of the chip. For testing purposes a microscope is utilized so that the user can visually locate a magnetic bead on the array. Nevertheless, to improve the clarity and focus of the microscope a Corning glass coverslip is placed on top of the plastic package to prevent liquid surface tension, evaporation, and vibration. Next, the user programs a specific coil to attract the bead toward it. Fig. 3.16 shows two frames taken from a video

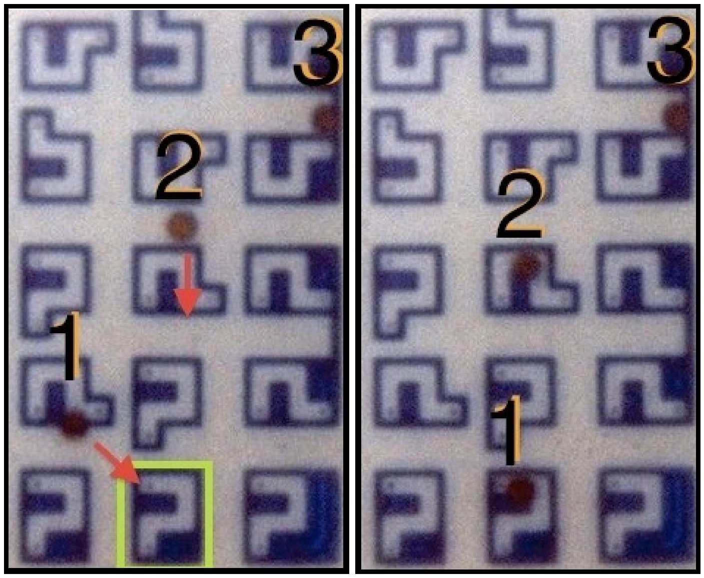

Figure 3.16: A micrograph of the coils closely stacked with three magnetic beads on top. The first frame on the left shows a bead “1” traveling to the highlighted coil when it is switched on. Bead “2” is also influenced by the movement and the magnetic field in the coil and in the interconnects. (50x magnification)

sequence while a bead is being manipulated. Initially the highlighted coil is switched on, namely, row=5 and column=2. Then the bead labeled “1” moves diagonally to reach the center of the highlighted coil after 11 seconds. The total distance traveled by bead “’1” is 7μm in 11 seconds. It is noted that the bead labeled “2” is also influenced by the magnetic field generated by the coil and possibly the local interconnects, however, the magnetic forces acting on bead “2” are relatively weak. To minimize such interconnect influences between coils in the same rows and columns in the array, we have shielded the array, when possible, using the top most metal layer i.e. metal3.

Finally, there is a trade-off between the size of the coil, the number of metal layers available in the CMOS technology, and the maximum current density allowed per via. Thus, one has to balance between all these parameters to achieve the desired force and array size.

3.3 AC Manipulation

The operational concepts of the AC coil array can be explained as follows. Using a technique analogous to switching regulators (switched-mode power supplies), the average output current of the amplifier can be controlled by switching the ring oscillator on/off at select durations. The durations are specific intervals that contain different fractions of the oscillation periods to provide different DC components. Thus, the DC magnetic field, and correspondingly the DC force, can be selectively commanded to generate forward (positive) or backward (negative) actuation on magnetized objects. In one targeted application, namely actuating a magnetic bead in fluid, it is anticipated that the high frequency components would be filtered out by the fluidic medium and primarily low and DC components would contribute to the actuation of the bead. Thus non-contact actuation of magnetized beads is easily achieved with the current integrated platform. The actual strategies of switching operations for best (sensing and/or actuation) performance is relegated to software in order to gain flexibility for broad choices of the sensing and control space.

3.3.1 Class E Power Amplifier

The class E power amplifier (PAE) [63] provides an efficient design of the driving engine for the array. In order to increase the amplifier's overall power output and to digitally control it, one replaces the single NMOS switch with a parallel NMOS configuration [64]. Fig. 3.17 shows the parallel NMOS switches (we use minimum size W/L). The eight inputs are connected to a 3-to-8 thermometer decoder to reduce the number of I/O pins required to control the PAE, and to facilitate binary-word increase/decrease in magnetic field actuation [65]. In Fig. 3.17, RFC represents a large on-chip inductor that provides a DC path from

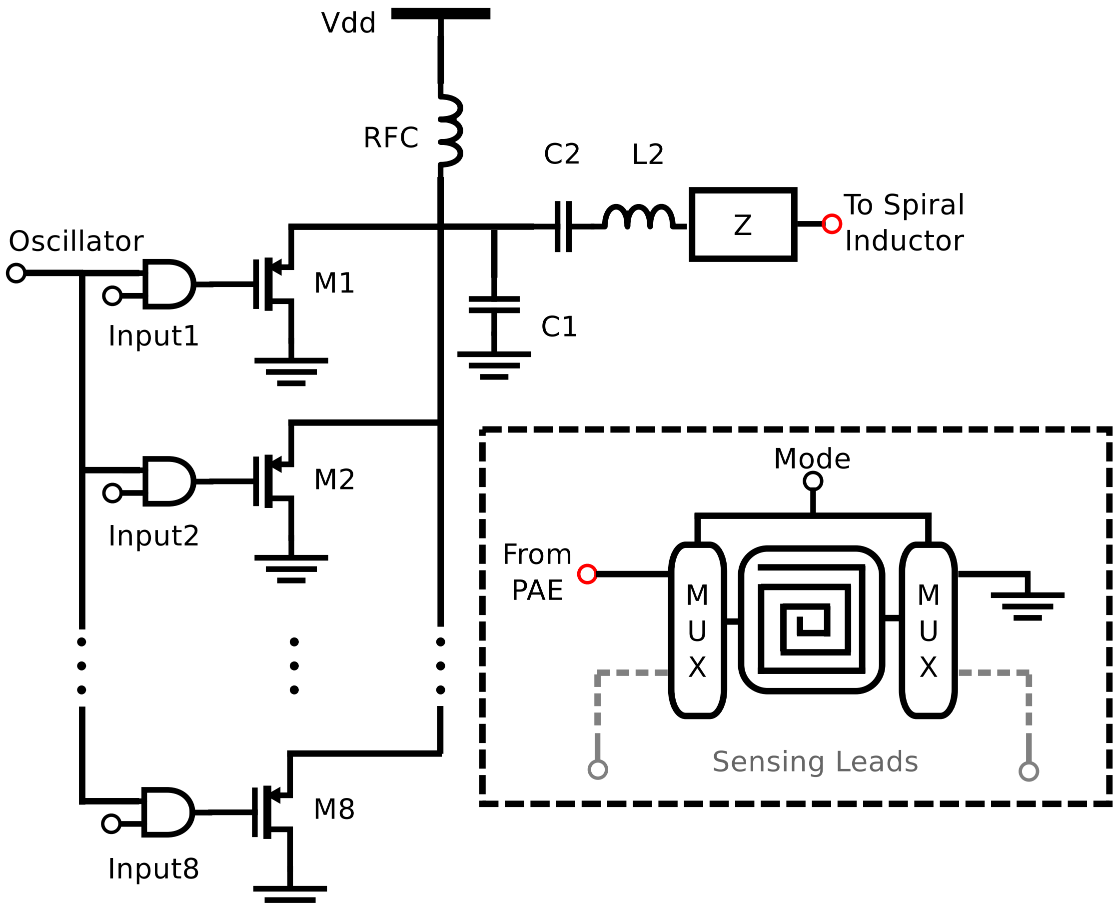

Figure 3.17: A variable gain class E power amplifier tuned at 900MHz. The dashed box is a simplified version showing how the same coil can be shared for sensing and actuation. In actuation mode, the PAE is connected to a single coil, the other end of the coil is connected to ground.

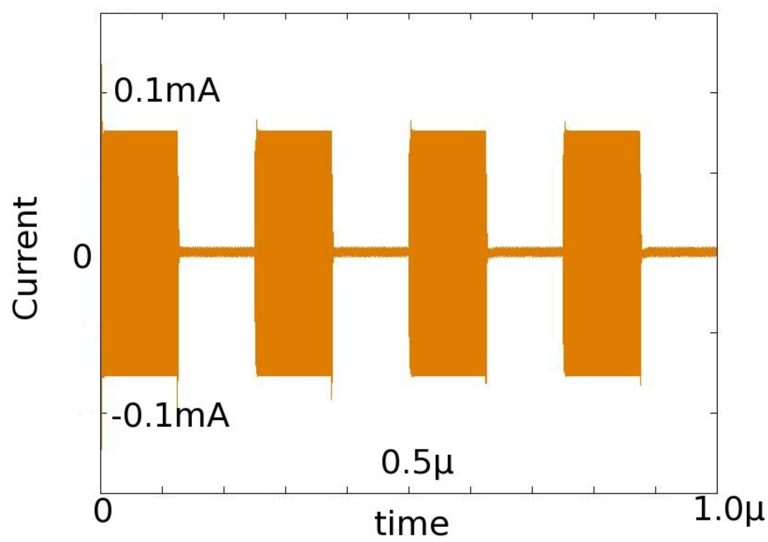

Figure 3.18: The smallest current passing through the actuator during a regular switching period. The peak-to-peak value is about 150μ. In this view, two actuators are turned on and off (only one is shown) while the rest of the array is completely shut off.

the supply and it is approximated as an open circuit at RF. The inductance L2 is designed to be 30nH and C2 is determined such that the PAE is tuned to 900MHz. Using the lowest output power, the PAE generates 150μA (peak-to-peak) when driving a single coil actuator.

In Fig. 3.17, RFC represents a large on-chip inductor that provides a DC path from the supply and it is approximated as an open circuit at RF. The inductance L2 is designed to be 30nH and C2 is determined such that the PAE is tuned to 900MHz. The smallest current generated is 150μA (peak-to-peak, see Fig. 3.18) when the PAE is driving the coil actuator. In this case, only one transistor is being switched ON and OFF, the other 7 transistors are completely OFF. The PAE output spectrum is depicted in Fig. 3.19.

A simple ring oscillator, tuned at 900MHz, is chosen in this design to reduce the complexity of the system and minimize real-estate. Ring oscillators are known to fluctuate with temperature changes and drift with time, therefore, if necessary, one can replace it with a Phase-Locked-Loop synthesizer. This platform is intended for temperature controlled bio-

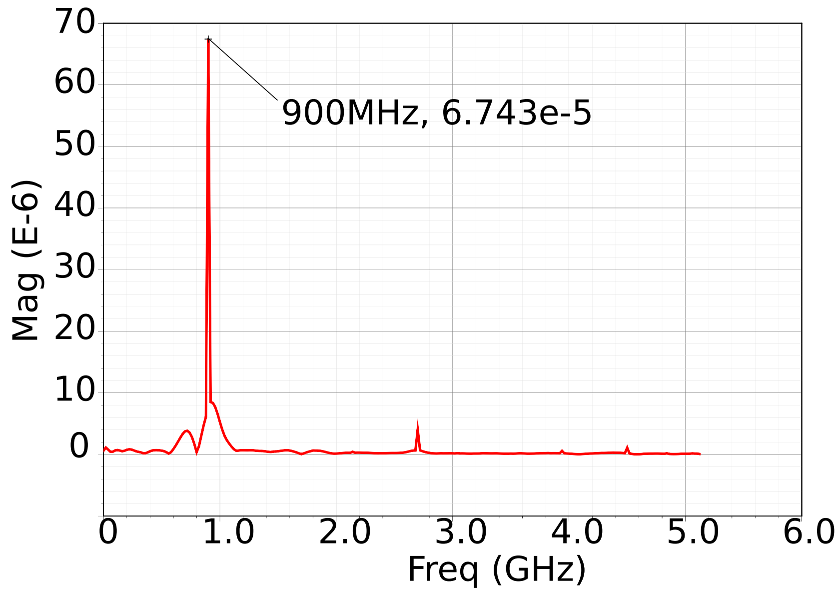

Figure 3.19: PAE output spectrum tuned at 900MHz. In order to minimize harmonic distortion outside the band of interest, the actuator impedance as well as the LC filter tank associated with the PAE are tuned to 900MHz

materials where the chip is assumed to operate around room temperature. The number of stages (gates) is chosen to be three, and the W/L sizes of each gate are adjusted to obtain an average delay of 0.10422ns tolerant to different variations in the fabrication process. The output frequency is given approximately as

$$f = \frac{1}{2 * N * T_d} \tag{3.3}$$

where f is the frequency, N is the number of stages and T_d is the (average) time delay per stage. Accordingly, f is calculated to be approximately 900MHz.

The Class E Power Amplifier described above is controlled by a 3-to-8 thermometer decoder, where the smallest possible input '000' translates to '00000001' output. This keeps the PAE turned on at all times unless the oscillator is switched off. Consequently, we have replaced the inverter in the first stage of the oscillator with an NAND gate, as shown in Fig.

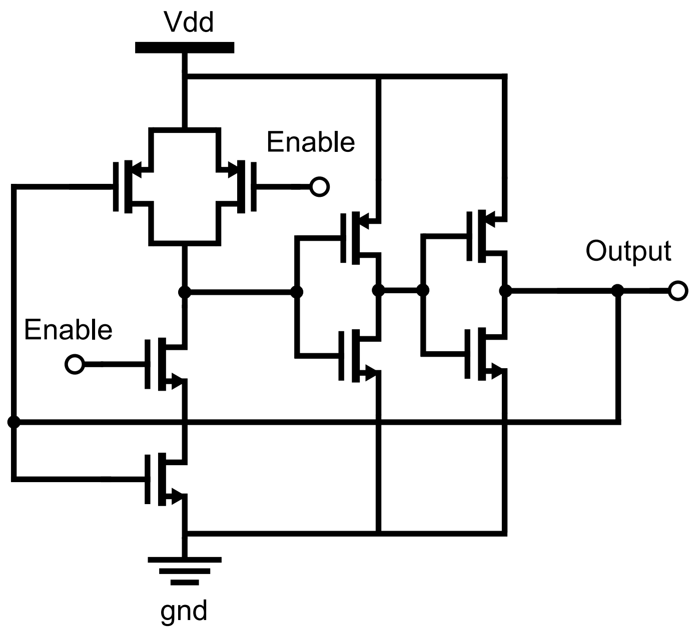

Figure 3.20: Min-sized, three stage ring oscillator with custom W/L to create an average delay of 0.10422 ns.

3.20, to allow switching off the oscillator and consequently, the PAE. Fig. 3.21 shows the average (DC component) of the periodic output of the PAE as a result of different switching intervals.

3.3.2 Digital Logic

Each cell in the 16x16 array needs to be accessed individually. Therefore, two 4-to-16 decoders are used to selectively link any inductor load to the driving circuits (the cross coupled LC oscillator and PAE). The decoders operate as in Random Access Memory (RAM) designs. Each input enables one of the sixteen rows and columns available. In order for the driving circuits to access a single coil cell, a high-speed control signal (switching at 40 MHz) is used to link a specific cell to the driving circuity. A dedicated switch consisting of 10 transistors is used to connect and isolate each coil in the array. The switch is built using an AND-gate for column/row selection and a tranmission-gate to pass the input/output signals.

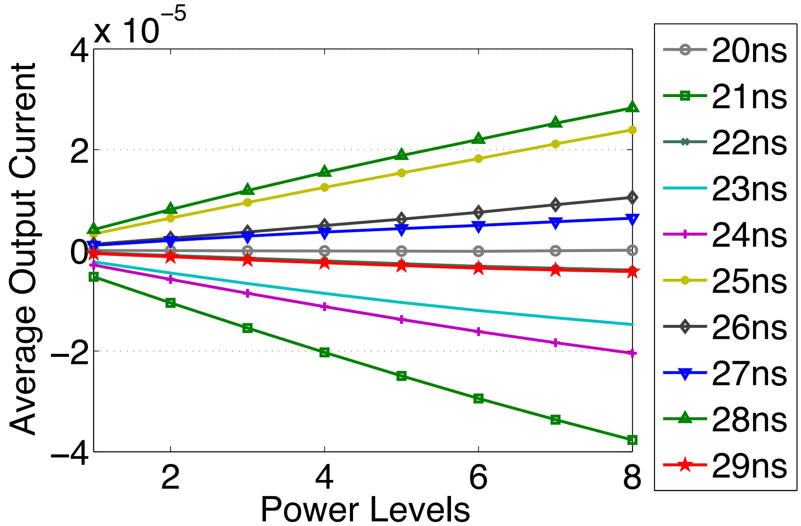

Figure 3.21: The average output current for different switching periods (20ns to 29ns). The magnitude is maximum at 28ns and 21ns switching periods.

If cross-talk and wire-loading is tolerated in an application, a much simpler approach can be adopted to minimize the size and logic of the control by replacing the 10 transistor switches with a single NMOS transistor. However, due to the noise and coupling generated by the neighboring cells, using NMOS switches exhibits negative influence on the performance of the array. Fig. 3.22 shows the performance of the 10-transistor transmission-gate switches in minimizing the cross-talk. In this simulation, a 3x3 block in the array was monitored. The center cell in the block is switched ON/OFF every 250 ns while all its 8 neighbors are switched OFF. The peak-to-peak current for the 8 neighboring cells is negligible (shown in red in the Figure) compared to the current of the center cell (shown in blue).

3.3.3 Actuator

The magnetic field generated in the array is proportional to the size of the inductor, the current passing through it, and the medium surrounding it. In this paper, the on-chip

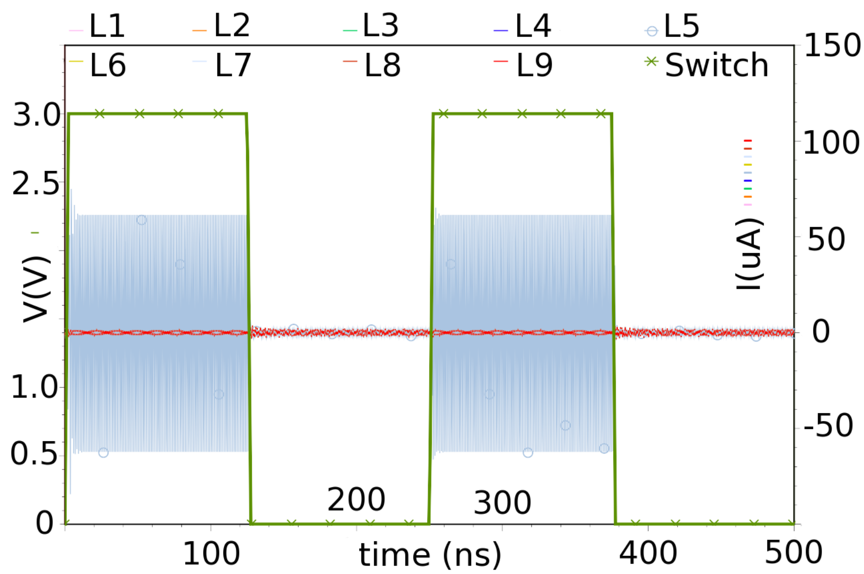

Figure 3.22: The center cell labelled L5 (blue curve) is being switched on and off every 250ns. The green curve depicts the logical switching activity on the transmission-gate switch and the other curves (shown in red) represent the currents going through the 8 neighboring coils. The magnitude of the current going through L5 dominates over the rest, in contrast of using a single switch which produces much more noise (not shown).

inductors were prototyped using all available 3 metal layers to constitute the smallest possible size in OnSemi 0.5μm CMOS technology. Each coil measures 6x6 microns in the plane with an inductance of 14.42495 pH and a resistance of 0.52μ Ohms. Fig. 3.23 depicts the tiny inductor. The 6x6 microns inductor was simulated to ensure the desired range of magnetic field output. The magnetic flux density generated is characterized (Fig. 3.24) with the assistance of an EM simulator (Ansoft Designer 4) using the proprietary technology parameters to ensure precision. The simulation shows that using the largest possible PAE current produces a magnetic flux close to 0.4mT.

Furthermore, a test circuit was fabricated to quantify the ability of these tiny inductors to manipulate magnetized objects. The test circuit consists of a 3-to-8 thermometer decoder controlling a PAE driving a mini-sized 6x6 micron coil. The passivation layer covering the coil has been removed to allow precise measurements. To measure the generated magnetic

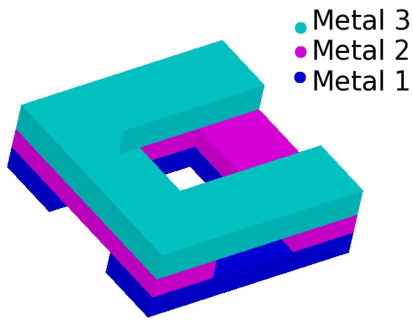

Figure 3.23: Three layered tiny coil 3D model. Each metal layer is designed as a “U” shape object.

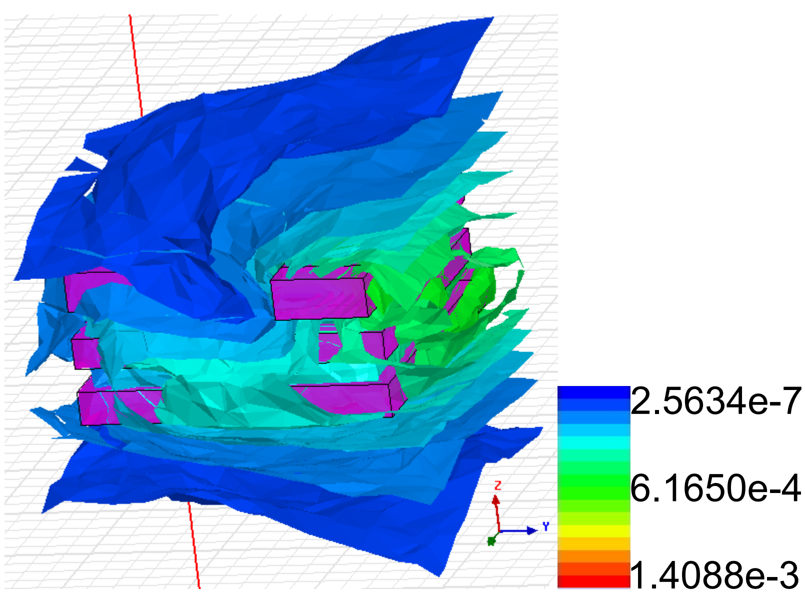

Figure 3.24: [3D Side view] Simulated magnetic field shown in green/blue as a result of passing 1.5mA through it (3 metal layers highlighted in pink). The B-field near the surface is approximately 0.4mT

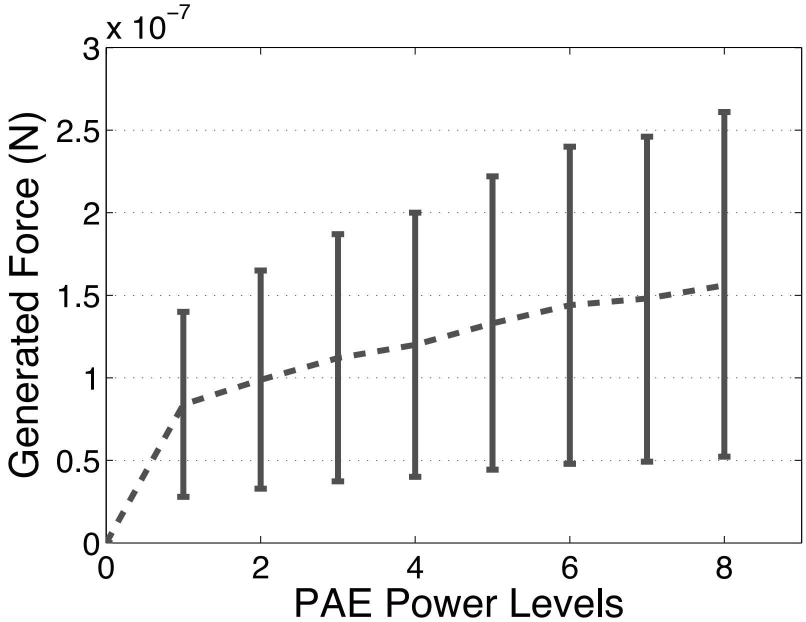

Figure 3.25: The forces (in Newton) generated on the cantilever tip by a single on-chip coil using different power levels. The error bars represents the variation in spring constants provided by the cantilever's fabrication house.

field of the fabricated coil, we have used an Atomic Force Microscopy (AFM) system with a magnetized tip (MAGT) fabricated by AppNano. The cantilever's tip height is around 15μm and its radius of curvature (ROC) is around 35nm. The cantilever's tip was placed on top of the "exposed" test chip.

The magnetic field of the coil has been detected by recording the measured deflection of the cantilever using the AFM optical laser sensor. The force exerted on the cantilever's tip is then computed. For each power level, we operated the AFM system to conduct 256 measurements which were then averaged. Therefore, a total of 2048 experimental runs were executed to measure 8 different (cantilever deflection) force levels. The experiment runs were separated by a 5 second timeout period to eliminate possible correlation between different driving power levels. In Fig. 3.25, the middle curve depicts the nominal magnetic field-generated forces for the 8 driving power levels.

3.3.4 Arrays

Integrating all components together on the same die requires careful considerations in terms of routing, isolation, and coupling among neighboring coil inductors. Moreover, careful considerations are due in terms of placement of RF and digital circuits with noisy sources, forming the array shape according to the targeted applications. The modular design should consider distributing heat equally across the entire array to maintain consistent interactions with the bio-objects of interest. Future versions will include on-chip temperature sensors. The overall system, shown in Fig. 3.26, has 3-degrees of flexibility: the shape of the array, different magnetic field levels per cell, and the array control scheme e.g. spiral, pyramidical, etc. Accordingly, with this flexibility, one can create collectively an arbitrary magnetic potential surfaces for manipulation. For example, it might be desired to generate a bowl shaped magnetic field using a square array. To that end, one can program the digital controller to set the edges of the array at maximum power '111' and reduce the power linearly along the X and Y axes in a gradient fashion toward the center of the square. More elaborate details on these schemes are the subject of future reports. As the switching control speed is about 40 MHz, time sharing is in fact used to power the desired configuration via multiplexing digital control, thus, requiring a single cross coupled LC oscillator for sensing and a single PAE for actuation.

A prototype array was fabricated in OnSemi 0.5μm 3M2P technology. For the first conservative design, we used the 1.5mmx1.5mm size for an array of 16x16 inductor cells. For different design rule CMOS technologies, one may adjust the design easily to accommodate the specific design rule constraints in selecting the small inductors and the corresponding arrays. The prototype is an asymmetrical 16x16 array suitable for singular and collaborative

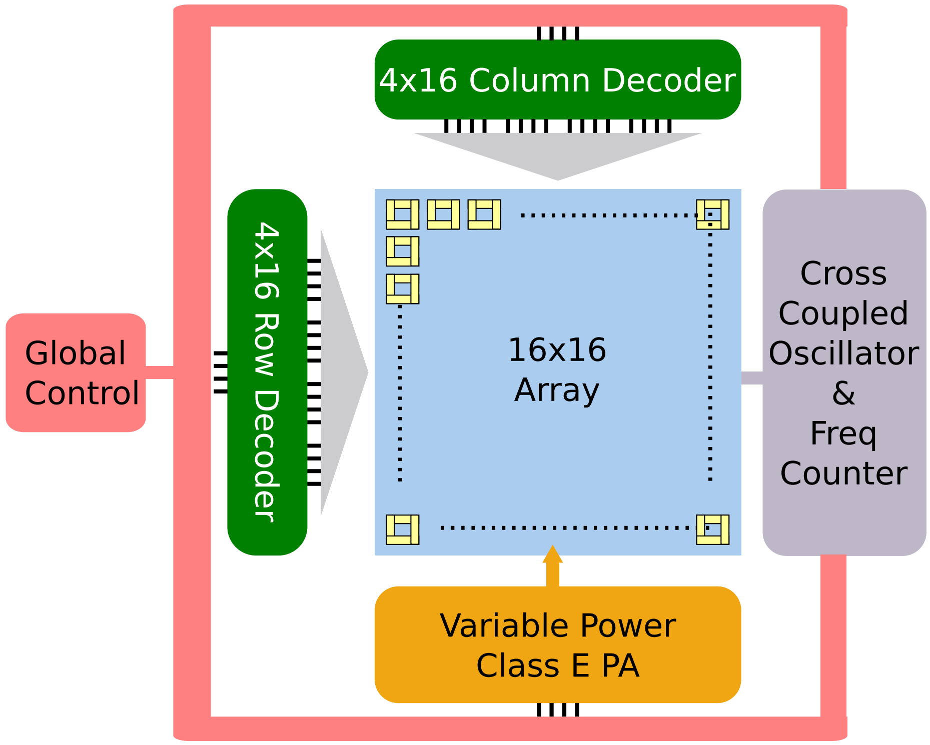

Figure 3.26: System block diagram. The global control is responsible for managing all building blocks to create the desired sensing or manipulation profile.

object manipulation with an estimated power consumption of 67mW. The distance between the center of any two neighboring cells on the same row is 93.450μm and the distance between two neighboring cells on the same column is 78.00μm. The array filled out the entire upper half of the die as shown in Fig. 3.27. The lower portion of the design, contains the PAE and digital control circuitry. The LC oscillator was not included in this run. The components have been intentionally separated and isolated to reduce coupling (cross-talk) and improve the performance of the actuation. The control logic can be applied directly to the chip from an external device using the I/O pins. Furthermore, the pad-frames on the upper half of the die have been removed to minimize the noise generated from the bonding wires and to allow it to be accessed from the upper half (for example via an Atomic Force Microscopy for testing) without damaging or shorting the I/O pins. The digital circuity and switching overhead

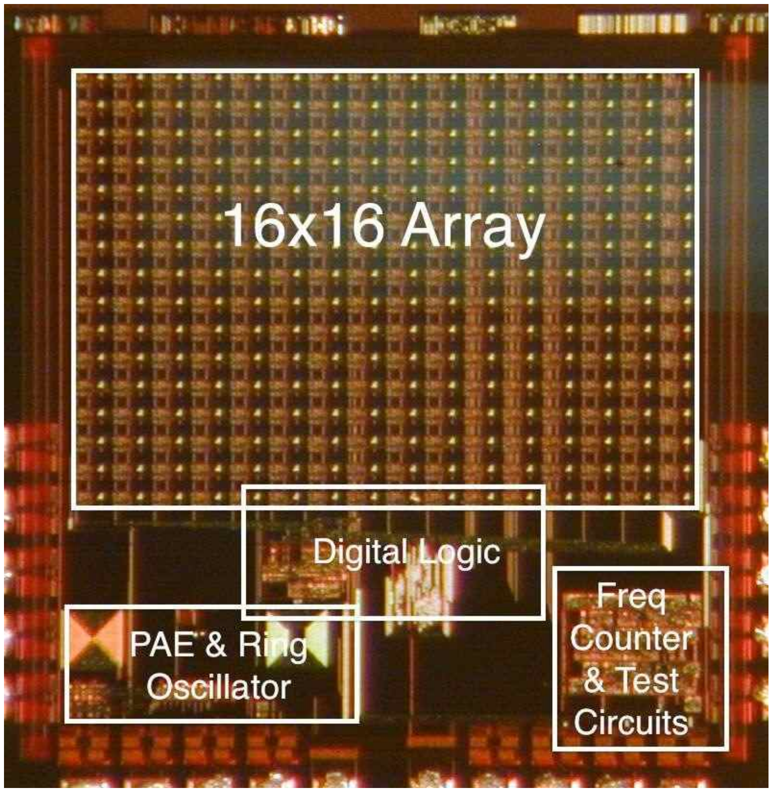

Figure 3.27: An annotated picture of the fabricated die: The RF components are placed far away from the array to reduce substrate injection and coupling. The I/O pads are removed from the 3 sides to permit easier testing.

occupies 51.450μmx34.5μm for this configuration. Finally, for future designs, the size of the actuators can be increased to increase magnetic fields to accommodate larger objects and beads. Accordingly, the driving circuitry and the PAE would need to be adjusted to properly to drive the new inductor loads.

A second design includes a symmetrical 16x16 array with some improvements. The difference between the two layout techniques is shown in Fig. 3.28. The digital overhead is reduced and occupies 38.4μmx32.7μm only. This is due to using a redesigned switching circuitry with a more compact layout. Another enhancement is that the overall area of the array is now 542.4μmx536.7μm which is 36% smaller than the one above. Finally, the distance between any two neighboring actuators (vertical or horizontal) is 33.6μm. This

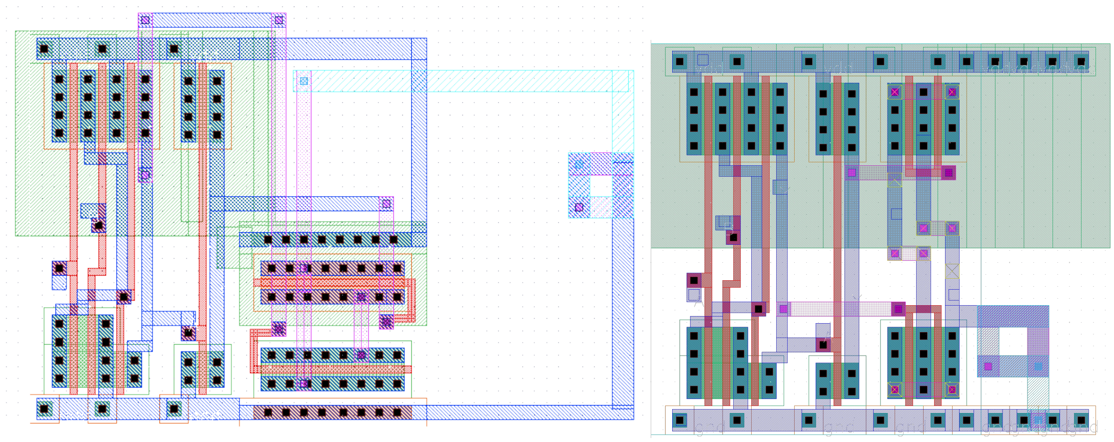

Figure 3.28: Comparison between two layout topologies.

compact symmetrical design allows easier controller programming, smaller die size and equal heat distribution. The power consumption for this array is estimated to be 60mW. Finally, it is possible to modify these arrays and move all the digital components to the die sides by creating a wide bus for the interconnects. This permits the coil array to be closely stacked and compact. However, careful component isolation to minimize coupling and noise would be challenging.

Last, a third design (shown in Fig. 3.29) includes a symmetrical 6x6 array with some improvements. First, the digital circuitry is moved to the side and the coils in the array are stacked as close as possible. Second, a redesigned digital switching circuitry is implemented with a more compact layout. The entire digital block occupies 200μm x 180μm. Third, the top most metal layer is used as a shield across the array to prevent stray magnetic fields from interfering with the manipulation process. Also, a poly layer is used to reduce substrate coupling with the coil array. Finally, the distance between any two neighboring actuators (vertical or horizontal) is 6.3μm. This compact symmetrical design allows easier controller programming, smaller die size and equal heat distribution. The power consumption for this array is 7.25mW in actuation mode and 1.9mW in sensing mode.

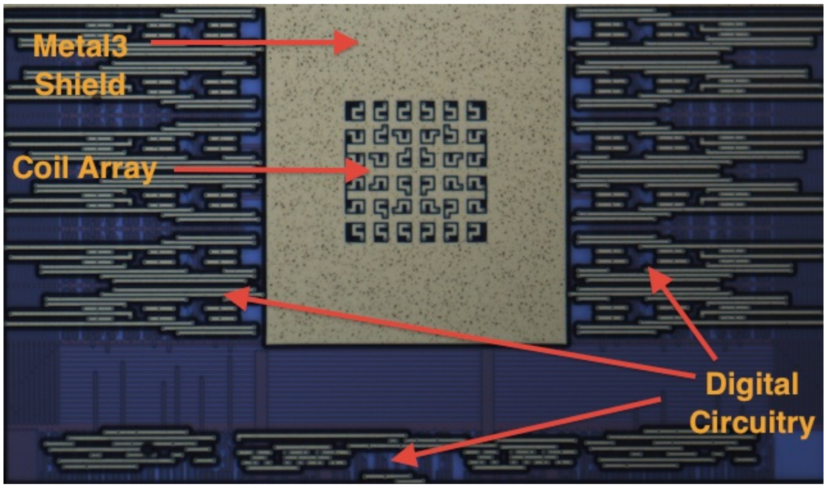

Figure 3.29: A micrograph snippet of the 6x6 array using 6x6 microns coils. The oscillator, PAE, and DC source are not shown. (20x magnification)

The shape and size of the array can be adjusted to meet the requirements of the application of interest. With the spatial array designs, one can create variable magnetic field profiles to enable steering one or multiple beads floating in liquid above the surface of the die to a final spatial destination. As an example, one may program the global controller to set the center coil of the array on maximum power '111' and reduce the power along the X and Y axes in a gradient manner toward the edges to create a pyramidal field shape. In this manner, if the control strategy steers a bead to a maximum magnetic field, then the bead(s) will be steered to the center of the array.

3.4 RF Sensing

3.4.1 Cross Coupled LC Oscillator

CMOS inductors' quality factor are very limited and since the linewidth of the impedance of the LC tank is determined by the quality factor, it is not possible to measure the impedance to achieve the sensitivity required for bio-sensing. However, for on-chip LC cross coupled oscillators the phase noise profile[18] will be significantly compressed compared to the tank impedance due to the virtual damping phenomena[66]. Therefore, a cross coupled LC oscillator is adopted to detect small magnetized particles. The active MOS components and the varactors (symbolized as variable capacitor) in Fig. 3.30 are shared across the entire array to save real-estate. The analog multiplexers facilitate the selection between actuation and sensing modes. Using the output frequency of the cross coupled LC oscillator, it is possible to monitor the change in resonance frequency when a magnetized particle in the order of 1μm is placed on top of the coil of interest. The method used in detection relies on the effective inductance of the vertical coil and its Q-value. For normal operations, the oscillation resonates at frequency $f = 1/(2\pi\sqrt{LC_1}) = 900$MHz. Nevertheless, when introducing a new medium, e.g a magnetic bead, on top of the vertical coil, its effective inductance is going to increase – resulting in a loss of resonance or a decrease in the oscillating frequency. Therefore, a simple integrated frequency counter is used to detect that change.

The 6x6 microns vertical inductor of 14.42pH requires a 2.168nF capacitor to oscillate at 900MHz (for this technology a simple poly-poly2 capacitor occupies 0.887 fF/μm^2) which is quiet large. Therefore, a custom poly-poly2 capacitor, appropriately sized cross coupled MOS transistors, and a tank of digitally controlled varactors are constructed for the LC oscillator. The W/L of the MOS transistors are adjusted for valid parasitics capacitance values. Also, the varactor tank is digitally controlled using 8-bits to calibrate the oscillator for different sensing paths. Moreover, the number of I/Os are reduced using a 3-to-8 thermometer decoder.

To verify the sensing abilities of the coils, we incorporate the Invitrogen MyOne Dynabead's model, using its physical specifications as well as the B-H hysteresis curves provided

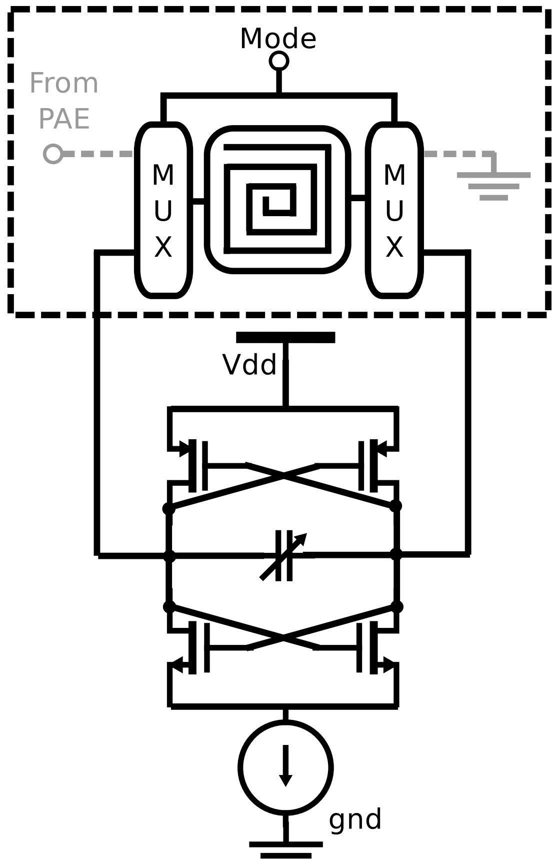

Figure 3.30: Cross coupled LC oscillator. The output frequency of the oscillator is also tuned at 900MHz. The variable capacitor is implemented as a varactor bank.

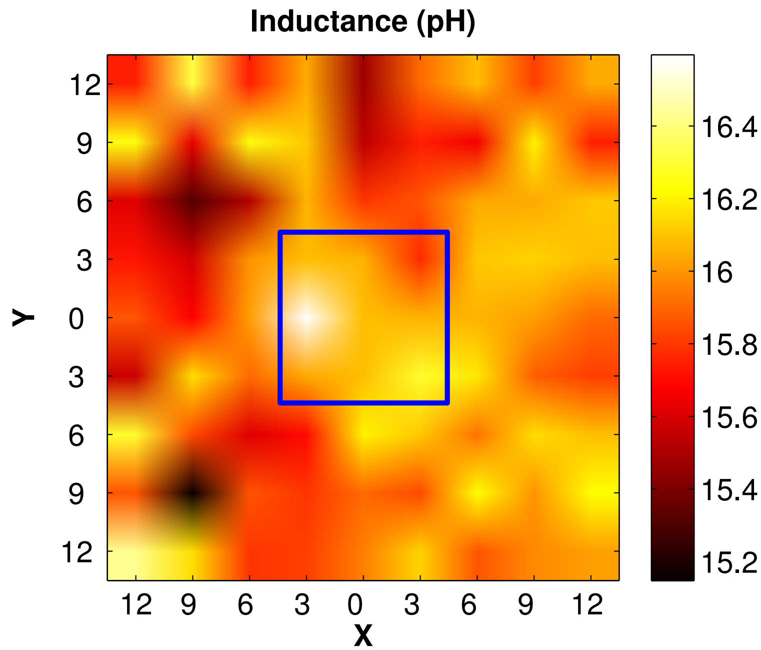

Figure 3.31: Computed coil's inductance based on the location of the bead in the X-Y plane. The coil is 6x6 microns, its center is located at (0,0) in the X-Y plane.

by the manufacturer, into an EM simulator (Ansoft HFSS). Then, we simulate the vertical coil with the bead suspended in distilled water. The simulation is swept over the spatial coil surface from (-12,-12)μm to (12,12)μm, in 3μm steps. The EM simulator subsequently recomputed the inductance of the vertical coil depending on the position (distance) of the bead with respect to the center of the coil. Fig. 3.31 shows that the maximum inductance occurs when the bead is located just above the coil. To verify this behavior another higher resolution simulation was carried out where the bead was re-positioned from (-3,-3) to (3,3) in 1μm steps and the maximum inductance was found at (-2,-2) as shown in Fig. 3.32. The simulations took one week to complete using Dual Intel Xeon X5460 3.16GHz 64bit with 64GB of RAM. Several simulations have shown that the oscillation frequency decreases below 900MHz (in shifts ranging from 0.5MHz to 5MHz). Such shift ranges are easily detectable by the frequency counter.

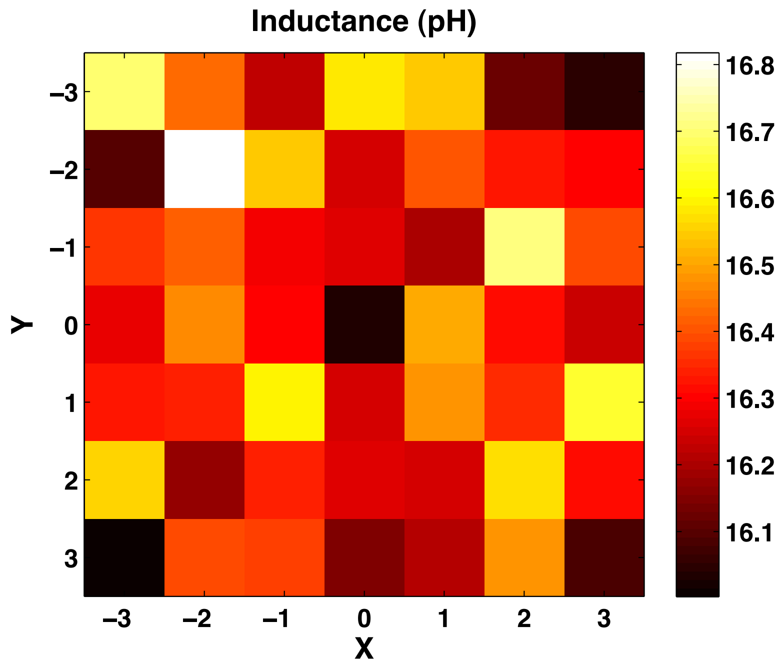

Figure 3.32: Zoomed coil's inductance just above the tiny coil. The location of the bead in the X-Y plane. The coil is 6x6 microns, its center is located at (0,0) in the X-Y plane.

The main advantage of this sensor is its relative small size compared to the sensed object of interest. However, due the fact that the Q value of this inductor is very low, the sensitivity is negatively affected. Therefore, another larger sensor adopted and is depicted in Fig. 3.33. In this design, the upper most metal layer (Metal3) is used for creating the spiral winding, Metal2 is used as an I/O bridge, Metal1 is used a ground, and Poly is used as a ground shield. Using patterned ground shielding we improved the Q value of the inductor by 2 folds. The resistance, Q, inductance plot is shown in Fig. 3.34. The circuit level model is shown in 3.35 and values of each component is expanded in table 3.2. This table summarizes most of the inductors used in this work. All parameters are self explanatory, however, SRF, is the self-resonance frequency of the coil.

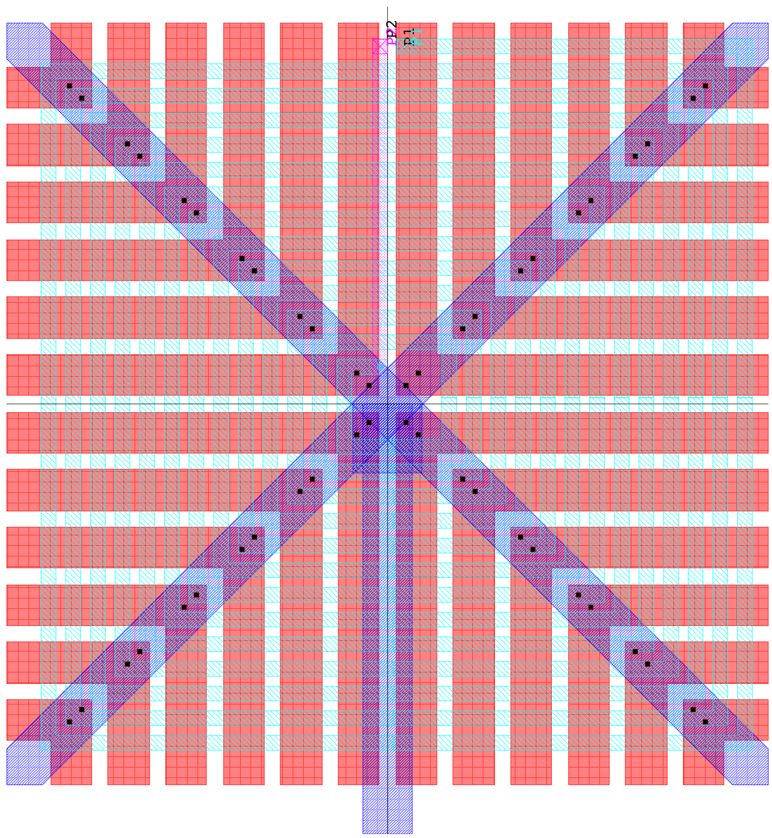

Figure 3.33: Layout of improved sensing on-chip inductor. Three metal layers were used. Metal3 for winding, Metal2 for exit bridge, and Metal1 for grounding.

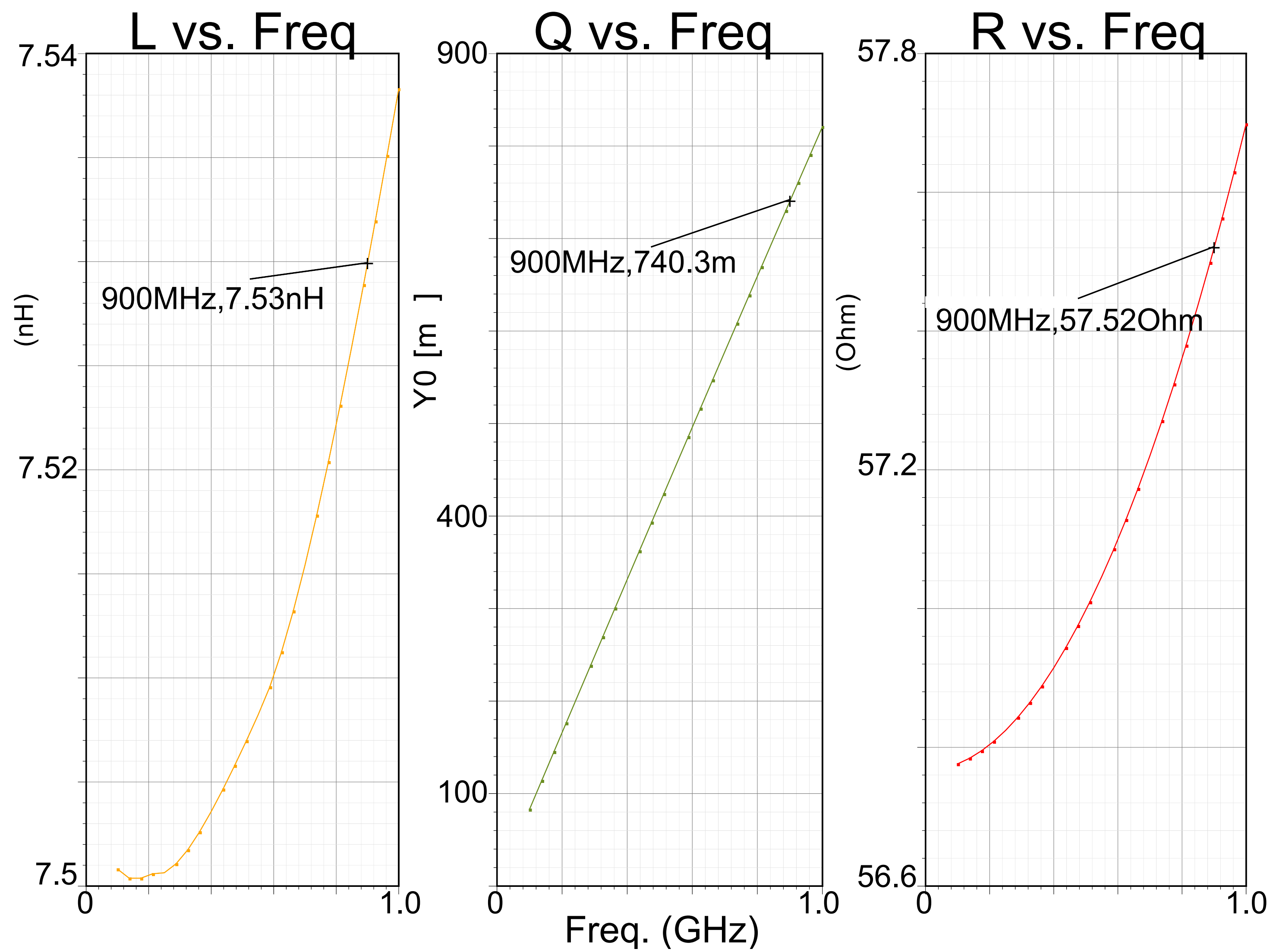

Figure 3.34: Inductor characteristic graphs. Inductance vs. Frequency, Q-value, versus Frequency, and Resistance vs. Frequency.

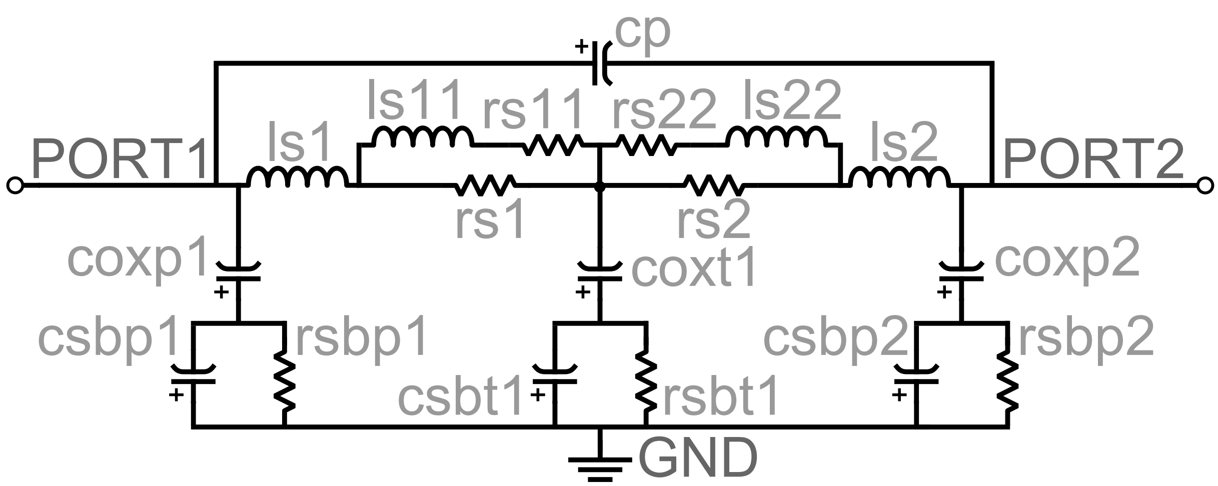

Figure 3.35: Schematic of the circuit level model of the inductor. Enhanced PI-model.

The phase noise and oscillation are simulated using Period-Steady-State Analysis (PSS) and the results of the improved phase noise is shown in Fig. 3.36. The oscillation range is 894.8MHz when the varactor input is 0000 0000 and 906.9MHz when the varactor input is 1111 1111. The frequency ranges are shown in 3.37. The startup time for the oscillator is estimated to be 13ns.

Table 3.2: Inductors used in this work and their parameters

Parameter	Inductor1	Inductor2	Inductor3	Inductor4	Inductor5
Turns	11.75	10.75	9.5	4	2.5
Inner Radius	3.6μm	18.6μm	15.5μm	63.4μm	54.9μm
Metal Width	3.1μm	1.8μm	1.8μm	15.1μm	20.0μm
Spacing	1.4μm	0.9μm	1.2μm	1.5μm	2.0μm
Frequency	900MHz	900MHz	900MHz	900MHz	900MHz
Inductance	7.675nH	10.07nH	7.08nH	5.5nH	2nH
Q-Value	1.07	0.379	0.328	6.539	5.337
SRF	8.97GHz	14.27GHz	18.07GHZ	11.47GHz	26.28GHz
Max Size	113.5μm	95.5μm	89.3μm	277.35μm	243.3μm
Top Metal	Metal3	Metal2	Metal2	Metal3	Metal3
Shield/GND	TRUE	FALSE	FALSE	TRUE	TRUE
cp	300pF	1.74fF	1.68fF	2.52fF	2.52fF
ls1	3nH	5.08nH	3.54nH	990pH	959pH
rs1	1KΩ	111.9Ω	91.33Ω	2.1Ω	2.07Ω
ls11	3nH	856.3nH	0.587nH	126pH	134pH
rs11	1KΩ	217.6Ω	177.66Ω	2.02Ω	1.96Ω
ls2	3nH	5.08nH	3.53nH	990pH	959pH
rs2	1KΩ	111.9Ω	91.3Ω	2.1Ω	2.07Ω
ls22	3nH	856.3nH	0.587nH	126pH	134pH
rs22	1KΩ	217.6Ω	177.66Ω	2.02Ω	1.96Ω
coxp1	500fF	18.1fF	15.75fF	31.1fF	32.4fF
coxt1	500fF	40.26fF	35.3fF	83.3fF	86.8fF
coxp2	500fF	22.16fF	19.54fF	24.4fF	25.4fF
csbp1	20fF	7.41fF	6.88fF	13.3fF	13.4fF
csbt1	20fF	16.48fF	15.42fF	24.3fF	24.69fF
csbp2	20fF	9.06fF	8.54fF	7.05fF	7.15fF
rsbp1	1KΩ	1.5KΩ	1.63KΩ	714Ω	705Ω
rsbt1	1KΩ	678KΩ	729.63Ω	390Ω	384Ω
rsbp2	1KΩ	1.23KΩ	1.32KΩ	1.34Ω	1.32KΩ

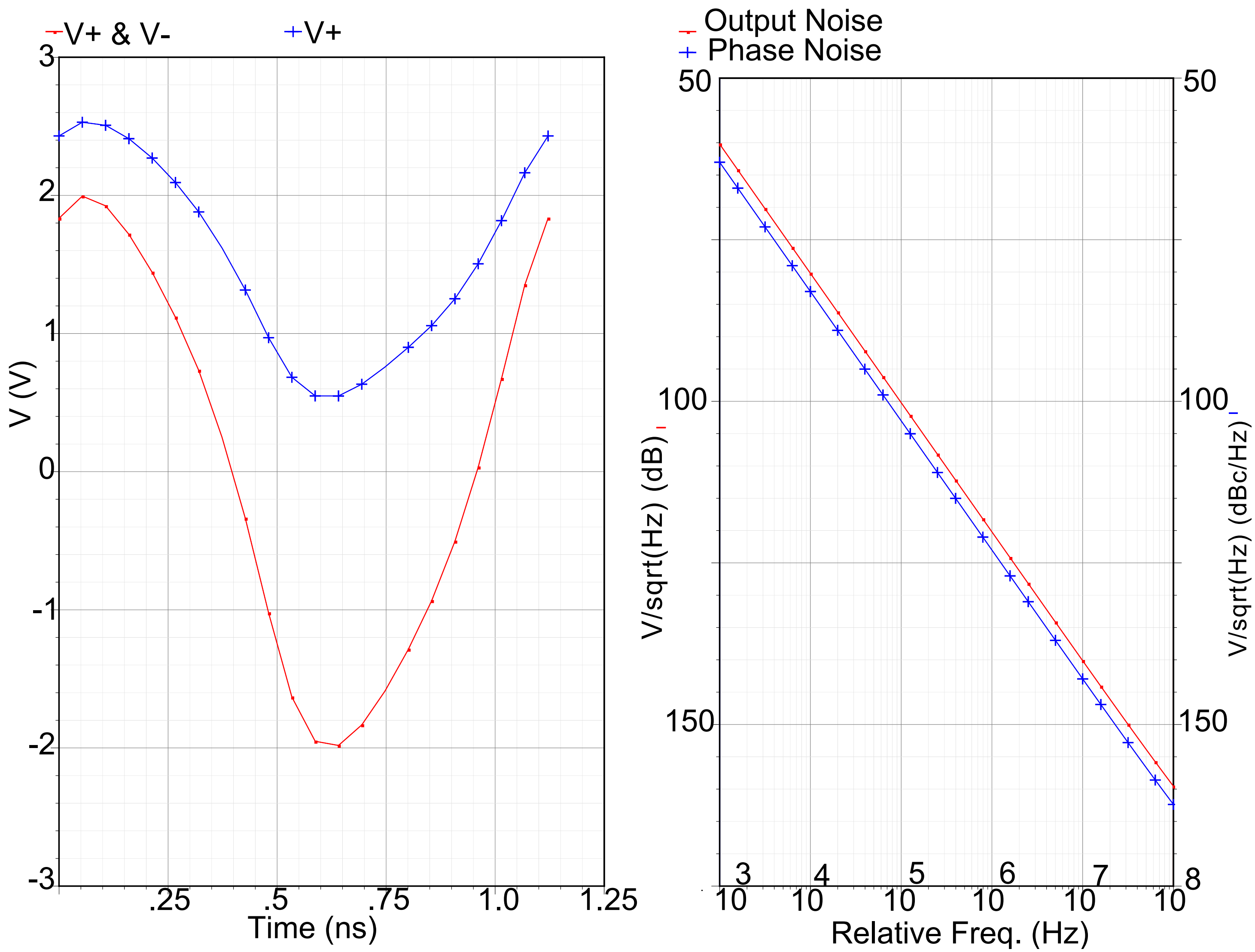

Figure 3.36: PSS simulation result. The phase noise and output noise are shown on the right figure.

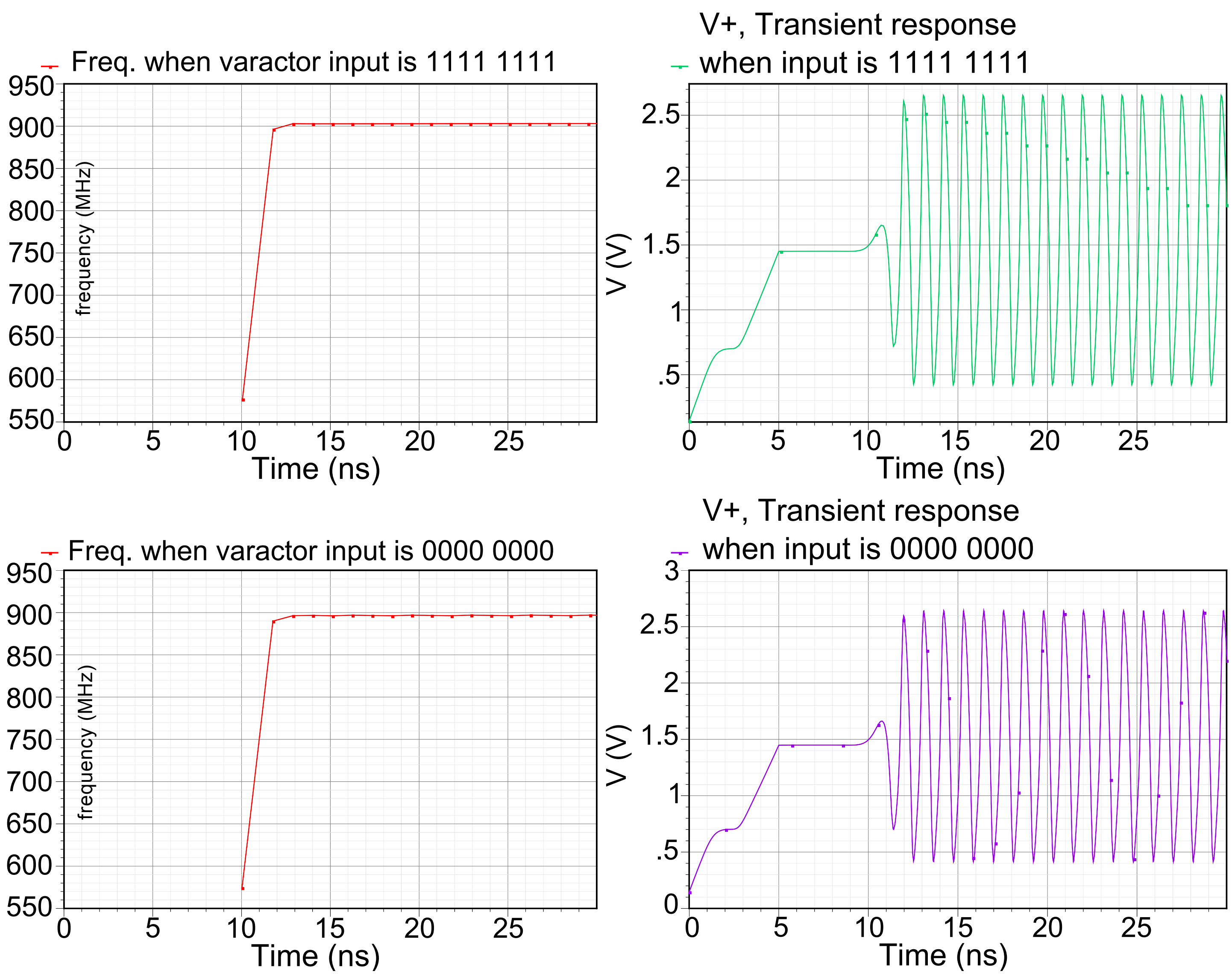

Figure 3.37: Transient response when the varactor is digital set at maximum and minimum capacitance.

A test circuit is fabricated to validate the simulation results. For the 6x6 coils the LC oscillator failed to start. The possible reasons of this failure are: it might be due to the very small Q-value of the 6x6 inductor, or it could be the way the coils are arranged in the array which might have caused the resistance of the path to the coil to become larger than the negative resistance of active MOS transistors. A second test circuit has another alternative sensing site (coil) with a dedicated LC to verify different oscillation schemes. The output of the alternative LC oscillator is connected to integrated counter which divides the high-frequency output of the LC oscillator down to 4.5MHz as shown in Fig. 3.38. The chip was running at VDD=1.8v and consumed an average of 1.5mA while in resonance. The peak-to-peak output of the oscillator is 1.3v. The output of the integrated counter is fed to a logic analyzer where it translated signals above 0.7V to logical one and below 0.7V as logical zero. A total of 4096 samples are recorded by the logic analyzer using a sampling frequency of 200MHz. The frequency spectrum of the output is shown in Fig. 3.39. Therefore, there are three possible states for the LC oscillator (a) oscillating at the resonance frequency (b) oscillating at a lower resonance frequency (c) no oscillation at all.

The detection approach can be summarized as follows (i) initially the entire chip is submerged in liquid. (ii) all coils across the array are sequentially switched and connected to the cross coupled LC oscillator for calibration. The varactors are then adjusted using the 8-bit digital control to tune the resonance frequency for the entire array based on the counter's output. (iii) when a bead lands near a coil, a shift in the resonance frequency will occur as seen in figure (3.39), curve labeled "Bead Present." (iv) alternatively, when a bead lands on top of the coil the oscillation might stop and the output of the oscillator would be a DC value close to VDD e.g. 1.8v. In general, the detector will output a logical "1"

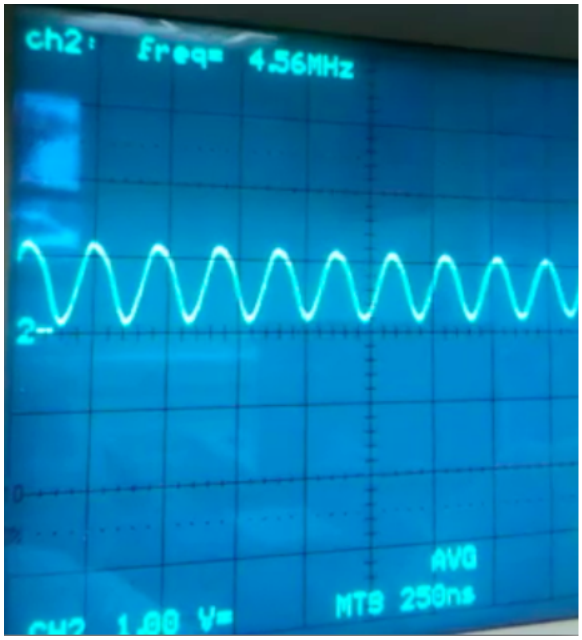

Figure 3.38: On-chip counter output using an oscilloscope.

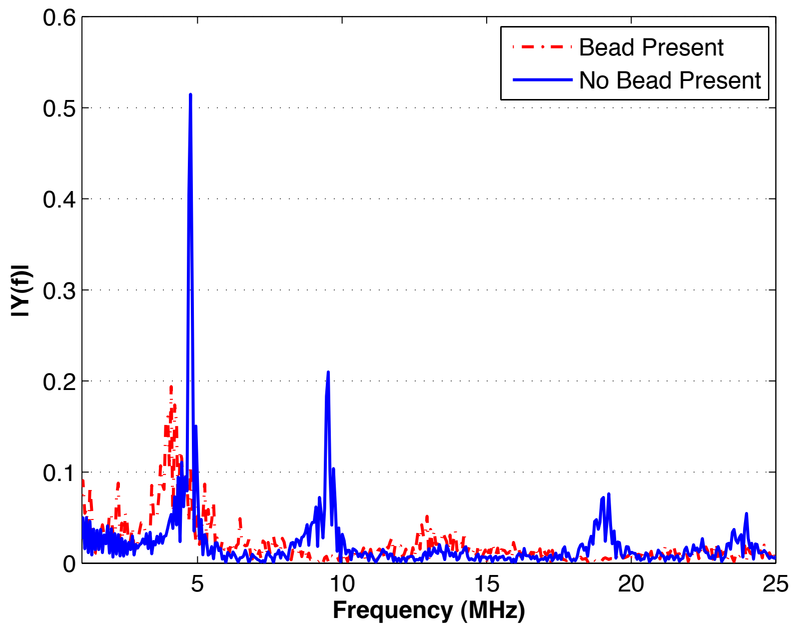

Figure 3.39: The blue curve represents the output when the chip is submerged in distilled water with no beads present. When a bead comes nearby the sensing sight a downshift of resonance frequency is observed. When the bead lies on top of the sensing site the oscillation is lost (not shown).

when there is no oscillation i.e. a bead exists above the coil and a logical “0” when there is oscillation. In future implementations, the correlation in frequency shifts across neighboring coils can be utilized to extract additional high-resolution information about the exact spatial location of the bead in the entire array.

3.4.2 Digital Logic

The digital logic used for sensing is the same logic used for the DC and AC modules. The high speed switches are utilized to connect any coil in the array to the sensing tank. A digitally controlled varactor is used to calibrate the resonance frequency when the device starts up. The varactor is made up using back to back PMOS transistors with binary increasing widths. A 3-8 thermometer decoder is used to adjust the capacitance needed for the tank to oscillate at a certain frequency. The resistance of the path is shown in Fig. 3.40 and it has to be compensated by a negative resistance using the active devices (NMOS, PMOS) in the cross coupled configuration.

The negative resistance for a single transistor can be approximated using first order square law equations. Or it can be simulated using Level=49 transistor SPICE Models. The transconductance (gm) of a PMOS device with Id = 1mA is shown in Fig. 3.41. There are many parameters to adjust in order to get proper oscillation. For example, the transistors has to be sized (W/L) correctly to guarantee stable oscillation. Using the DC simulation in the figure a designer has to calculate the total resistance of the tank (positive + negative). The net resistance has to be more negative for stable operations.

The value of gm is usually chosen to be 1.5 to 3 times [67, 68] more than the calculated or simulated values. Fig. 3.42 depicts the tanks conductance vs. three differently sized

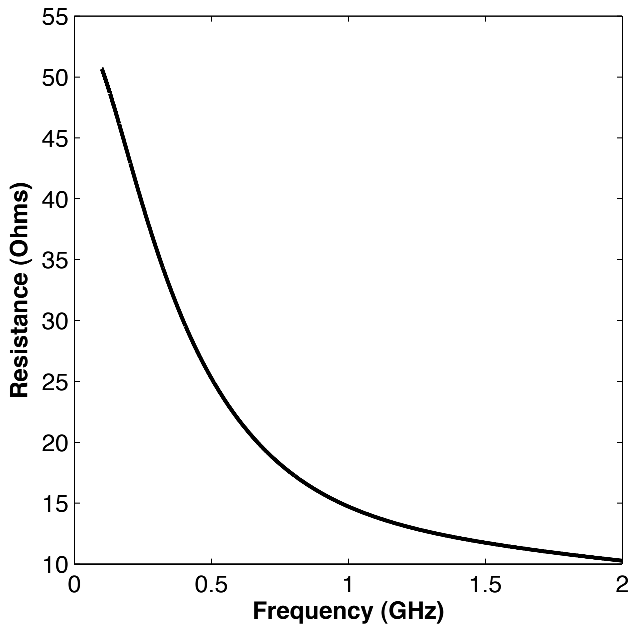

Figure 3.40: Tank resistance in ohms which needs to be compensated for using the active devices. This resistance includes the digital switches and the varactors.

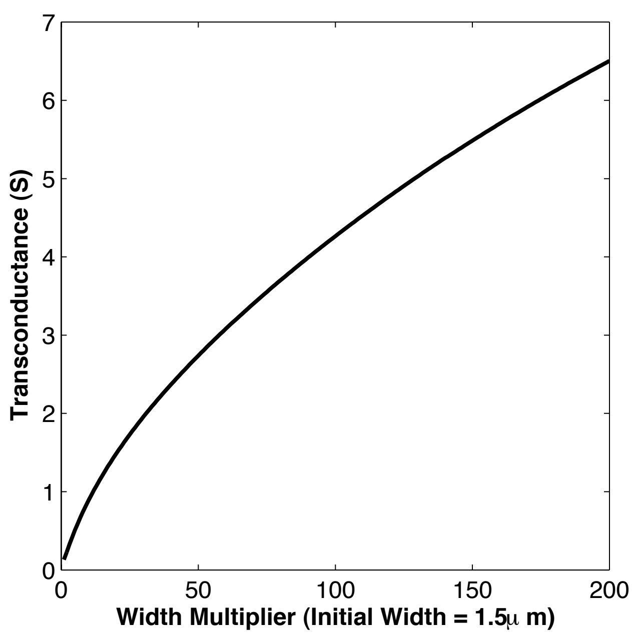

Figure 3.41: A DC sweep simulation of a PMOS device where the width of the device is incremented while keeping the source-drain current fixed. VDD is 3 volts.

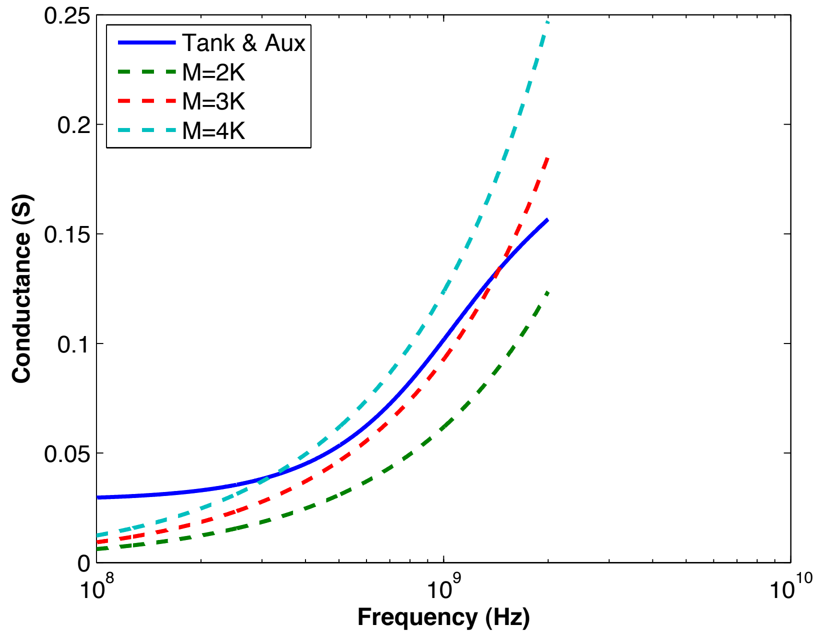

Figure 3.42: A simulation of 3 differently sized NMOS transistors to find the W/L ratio which will create a proper gm to overcome the inductor's.

NMOS transistors. The variable M represents the multiplier used in the simulation for the transistor. For example, if M=1000 then the actual width of the transistor is 1.5 microns * 1000 = 1500 microns. The simulation shows that for a frequency range between 800MHz and 1GHz the dashed blue cover, labeled, M=4K or 4,000 the gm of the transistor overcomes that of the tank. In order to layout these huge transistors, multi-fingered transistors are realized.

3.4.3 Arrays

Sensing arrays are designed the same way as the DC, and AC arrays. However, other considerations are due to guarantee oscillation on all inductors/coils in the array. First, the inductor itself has to be designed correctly as previously discussed. The Q-value of the inductor has to be between 5-10, the higher the better. The conductance of the active components of the LC-cross-coupled oscillator has to compensate for the worst case inductor routing. Therefore, a simulation is performed to calculate the impedance of the entire path to the coil array. Fig. 3.30 depicts the simplified path, however, each coil has two analog multiplexers and two analog switches connected to its ports. To measure the impedance and the conductance, an AC source is connected to the tank of a 3x3 sensing coil array. Fig. 3.43 shows the conductance that needs to be compensated at 900MHz. The coil used in this simulation is Inductor4 in table 3.2 The transistors' W/L in the switches and the multiplexers are configured wide (width is 43.95 microns and the multiplier is 20) to reduce the resistance of the path. Additionally, once they are shared with other modes (i.e. DC mode) they have to accommodate large amounts of currents. The active components (NMOS and PMOS) has to be sized accordingly to produce a gm that is 1-3 times larger than the tank's. Fig. 3.44 shows a DC simulation of an NMOS transistor with its source connected to DC voltage of 0.7mV to compensate for the NMOS's body effect. The width of the transistor is swept from 50 to 60 (x 1.5μm) and the drain source current is fixed at 15mA. Fig. 3.44 shows the DC simulation of the PMOS transistor which matches the NMOS's gm. However, the source is not connected to a DC voltage, it is connected directly to ground. The width of the transistor is swept from 95 to 105 (x 1.5μm) and the drain-source current is also fixed at 15mA. Finally, in order to fix the active transistors' source-drain current at 15mA a tail-current source is realized as a NMOS transistor. The width of the transistor is 9μm and the width multiplier is 100. Fig. 3.46 shows a DC simulation on the tail NMOS transistor to generate 15mA. Approximately, by applying 1V at the gate the transistor would provide 15mA IDS. Additionally, the tail transistor is not connected to a current mirror to facilitate testing. A user can connect a programmable voltage source to the tail NMOS transistor to

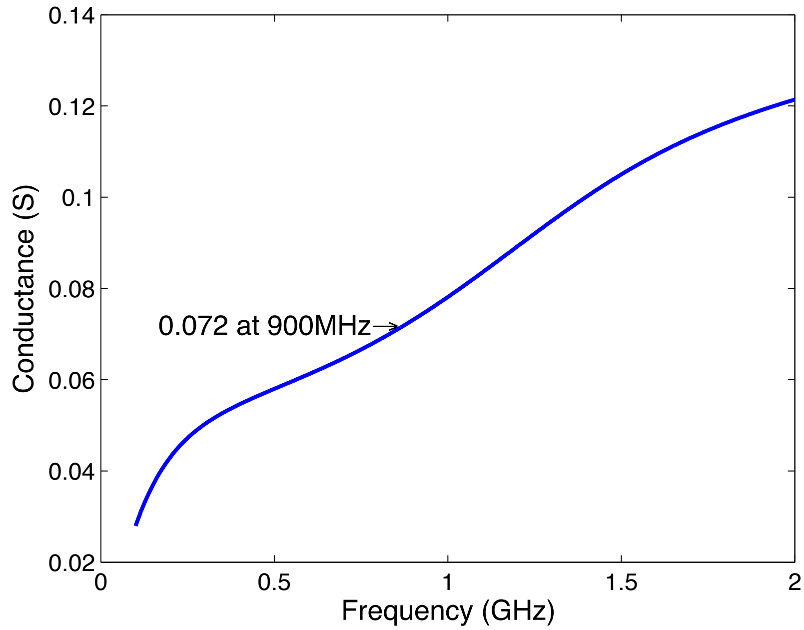

Figure 3.43: An AC simulation running at vdd=1.8v to find the conductance of *Inductor4*, two analog multiplexers, and two analog switches.

adjust the amount of current driven through the tank.

A lab experiment is conducted to test the sensing capability of the coil arrays. The chip is submerged in deionized water with no beads present initially. Then two beads were placed on 2 neighboring coils in the array. The array is set to sense the location of two beads. Coil (0,0) doesn't have any bead, coil (0,1) has a bead lying on top of it, coil (0,2) has a bead lying close to the center, coil (0,3) and (0,4) don't have beads on them. Fig. 3.47 shows the output of the frequency counter connected to the LC-Oscillator. The coils are multiplexed to detect beads. Coils (0,0), (0,3), and (0,4) don't show any major shift in frequency therefore, there is no bead present. Coil (0,1) shows a downshift in frequency, and (0,2) is not oscillating at all which means there is a bead on it. The mean frequency of oscillation when there is no bead present is 4.8017 MHz with a standard deviation of 0.0704. The downshift in frequency when adding a magnetic bead on top of the coil is approximately

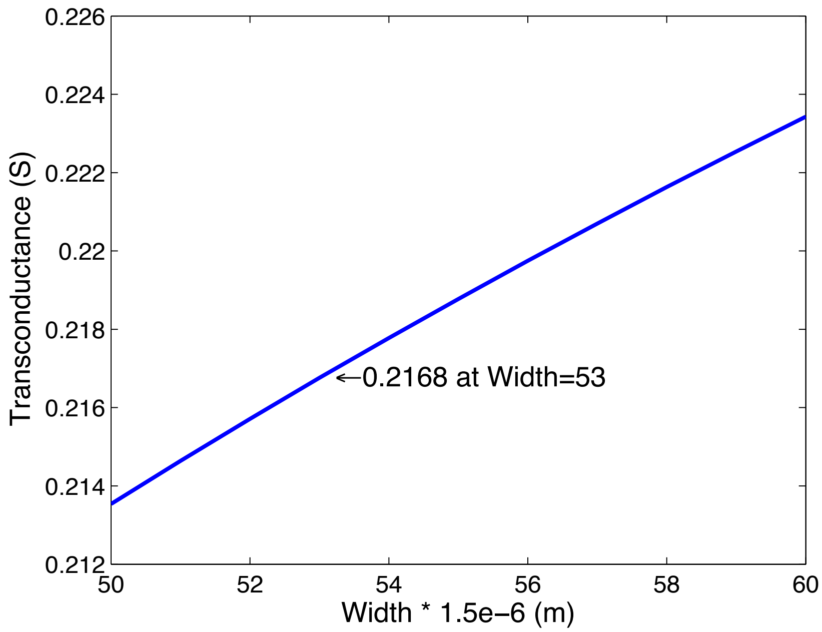

Figure 3.44: A DC simulation running at vdd=1.8v to find the transconductance (gm) of a NMOS transistor. The source is connected to 0.7V to realize the body effect.

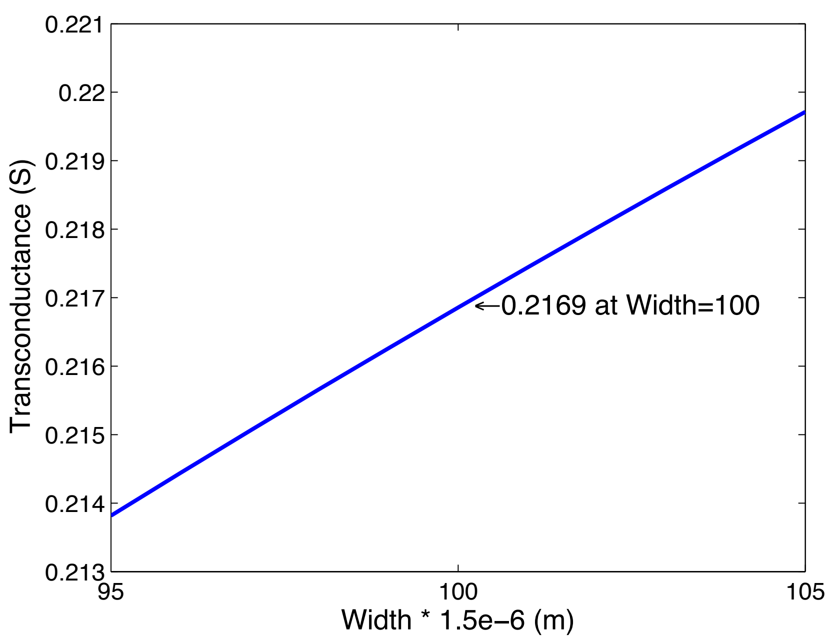

Figure 3.45: A DC simulation running at vdd=1.8v to find the transconductance (gm) of a PMOS transistor.

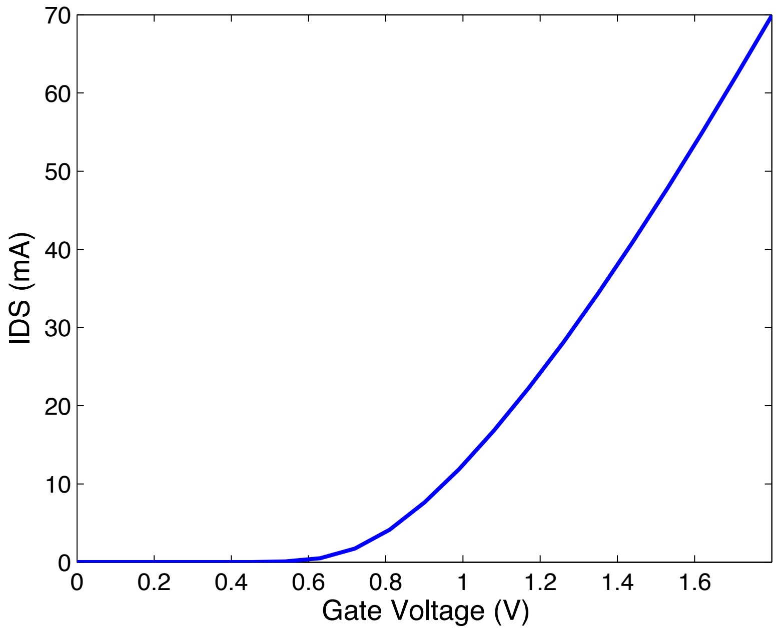

Figure 3.46: A DC simulation running at vdd=1.8v to find the voltage at which the tail NMOS transistor provides 15mA.

0.7127 MHz. The detection algorithm is described at the end of subsection 3.4.1. Finally, the sensing sensitivity in the 8x8 is not performing as expected. There are some issues when scanning the entire array for beads. There are some inductors in the array which refuse to start oscillating even when there is no bead present on top. This is due to, low Q-value of inductors, long interconnects between the active component and the coils, coupling between neighboring coils. These issues are further investigated in a dedicated chip, shown in Fig. 3.48, that is currently being fabricated.

3.5 Tri-mode System

A dedicated CMOS chip to run all actuation and sensing modes, on the same die, is fabricated. It supports three modes of operation (Sensing, AC actuation, DC actuation) on

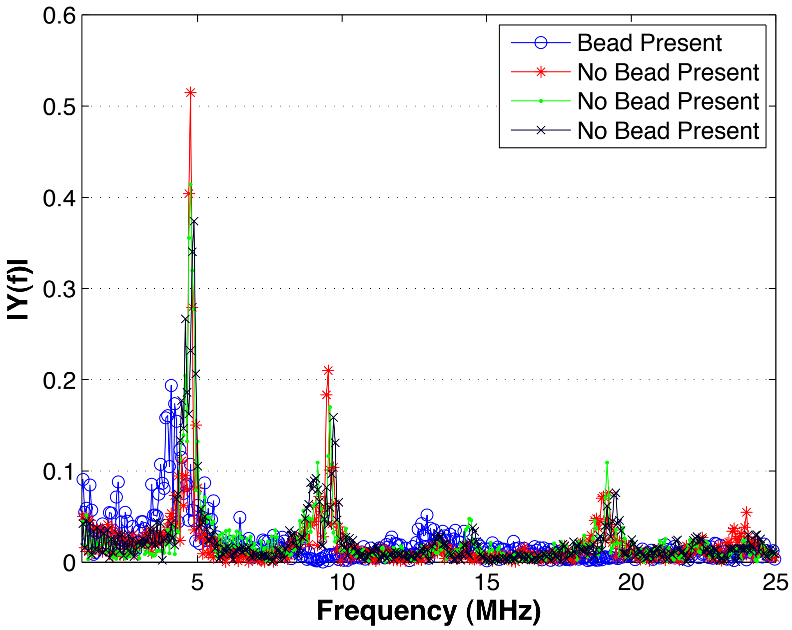

Figure 3.47: 5 Coils in the array are scanned to sense magnetic beads. One coil detects a bead when the output frequency is downshifted. The other coil stop oscillating (curve not shown), and the other three coils have the same frequency output.

the same chip. A system level block diagram is shown in Fig. 3.49, the array size can be chosen arbitrarily based on the available real-estate on the die. The column/row decoders need to scale according to the size of the array. If the array is symmetrical, standard cell decoders can be used to access each cell in the array. In order to reduce, the number of pad-frames, bonding wires, and I/Os 3-8-thermometer decoders are utilized. Each module of the sub-components (DC/AC/SENSING) accepts an 8-bits level configuration. The DC current source can generate 8-level DC currents, the class-e amplifier can generate 8-power outputs, and the oscillator has an 8-bit varactor to adjust the capacitive load in order to tune its output frequency. All of these modules are multiplexed using a wide analog multiplexer as discussed in the DC, AC, RF sections before. Finally, the global control is responsible for coordinating all the components to create seamless pseudo-parallel operation, where a user

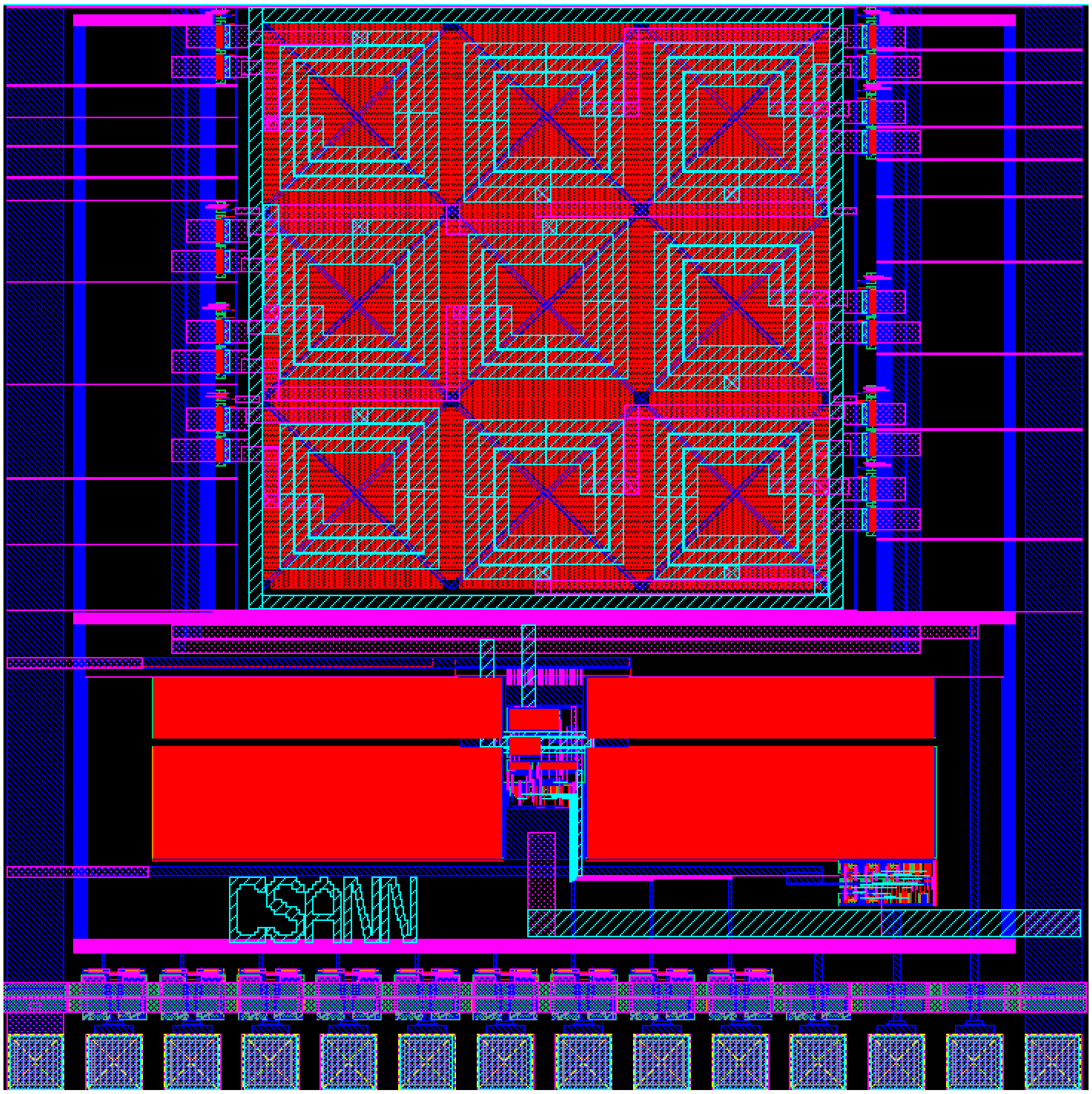

Figure 3.48: A 3x3 coil array with improved inductors Q-value and sensing isolation.

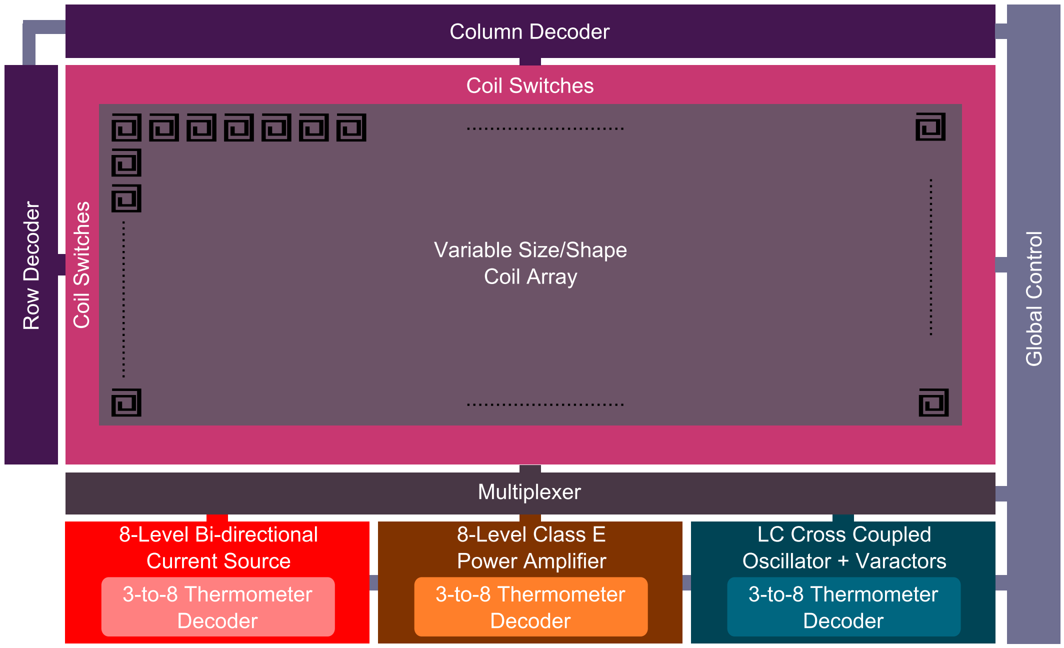

Figure 3.49: System block diagram for tri-mode operation.

can sense and actuate objects up to 40MHz.

In order to switch between different modes we utilized the high-speed switches designed in the previous section as shown in Fig. 3.4. The high-speed switches use the smallest possible transistor length for both NMOS and PMOS transistors. The width for the transistors is 43.95 microns and the multiplier is 20. The gain for the switch is plotted in Fig. 3.51. At 900MHz the gain is 99.55%, which implies that the amplitude of signal passed through it is not affect it.

Moreover, when switching between the DC and RF sensing modes, the startup time for the oscillator is considered the limiting factor. However, the startup time for the LC oscillator implemented, as discussed in section 3.4.1, is 13ns which is more than enough in a 40MHz (250ns) cycle. Therefore, it is possible to simultaneously manipulate and monitor magnetic beads by quickly alternating between the DC and RF sensing modes.

All of the components discussed in the AC, DC, and RF sections where carefully inte-

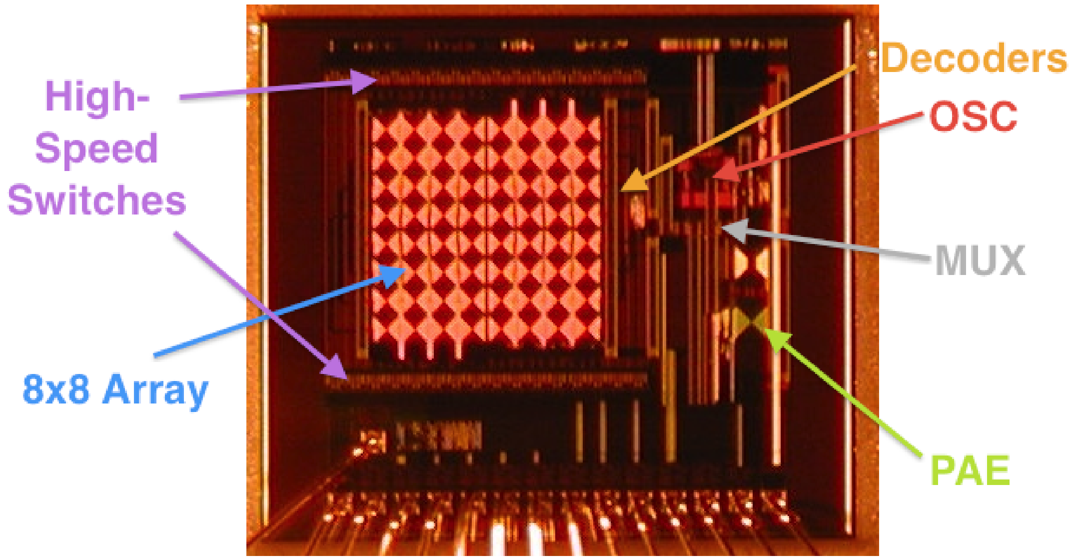

Figure 3.50: A micrograph of the tri-mode system.

grated and fabricated. A die photograph is shown in Fig. 3.50. The size of the die is 1.5mm x 1.5mm the size of the array is approximately 740μm x 740μm, the digital overhead is 400μm x 1000μm, and the share DC, AC, and RF modules are 460μm x 900μm.

Finally, the lab experiments in the previous sections were mainly conducted using the tri-mode chip except for the AC experiments and the 30x30 μm DC experiment. The 80x80 coils where we did the DC pseudo-parallel manipulation and RF sensing were in fact part of the tri-mode system.

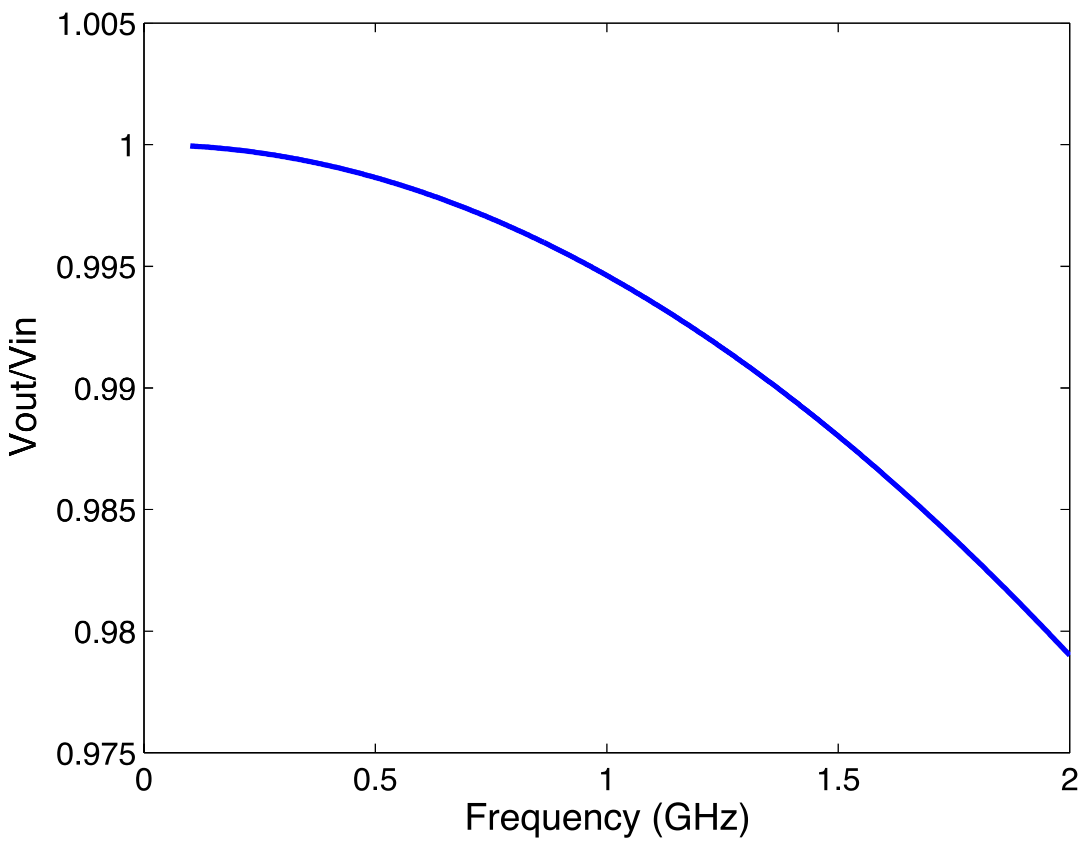

Figure 3.51: The frequency response of the large switch. The output voltage divided by the input voltage.

Chapter 4

Magnetic Bead Control

We have introduced in previous chapters multiple platforms to manipulate and sense magnetic micro-beads in the size order of 1μm. These platforms use DC and/or AC electric currents for manipulation, on-chip RF oscillators for sensing, and an open-cavity device for low-cost packaging. In this chapter, we develop a second-order dynamic model for the bead and implement a tailored closed-loop PID controller for precise micro-bead manipulation using the on-chip sensors and actuators. The second order model includes the micro-beads' inertia, crucial for precise transport, which is often neglected in the literature, e.g., [11, 4, 17]. Also, the controller does not use any visual feedback, as in [11], or external optical sources, as in [17], for its sensing modality. In contrast, the entire coil array is utilized by selectively addressing any single coil and using such coil in time-multiplexing mode to sense and actuate the bead(s) for seamless pseudo-parallel operations.

4.1 Micro-Beads Motion

Standard Cartesian coordinates are adopted so that the coil array (and thus the substrate surface) form the $x - y$-plane, and the z-axis is normal to the substrate surface. Standard Spherical coordinates may also be invoked as commonly used in the literature.

4.1.1 First-Order Translational Motion

1D (1-dimension) and 3D first-order models for translational motion of a bead on the surface of a micro-coil array are now presented. The 1D model is a result of reducing the 3D model by limiting the translational movement to the x-direction only. The equations developed for the first-order model are based on [4]. We begin with the magnetic potential energy, say U, for trapping a magnetic bead, given as

$$U = -\frac{1}{2}\mathbf{m} \cdot \mathbf{B}, \tag{4.1}$$

where $\mathbf{m}$ is the magnetic moment vector of the bead and $\mathbf{B}$ is the (external) magnetic flux density. The moment is expressed as

$$\mathbf{m} = \frac{\chi V}{\mu_0}\mathbf{B}, \tag{4.2}$$

where V is the volume of the bead and χ its magnetic susceptibility. Therefore, the magnetic force becomes

$$\mathbf{F}_m = -\nabla U = \frac{1}{2}\frac{\chi V}{\mu_0}\nabla B^2, \tag{4.3}$$

Next, any object moving through a fluid encounters a hydrodynamic resistance which opposes its motion. This resistance is called the drag force, and it is directly related to the viscosity of the medium the object is traveling in. Assuming that the bead is a perfect sphere moving in a medium with a low Reynolds number (R_0), the drag force $\mathbf{F}_d$ is approximated as

$$\mathbf{F}_d = -6\pi r\eta\mathbf{v} \cdot f_D, \tag{4.4}$$

where r is the radius of the bead, η is the dynamic viscosity of the fluid, and f_D is the drag coefficient. $\mathbf{v}$ is the velocity of the bead relative to the fluidic environment and is expressed as

$$\mathbf{v} = \left(\mathbf{v}_b - \mathbf{v}_f\right), \tag{4.5}$$

where $\mathbf{v}_b$ is the velocity of the bead and $\mathbf{v}_f$ is the velocity of the fluidic flow. Since there is no fluidic flow in open cavity devices, $\mathbf{v}$ is equal to the absolute velocity of the bead.

Finally, the normal force $\mathbf{F}_n$ on a bead with mass m_b is

$$\mathbf{F}_n = m_b \begin{pmatrix} 0 \\ 0 \\ -g \end{pmatrix}, \tag{4.6}$$

where g is the gravitational acceleration. As a result, the total forces acting on the bead is

$$\mathbf{F}_m + \mathbf{F}_d + \mathbf{F}_n = 0. \tag{4.7}$$

The 3D equation can be simplified to 1D since the plane of interest is $x - z$-plane [4], therefore, the final form of translational velocity for the controller is

$$\dot{x} = \frac{m}{6\pi\eta r f_D}\left(\frac{\partial B_x}{\partial x}\sin\theta + \frac{\partial B_z}{\partial x}\cos\theta\right) \tag{4.8}$$

4.1.2 First-Order Rotational Motion

Rotation is caused by torque, which is the magnetic torque $\mathbf{N}_m$ and the torque caused by viscous drag $\mathbf{N}_d$. When modeling the 3D rotational motion we assume the rotational axis along the three Cartesian axes are: (i) $\dot{\beta}$ (i.e. the rotation along the x-axis), (ii) $\dot{\gamma}$ (i.e. the rotation along the y-axis), and (iii) $\dot{\kappa}$ (i.e. the rotation along the z-axis.) Therefore, the rotation around the $x-z$-plane is

$$\dot{\theta} = \frac{m}{8\pi\eta r^3}\left(B_x\cos\theta - B_z\sin\theta\right) - \frac{15}{256r}\dot{x} \tag{4.9}$$

4.1.3 Second-Order Translational Motion

According to Newtons second law, a body of a known mass subjected to a force undergoes an acceleration. This acceleration is often neglected due to the mico-bead's small mass, as a result, the inertia of the bead is ignored. For precise control strategy a second order model is developed to accommodate the inertia. The sum of all forces applied on a bead is

$$\mathbf{F} = m_b \cdot \mathbf{a}, \tag{4.10}$$

where m_b the mass of the bead and **a** the acceleration of the bead. Therefore, the 1D equation of $\ddot{x}$ [69] is

$$\ddot{x} = \frac{m}{m_b}\left(\frac{\partial B_x}{\partial x}\sin\theta + \frac{\partial B_z}{\partial x}\cos\theta\right) - \frac{6\pi\eta r f_D}{m_b}\dot{x} \tag{4.11}$$

4.1.4 Second Order Rotational Motion

The second order rotational torque is assumed too small to be included in the control strategy, therefore, it is neglected.

4.1.5 First-Order vs. Second-Order

Now, we compare the first-order dynamic model of a bead to a second-order model when the bead is traveling between two wires. The distance between the two wires is 10 μm. Initially the bead is trapped on "wire 1" by supplying 100mA DC current through it. Then at t=1 "wire 1" is switched off and "wire 2" is switched on by passing 100mA through it. Fig. 4.1 depicts the simulation result of this operation. Clearly, there is a difference in the behavior of the bead when modeled with inertia. For the 1st-order model the bead almost instantaneously reaches 90% of its destination to "wire 2" when it is switched on, while it takes the 2nd-order model almost two seconds to reach the same point.

4.2 On-Chip Coil Model

The CMOS technology used in this work does not allow "non-manhattan" shaped metals. Consequently, square spiral coils are developed in this design. In order to compute the magnetic flux density, thus, the magnetic force, we apply the Biot-Savart's law for each wire

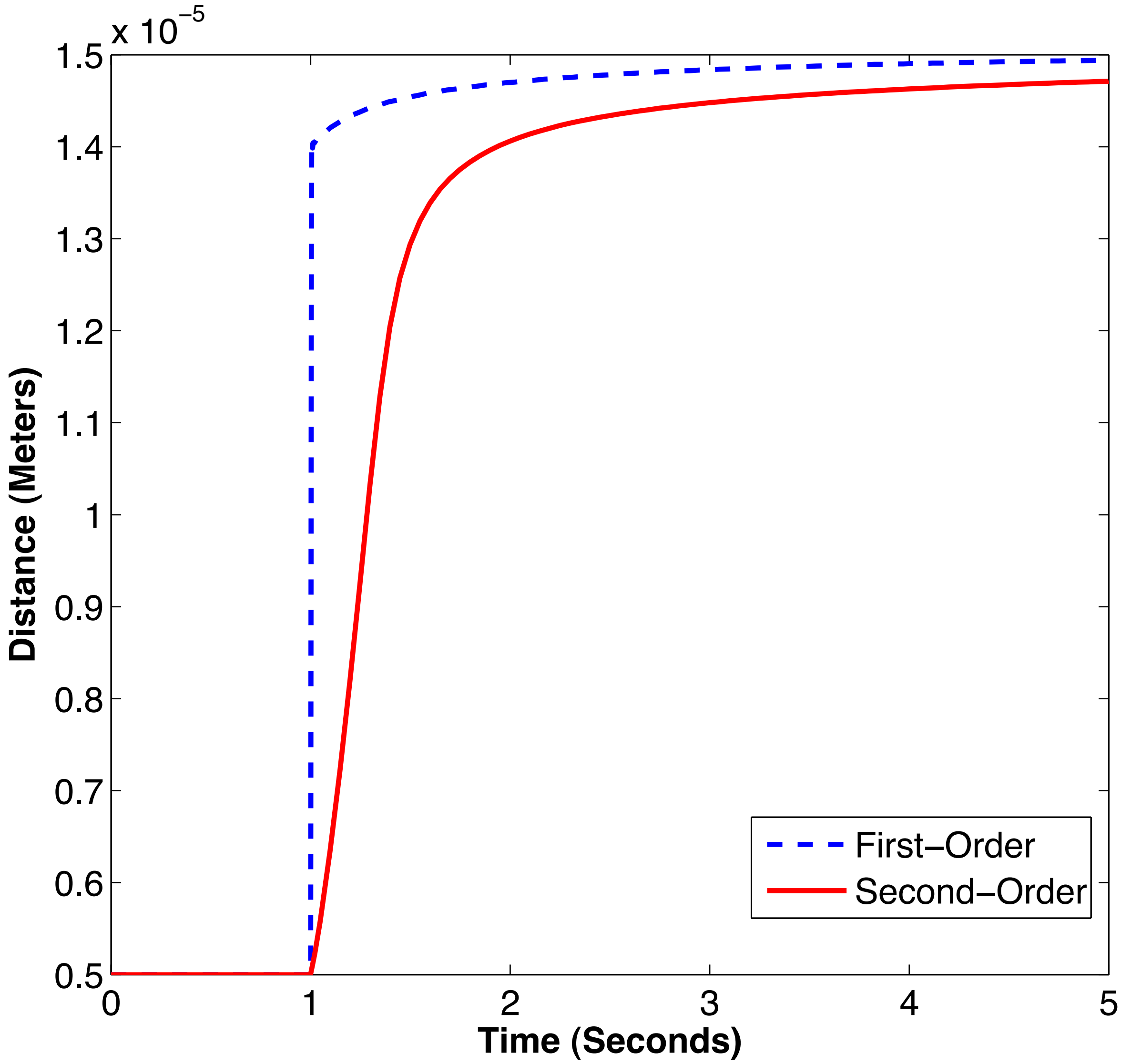

Figure 4.1: Comparison between 1st-order transitional motion model vs. 2nd-order. In the 2nd-order the bead's inertia is included.

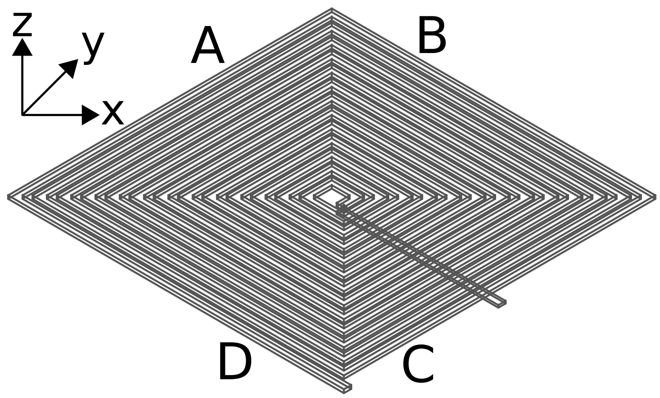

Figure 4.2: Visualization of a 80x80 micron on-coil as used on the chip, in the Cartesian space. A, B, C and D indicate the four sections of the mathematical model.

segment in the coil as derived in [70]. The coil is divided to four sections {A,B,C,D} as shown in Fig. 4.2. The total magnetic field is the sum of all wires in all sections.

4.3 Control Design

Feedback control is widely used in automation and robotic applications to stabilize an actuation task. A feedback system can be described as an output variable (y) which is measured by a sensor and fed back via a controller to be adjusted to reach a desired value. In other words, the output variable (y) is the bead's current location, influenced by a noise source (F_T), is compared to the desired destination of the bead (y_d) and then passed to the controller to adjust the system's actuation parameters, e.g. current through a coil, to move the bead to the desired location. This operation is shown as a block diagram in Fig. 4.3.

Any minute object suspended in a liquid platform experiences Brownian motion. Therefore, the noise source here is best observed as Brownian motion of the bead. This motion is caused by a collection of forces. In this implementation, the main cause of this motion is assumed to be the thermal force and it is considered to be a white Gaussian noise source

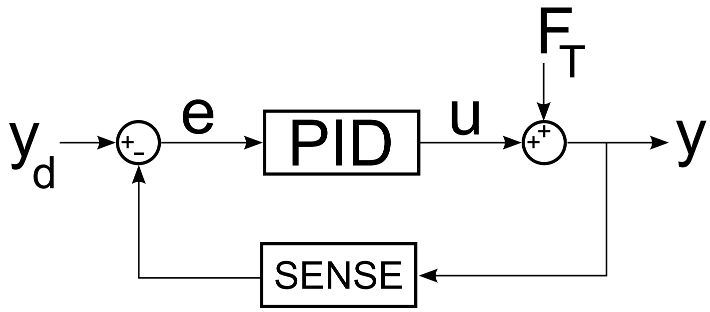

Figure 4.3: Control Strategy for second order bead dynamics.

[11].

Most design methods for controllers require complete models of the dynamic process. The Ziegler-Nichols tuning of PID is adopted here to simplify the approach [69]. Fig. 4.4 shows Ziegler-Nichols tuning of a bead moving from one coil's center to another. A simulation is performed in Fig. 4.5 to show the second-order model of the bead, using Ziegler-Nichols tuning method, while being manipulated between two neighboring coils in the array. The bead doesn't reach its exact final destination due to a tolerance range set by the controller. If the bead escapes that range, due to diffusion, the PID controller will adjust the current though the coil to trap the bead back in place.

Finally, the entire coil array shares a single PID controller to move a bead from one location to the other. Initially the coil array is scanned and calibrated using the on-chip coils. Then the array and the PID controller are programmed to move a bead from a specific location (i.e. row=0,column=0) to another (i.e. row=3,column=3). The PID controller is switched to control the first target coil (i.e. row=1,column=1), then, when the bead is attracted (trapped) there the PID controller is "handed over" to the next coil for the following trapping operation until the bead reaches its final destination. For simplicity, we assume (i) the bead's path is always simple i.e. from a coil's center to another, (ii) there are no obstacles on the surface of the chip to block a bead from reaching its destination. We

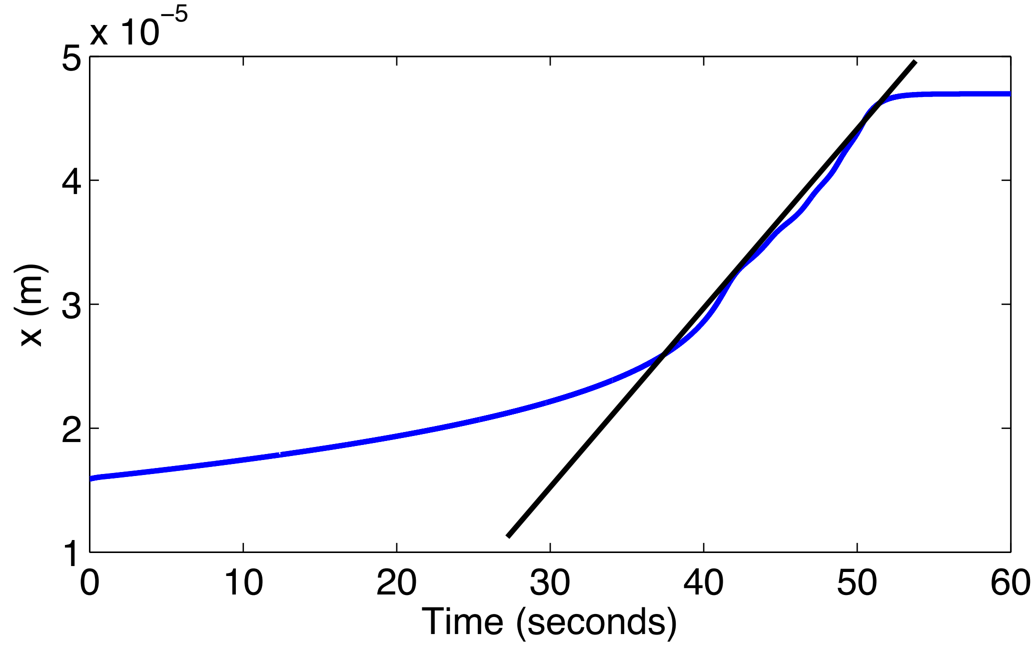

Figure 4.4: Process reaction curve of a bead moving from one coil's center to another, based on a second order system. For the Zieger-Nichols tuning, a tangent is drawn approximately in the inflection point. $T_L = 30sec$ and $a = 39 \cdot 10^{-6}$

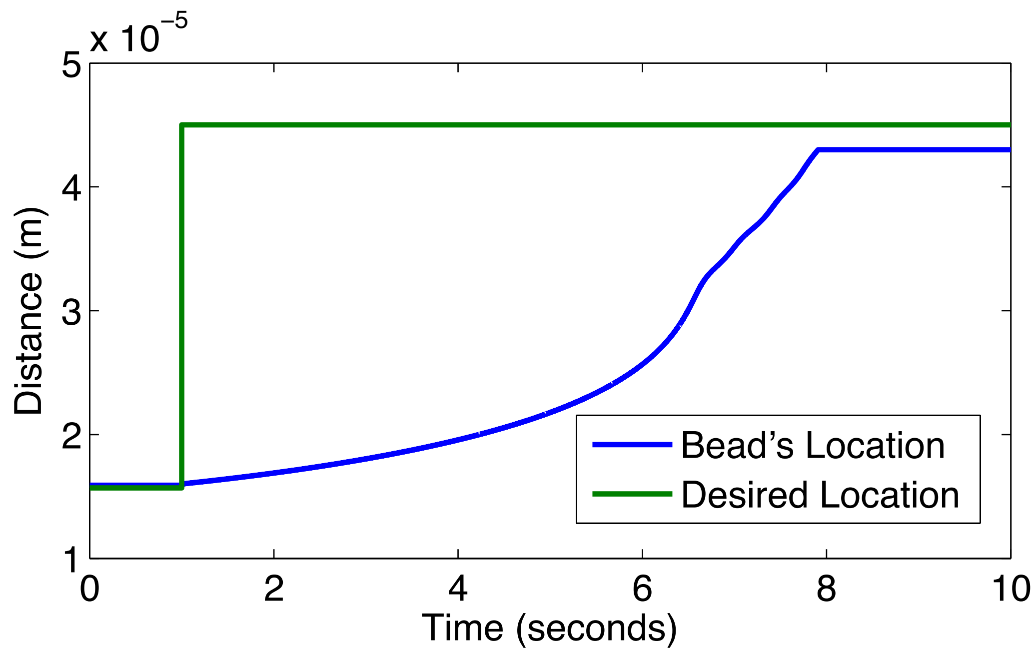

Figure 4.5: Simulation result of the response to a step function at $t = 1$ sec.

plan to report on path finding and obstacle avoidance strategies in a future publication.

4.4 Control Based on Energy Functions

The following modeling considers the magnetized force interaction when a magnetized object of interest (bead) is initially magnetized by a first coil on the array, which then is switched off, followed by a neighboring second coil switching on. Let the induced magnetic moment of the (magnetic) bead by the first coil is given as $M_k - 1 = \frac{1}{\mu_0}\chi V B_k - 1$, where (the physical constants) μ_0, χ, V are respectively the permeability, the susceptibility and volume of the bead due to the spatial coil located at $k - 1$[4]. Thus the generated magnetic potential for a bead which acquired the moment of magnetic field generated from location $k - 1$ and now is acted upon by spatial coil location k is given as the vector dot product of the 2 adjacent magnetic fields.

$$
\begin{aligned}
U &= -\frac{1}{2} M_{k-1} \cdot B_k \\
&= -\frac{1}{2}(\frac{1}{\mu_0}\chi V B_{k-1}) \cdot B_k.
\end{aligned}
\tag{4.12}
$$

As the forces from the spatial coils are generated sequentially, it is thus assumed that the field B_{k-1} is in steady state when the new field B_k is generated from the adjacent coil k. Thus, the translational dynamics of the bead is given as [22, 17, 4]

$$
\begin{aligned}
m\ddot{x} &= F_d + F_m \\
&= (-6a\pi\eta r_B(\dot{x} - v_f)) + \frac{1}{2}\frac{1}{\mu_0}\chi V(\vec{B}_{k-1})\vec{B}_k)
\end{aligned}
\tag{4.13}
$$

We relegate the definition of the (constant, physical) parameters to [4]. For the purpose of control, the equations are expressed in the compact form

$$m\ddot{x} = \Gamma - d\dot{x} + b(\nabla \vec{B}_k)\vec{B}_{k-1}, \tag{4.14}$$

where Γ is a vector determined by the fluid flow, d is a (damping constant) determined by the flow friction to the bead, and the scalar b is signifying scaling of the magnetic force generated. The rotational dynamics of the magnetized bead is expressed compactly in the form

$$I\ddot{\theta} = N_d + N_m = -d_r(\dot{\theta} + \beta\dot{x}) + (B_{k-1} \times B_k), \tag{4.15}$$

where the parameters are compressed physical constants. It is known (theoretically and experimentally) that the rotational dynamics are fast in comparison to the translational dynamics and are often taken to be in the steady state of the induced moments as the bead quickly lines up with the adjacent magnetic field of spatial coil k. As an initial step for analysis, we focus on the translation dynamics with the rotational dynamics already assumed in the steady state.

The energy associated with the translational dynamics are the sum of the potential and kinetic energies as [22]

$$W(x, \dot{x}) = \frac{1}{2}(\dot{x}^T \dot{x}) - \Gamma^T x + U, \tag{4.16}$$

The control signal is the generated magnetic field B_k which is radiating from the spatial coil k and is controlled by the current strength in the coil k. It is noted that the presence of fluidic flow renders the vector Γ non-zero, and with the consideration of the inertia of the bead, the dynamics are non-gradient. Thus methods that exploit the gradient in devising control are not applicable. However, in practice, when the mass of the bead is neglected, the dynamics become gradients and the bead can be steered by the potential surface shaping. The platform array in effect discretize the potential surface spatially and the coil elements of the array define spatial regions of the potential field. Thus, an object can be steered along arbitrary paths along the platform surface. The energy function in (4.16) captures the dynamics of the physical system with control and thus represents the constraint in an optimization setting. In the optimization, one can derive the control sequence that would, e.g., steer a single or a population of beads to form a prescribed probability distribution or profile.

Chapter 5

IC Packaging

5.1 Introduction

All of the components are integrated on the same die and fabricated using standard 0.5μm 3M2P CMOS technology then packaged using standard ceramic packages (shown in Fig. 5.1) or plastic packages (shown in Fig. 5.2). Contrary to other state-of-the-art implementations, our method doesn't need any special post-processing, such as; microfluidic structures to channel or manipulate bio-materials. It is designed to operate as an "open cavity" device where the entire surface of the chip is exposed to the sample or material of interest. This reduces the complexity of the system, makes it cheaper to manufacture, and more portable by eliminating microfluidic overhead and the micro-pumps associated with them. However, it is still possible to add these structures if the targeted applications requires such setup.

Using an open-cavity design introduces new challenges, in which, some are shared with microfluidics. The challenges are: insulating the wire bonds attaching the CMOS die with the ceramic/plastic package, increasing biocompatibility of the die's surface, and maneuvering

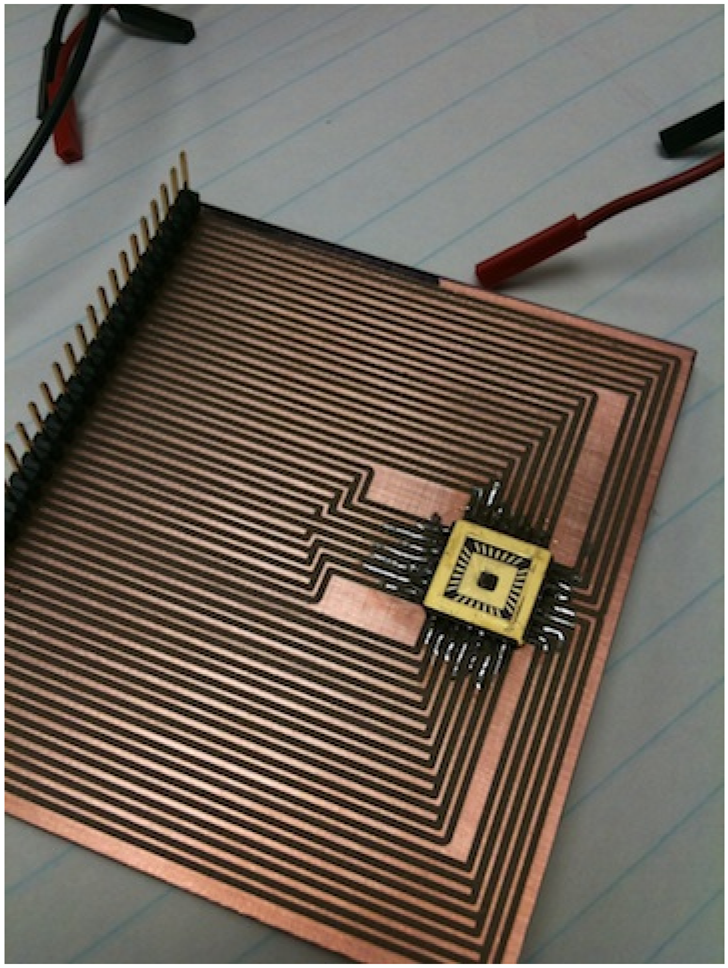

Figure 5.1: Standard ceramic package with PCB board for testing.

the sample of interest on an open surface.

5.2 PDMS

Microfluidic channels are often created using Polydimethylsiloxane (PDMS). This compound is commonly referred to as Silicone. In Bio-MEMs, silicon wafers are used to design channels then PDMS is poured over them and left to cure. Nevertheless PDMS is typically hydrophobic, therefore, its surface is usually exposed to RF Plasma techniques to make it hydrophilic. Once the surface bonds are treated and ready a cover slip (glass) can be placed on the acti-

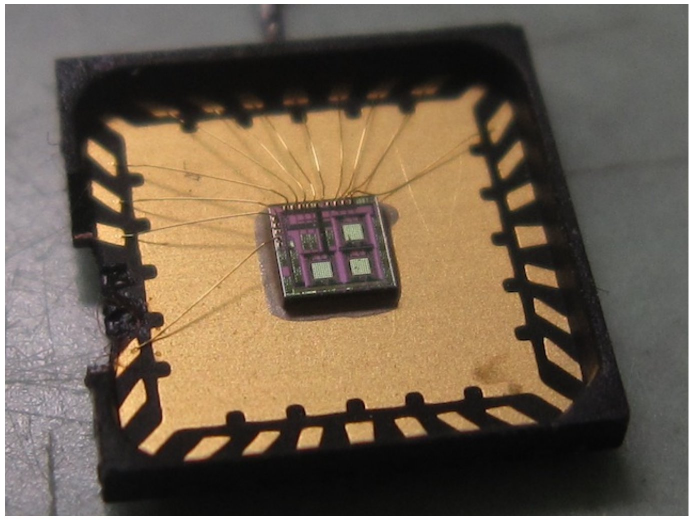

Figure 5.2: Standard plastic package with drainage for testing.

vated side to seal the PDMS channel structure. Thus, creating a micro-fluidic device. These devices are heavily used in lab-on-chip and other rapid analysis platforms.

In this work, we deferred from using PDMS and microfluidic channels to keep the overall design simple. However, we utilized PDMS to insulate the PCB board after assembly. We used a product of SYLGARD 182 SILICONE ELASTOMER KIT from Dowcorning. The mixture was prepared according to the standard protocol described in the datasheet. Then it was poured on the PCB to cover the traces and the soldering points with the header pins. The board was exposed to 100°C for 5 minutes to expedite the curing process.

5.3 Standard

Standard packages were used to reduce the cost and complexity of the final device. Initially a standard DIP40 ceramic package was utilized, however, the package size and the cavity clearance were not suitable for AFM measurements and on-chip biomedical experiments. Second, a standard LCC28 ceramic package was explored, however, the cavity size made the wire-bonding insulation difficult. Third, a standard QFN28 plastic package was used, the size of the cavity was large so both AFM and biological experiments were conducted. The plastic package was easily perforated to create proper drainage, however, the only problem was soldering the package to a standard PCB. Since it is a lead-less package, it required an oven to solder the device on the PCB. Therefore, to reduce the costs, we decided not to use this package. Finally, a standard plastic package LQFP64 was chosen due to its large cavity, long leads, and plastic edges. The low profile cavity made it easy to conduct AFM experiments and create a relatively deep well to contain liquids suitable for lab-on-chip and biomedical experiments.

5.4 Custom

First, a printed circuit board (PCB) is used to mount the CMOS die directly on the edge of an NeuroNexus A-series [71] probe. Then it is placed in a Corning dish under the microscope as in Fig. 5.3. The bonding wires are protected using EpoxyTechnology 353 ND and 353 NDT. The three on-chip arrays are exposed and submerged in Phosphate buffered saline (PBS) solution inside a dish. Then small droplets of magnetic beads are applied on the surface of the chip. The experiment results are discussed in Section 3.2.4.

Second, a LQFP64 package is soldered on a prototype PCB as shown in Fig. 5.4. The size of the PCB is 1.6” x 1.6” x 0.0625”. The PCB board is chosen to fit under the objective of the microscope without requiring much space. The cavity size is 8.402mm x 8.402mm, the depth of the cavity is 0.635mm and the height of the CMOS die is between 0.127 and 0.381mm. The bonding wire arc’s highest point is estimated to be 0.5mm. These values allowed us to create a “well” around the CMOS die that is suitable for lab-on-chip experiments. The

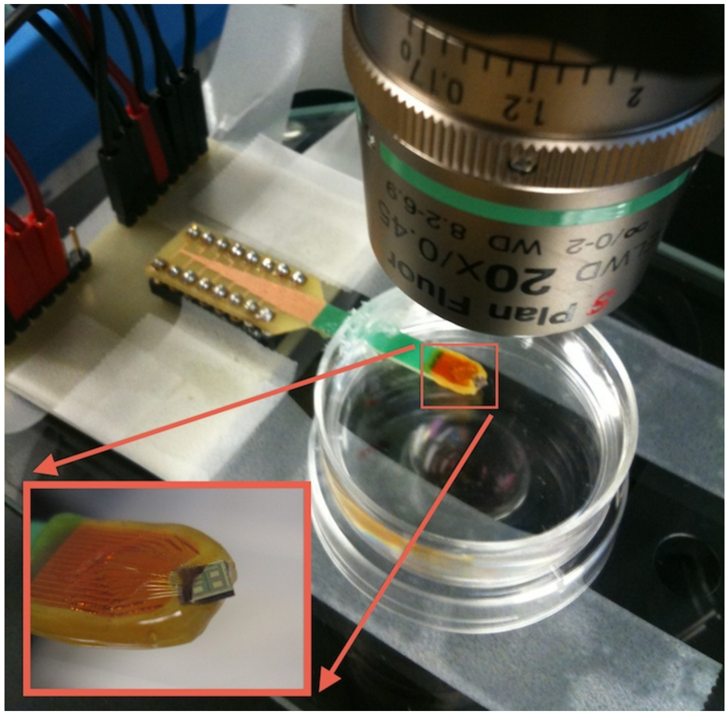

Figure 5.3: Packaging of the CMOS die on top of a PCB probe.

bonding wires were covered with different compounds for insulation. Also, the depth of the cavity is large enough to fill it with liquids and cover it with cover slip. The following subsections discuss the insulating techniques that were using on the CMOS die and the bonding wires.

5.4.1 Wire Bonding Insulation

Simple wire bonding insulation is initially deployed. A product from Loctite (5 minute epoxy) is used and applied to the bonding wires as directed in the user guide. The mixture is applied directly on the bonding wires and manually manipulated to cover the wires and the pads. Fig. 5.5 shows the final insulated bonding wires. The bubbles in the epoxy are a result of rapid mixing before applying the compound. Fig. 5.6 shows a close-up of the epoxy on the die. Three coils in the array were covered because (1) there is a bonding wire close

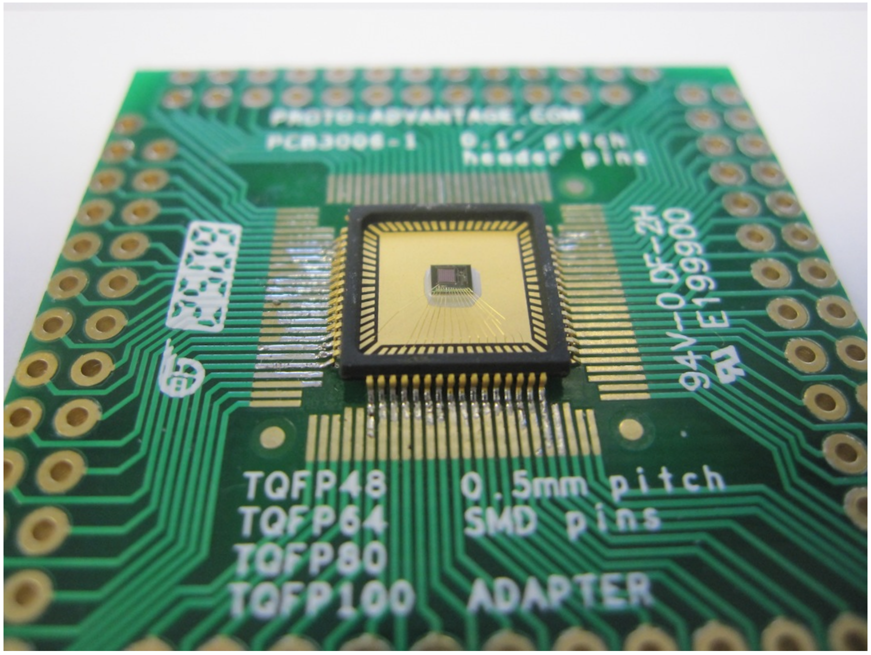

Figure 5.4: Packaged CMOS die on top of a prototype PCB.

to the array (i.e lower left), (2) the epoxy flowed downward to the die because of surface tension.

This chip was functional for approximately 2 months then it failed possibly due to leakage. There were several factors which caused this chip to fail. First, the edges of the CMOS die was regularly exposed to organic chemicals, water, chlorine, as well as UV light. These chemicals caused the edges to chip after numerous exposures. Additionally, extreme UV light exposure changed some of the properties of the semiconductor which eventually changed the threshold voltage on the DC current supplies causing them to fail or operate beyond their capacities.

5.4.2 Enhanced Wire Bonding Insulation

A more sophisticated approached is developed to better insulate the CMOS die and the wire bondings. First, the device is is coated with a 2μm layer of Parylene-C using Specially

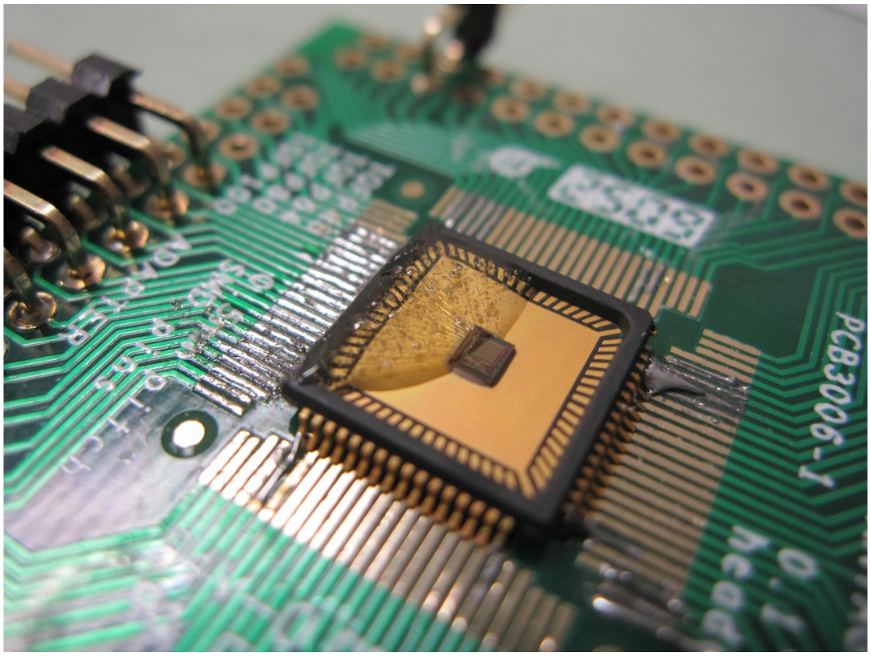

Figure 5.5: Epoxy covering bonding wires.

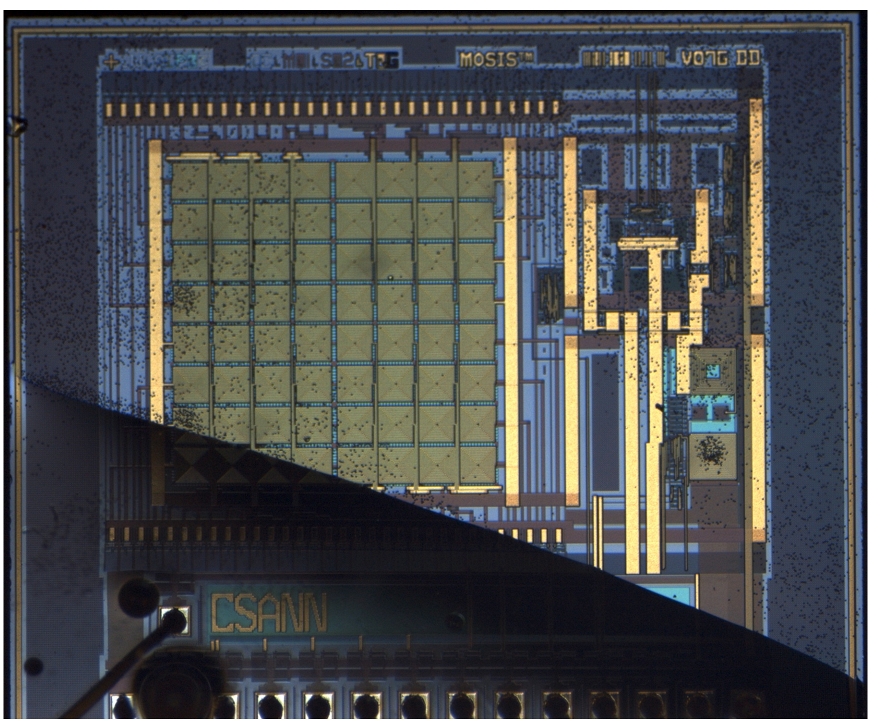

Figure 5.6: Micrograph of CMOS die submerged in fluid with magnetic beads on top. The image illustrates how the epoxy covers part of the die and made 3 coils unusable.

Coating Systems PDS 2010. The deposition time was 1 hour and 31 minutes and 40 seconds. The dimer mass was 3.1348 grams. Second, the bonding wires and the CMOS die were covered by EpoxyTechnology 353 NDT or EpoxyTechnology 353NDT-5. Note that, the viscosity and the thixotropic index of the epoxy are crucial parameters. Choosing a higher viscosity makes the application procedure difficult, and choosing a low viscosity makes it hard to control the flow, thus, covering the entire die. We found that a viscosity (20 RPM and 23°C) between 5000 and 15000 cPs and thixotropic index between 2.1 and 3.6 fit best for this procedure. The procedure of applying the epoxy is described as follows:

- Before mixing the epoxy it might be desirable to add a black pigment to make the color of the epoxy black in order to improve the Epifluorescence microscopy images.
- After mixing the epoxy, a small amount (approximately 5mL) is applied on the bonding wires and around the CMOS die. The entire cavity can be filled if need be. However, it is desirable to keep the epoxy level below the edges of the package.
- The epoxy might start flowing toward the center of the chip. However, the flow should be minimal.
- Dry Nitrogen is slowly blown toward the center of the chip to prevent any slow flow and to create a dam surrounding the die.
- The pressure of the dry nitrogen is slowly increased until the epoxy flows outwards. This creates a dam around the CMOS die. At this point the epoxy should stay at its current position due to its high viscosity.
- The device is placed in preheated vacuum oven (Fisher Scientific Isotemp Vacuum Oven Model 281A) set at 50°C then the vacuum is increased to, approximately, 30 inches of Hg. The epoxy will rise when subjected to such pressure, thus, creating a

Figure 5.7: Top view of chip1 insulation.

larger dam around the CMOS die, which creates the open-cavity needed for cultures, or bead manipulations.

- While the device is still under pressure, the temperature is gradually increased to 100°C to cure the epoxy.
- Once the temperature reaches 100°C. The vacuum is released progressively and the epoxy is watched carefully until it cures. 353NDT cures in 10 minutes under 100°C, however, due to preheating and vacuum pressure, it is highly recommended to reduce that time and carefully watch the amber color of the epoxy.

The results of the aforementioned method is shown in Fig. 5.7 for the first chip and Fig. 5.8 for the second chip. For the first chip, there were debris that prevented the epoxy to flow back. However, for the second chip the epoxy covered the chip properly.

Finally, a standard corning dish is perforated and installed on the PCB board as shown in Fig. 5.9. The dish is insulated with standard 5 minute epoxy to prevent leaks. The same

Figure 5.8: Top view of chip2 insulation.

353NDT epoxy can be also used to seal the dish for better biocompatibility. The die can be attached directly to PCB as shown in the figure or it can be encapsulated with a standard plastic package as previously discussed. If the fabrication house provides free wire-bonding, it might be desirable to use pre-packaged CMOS dies to reduce costs. However, the package leads and thermal package (if present) need to be sealed and insulated accordingly. PDMS can be used, after Parylene-C, coating to submerge the entire PCB while keeping the die and the surface of the package exposed.

The new packaging scheme is built to accommodate neuronal cultures. The dish is filled with media and then small droplets of neuronal embryos are deposited in the center i.e. on top of the chip. The culture is then placed to in an incubator to grow. For more details, see Chapter 6.

Figure 5.9: Final packaged device.

Chapter 6

On-Chip Axonal Initiation and Elongation

6.1 Introduction

Forces have a key role on the growth and development of neurites. For example, external application of forces can double the elongation rates of axons without disrupting the transmission of action potentials or causing axonal thinning. Current methods for applying forces, namely using force calibrated glass needles[72, 73, 74], require excellent manual dexterity, elaborate steps for needle calibration, and continuous observation using fluorescents and bulky optics. This limits both the throughput and the application of this general approach to users with a high degree of training.

In this thesis, we present our contributions toward a fully integrated device suitable for autonomous axonal elongation and monitoring on top of the surface of a standard CMOS substrate. The system consists of a programmable on-chip coil array capable of generating customized electromagnetic forces, in the order of nano Newtons, to synergistically control and manipulate superparamagnetic beads bound to neurites. The electromagnetic forces utilize singular and collaborative maneuvering to elongate axons in 3-Dimensions. Each coil in the array is also time-shared to a cross coupled LC oscillator to sense and detect the spatial position of the bead and the cell body, and thus, scrutinizing the movement and growth of the axon. Therefore, the system previewed provides an automated, high precision, and high-resolution platform to better understand and study neuroregeneration in vitro, which will propel future clinical applications and provides the foundation of techniques needed to wire neuronal circuits using living cells.

6.2 Biophysical Model

The process of axonal elongation has been described to occur in three stages [73]:

- An initial elastic stretch.
- Delayed stretching.
- Constant elongation rates.

This behavior is modeled by Dennerll et al. [73] using three elements where the axon behaves as a spring, a Voigt element, and a dashpot. All elements are connected in series. The combination of the three elements are also called a Burgers element [73]. This model illustrates the effects of tensile stress on the elongation process, but it does not include the axon's distal deformations and/or the effects of adhesions between the axon and the substrate. On the other hand, there is Aeschlimann model, where the axon is modeled as (1) series of springs that stretch elastically and (2) a growth dashpot at the end where the new mass is added during elongation. This model includes the spring and fluid like behaviors

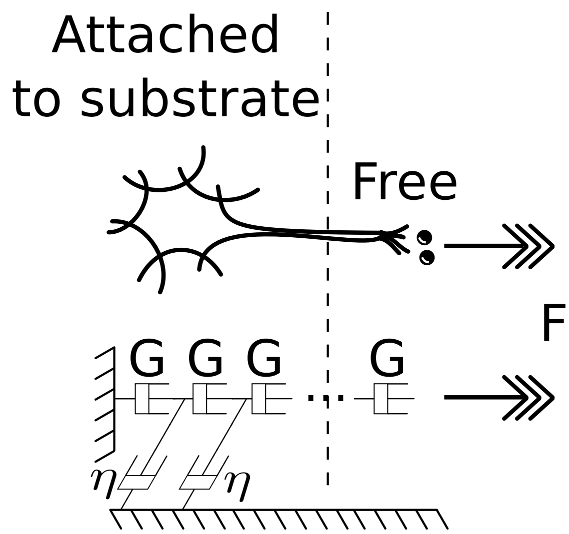

Figure 6.1: The axon is treated as a series of dashpots (G). Where F is the force or tension applied or generated at the growth cone and the friction dashpot η represents the attachments to the substrate.

associated with axonal elongation. Finally O'Toole et al. [75] model axons as a series of dashpots that act like a viscoelastic fluid, as show in Fig. 6.1. They derive a model that includes the effects of tension generation at the growth cone as well as the dissipation along the length of the axon due to adhesions to the substrate.

The force profile of the axon, f, is a function of the distance from the cell body, x, and the length of the axon, $L(t)$. A constant force F_0 applied at the growth cone causes distension at each point along the length. Therefore, the mathematical model [75] for the force is realized in 6.1 and force the axon's length in 6.2.

$$f(x, L(t)) = \frac{F_0 \cosh\left(x\sqrt{\eta/G}\right)}{\cosh\left(L(t)\sqrt{\eta/G}\right)}, \tag{6.1}$$

$$L(t) = \sqrt{\eta/G}\,\operatorname{arcsinh}\left(\sinh\left(L_0\sqrt{\eta/G}\right)\exp\left(\frac{F_0 t}{G}\right)\right), \tag{6.2}$$

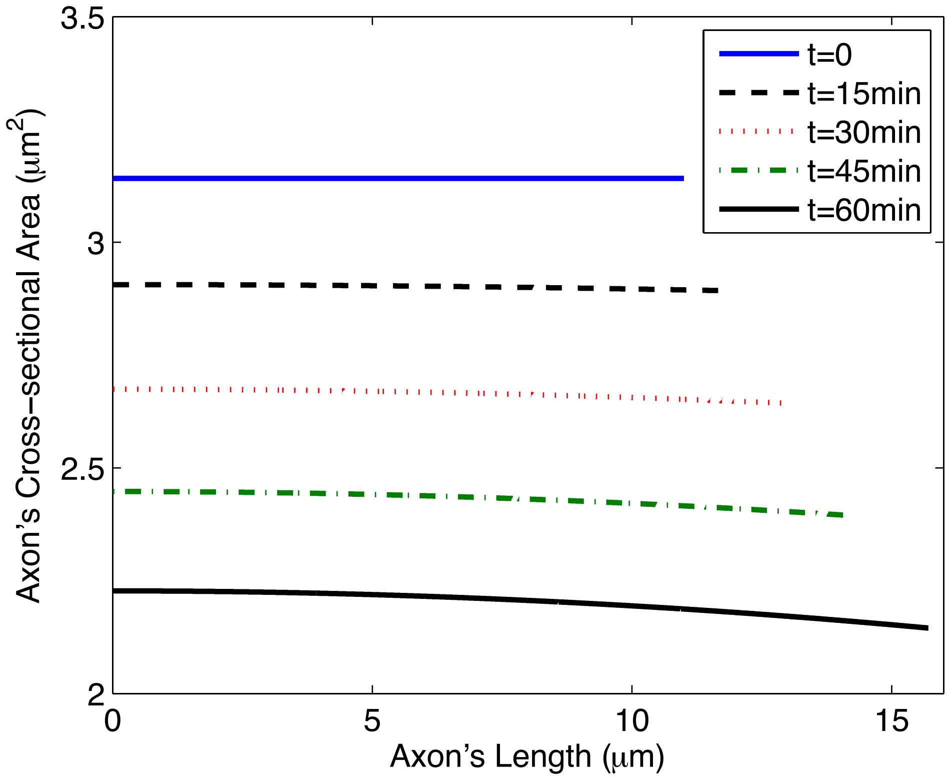

Figure 6.2: Axon's model simulation, without mass addition, shows a 11μm long axon being stretched for 1 hour with 1nN tension force. After 15min the length is 11.9. After 30min the length is 12.97. After 45min the length is 14.22. At the end of the simulation the axon's length is 15.71. A total growth of 4.71 microns. The diameter of the axon is thinning because mass addition was not realized.

where G is the growth dashpot parameter and η is the constant of friction. During the elongation, G varies along with the cross-sectional area while η remains constant. Fig. 6.2 shows a simulation of this model [75] where the axon is 11μm long and a constant force (F_0) of 1nN is applied at the growth cone.

6.3 Experiments

Several lab experiments were conducted to elongate axons using magnetic beads. Initially, we used off the shelf components i.e. electromagnets, and Neodymium magnets. Next, we employed the on-chip micro-coil arrays to manipulate the beads, attach them to axons, and initiate and elongate them.

6.3.1 Neuronal Culture

Drosophila neurons are isolated as discussed in [76]. Cells are grown and imaged at 25C in L-15 medium (Sigma Chemical Co., St. Louis, MO) then supplemented with 0.6% glucose, 1 mM glutamine, 100 U/ml penicillin, 136 mg/ml streptomycin sulfate, 10% fetal calf serum, and N9 growth supplement [77]. This is the standard L-15+N9 based media developed for the culture of chick sensory neurons by Lamoureux et al. [78].

6.3.2 Elongation on Dish

First, we tried to use off-the-shelf components to manipulate magnetic beads to bind and elongate axons. We used a product of APW Company 1.0 Diameter Round Electromagnets EM100 that can hold up to 25 pounds. Three electromagnets were used to maneuver the beads on the dish and were placed around the sample as shown in Fig. 6.3. Initially, all three electromagnetic are switched off then the one on the west is switched on, then the east, then the north. This movie is depicted in a montage in Fig. 6.4. The video is available at (`http://www.msu.edu/~asd1815/videos.html` titled [off_manipulation]). Here, the beads are pointing toward the maximum magnetic field emitted by the electromagnetic. The electromagnets are not lying in the same plane as the sample (dish), therefore, the beads are pointing "upwards" i.e. normal to the dish. This weakens the manipulation forces and causes the distal region of the axon to detach itself from the substrate and retreat.

Moreover, a custom microscope stage was fabricated in order to dip the electromagnets

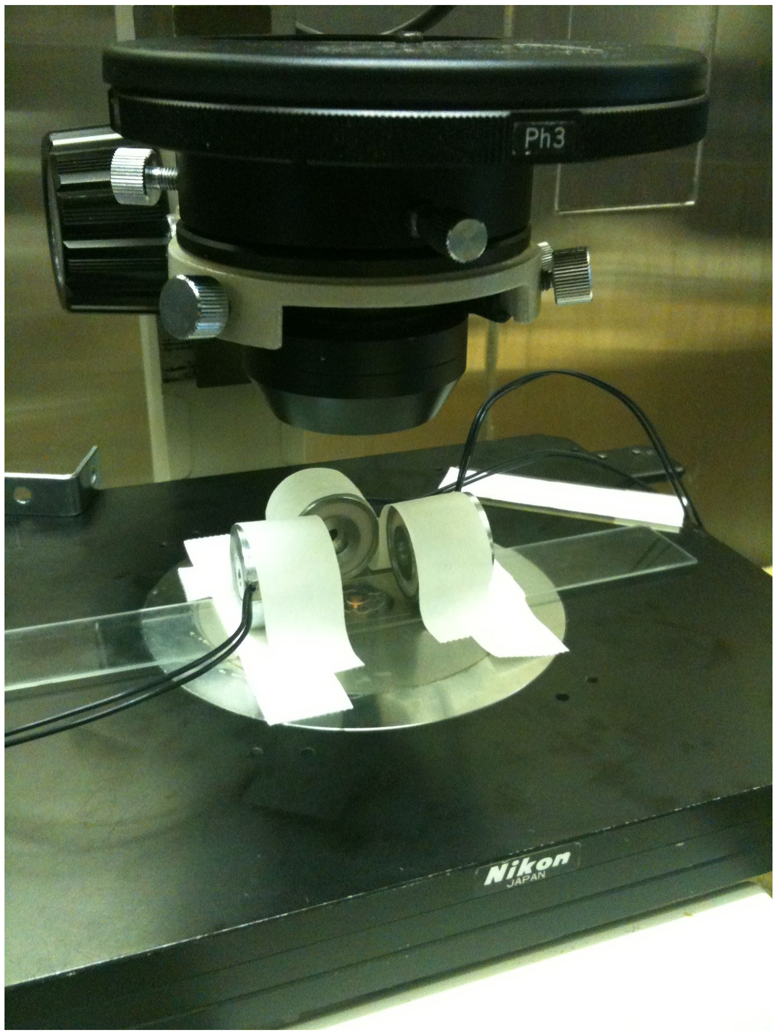

Figure 6.3: Three electromagnetic placed around the sample.

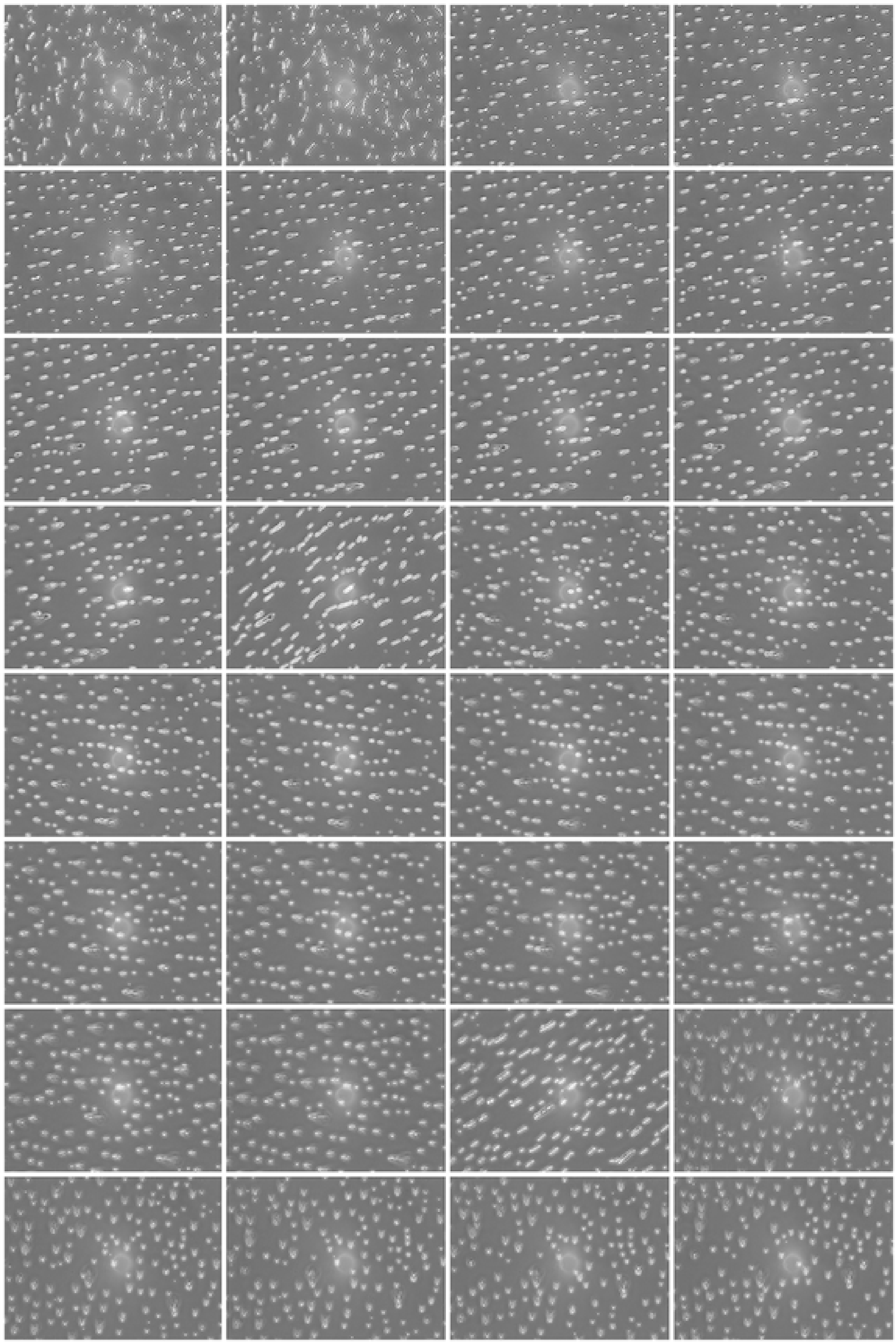

Figure 6.4: Magnetic bead manipulation using three of the shelf electromagnetic.

into the stage for maximum transitional forces. The center of the electromagnet is placed in plane with the culture dish, as depicted in Fig. 6.5. The forces generated from the electromagnet vs. the distance (from its center) is shown in Fig. 6.6. The forces decrease cubically as the distance increases. Additionally, having an electromagnetic close to the sample creates problems when using on stage incubators because the user has to move the magnetic source father away from the sample, thus, reducing the force. Or when larger dishes are used the magnetic forces become weaker for the targets at the center of the dish.

Multiple experiments were conducted to elongate axons using these electromagnets. Two experiments are shown in Fig. 6.7 and Fig. 6.8. The videos are available at (`http://www.msu.edu/~asd1815/videos.html` titled [off_exp1] and [off_exp2]). Phase-microscopy was used to take these photographs. The magnetic beads were manufactured by Invitrogen and were coated with Texas red rabbit HRP (horseradish peroxidase) antibody to facilitate the binding between beads and the axon's membrane. In the first montage, two 1.05 μm beads were attached to an axon. The electromagnetic placed at the south was turned on at maximum power. The magnetic force was not capable of pulling/towing the beads toward the south. In the second, montage 6.8 a single bead was attached to an axon but it couldn't pull it due to the weak force generated by the electromagnet. The bead actually moved along the axon due to mass additions and transport from the cell body.

6.3.3 On-Chip Axonal Elongation

Axonal elongation experiments are implemented on-chip i.e. in vitro to eliminate the limitations seen in the previous section. The limitations are mainly: manipulation resolution, manipulator size, weak magnetic force, and temperature.

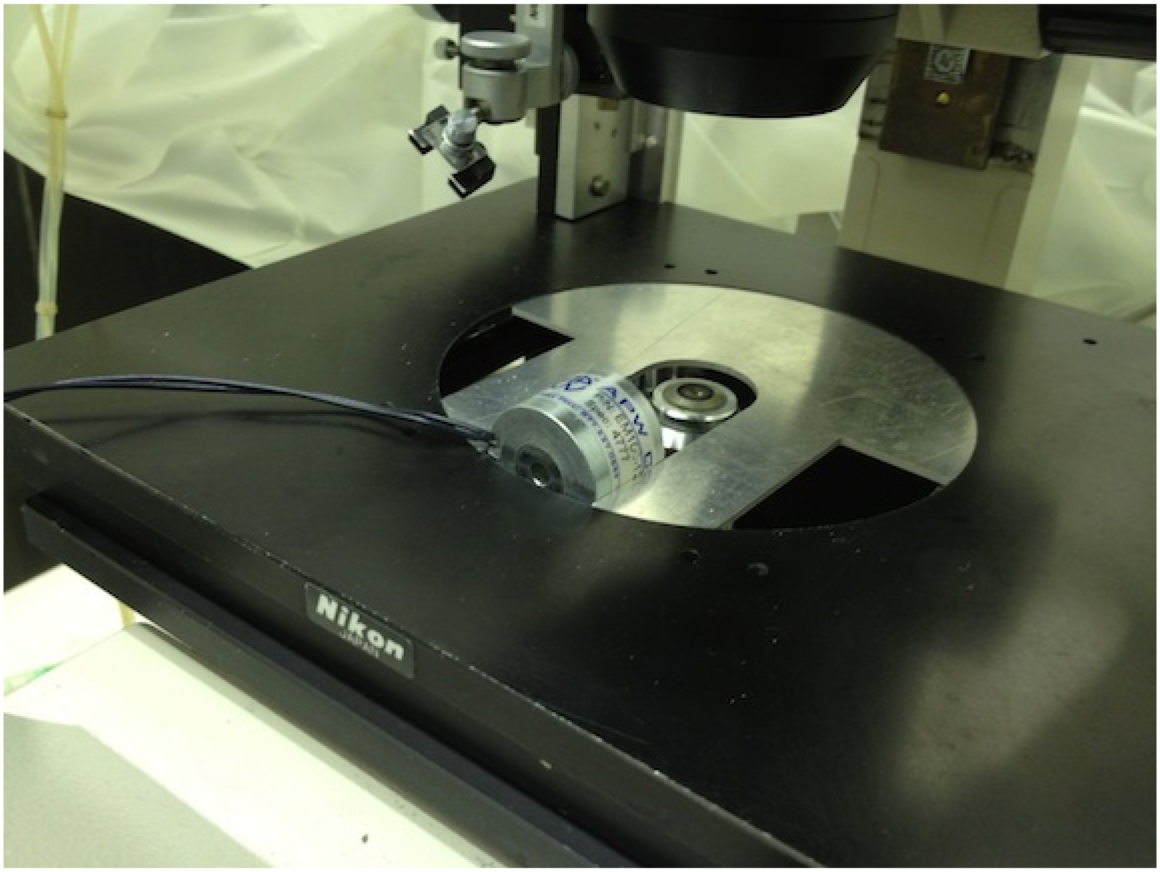

Figure 6.5: Custom stage where the electromagnetic is placed in plane with the sample.

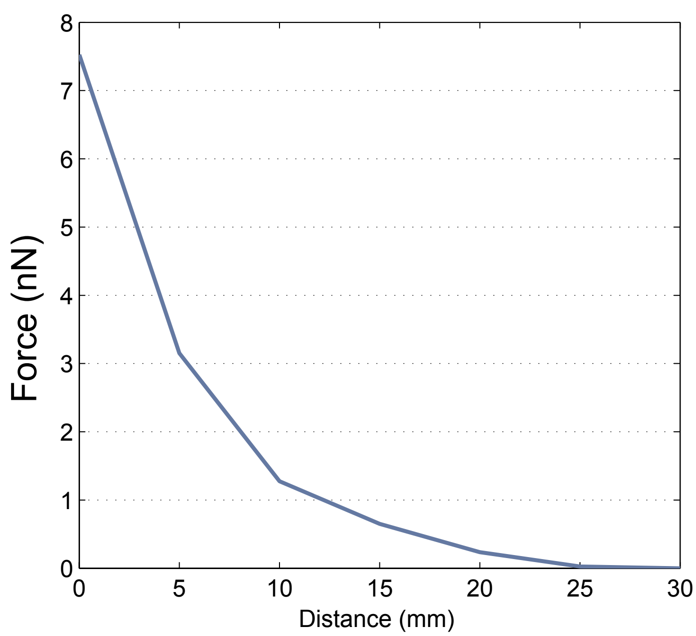

Figure 6.6: Forces generated from electromagnet EM100.

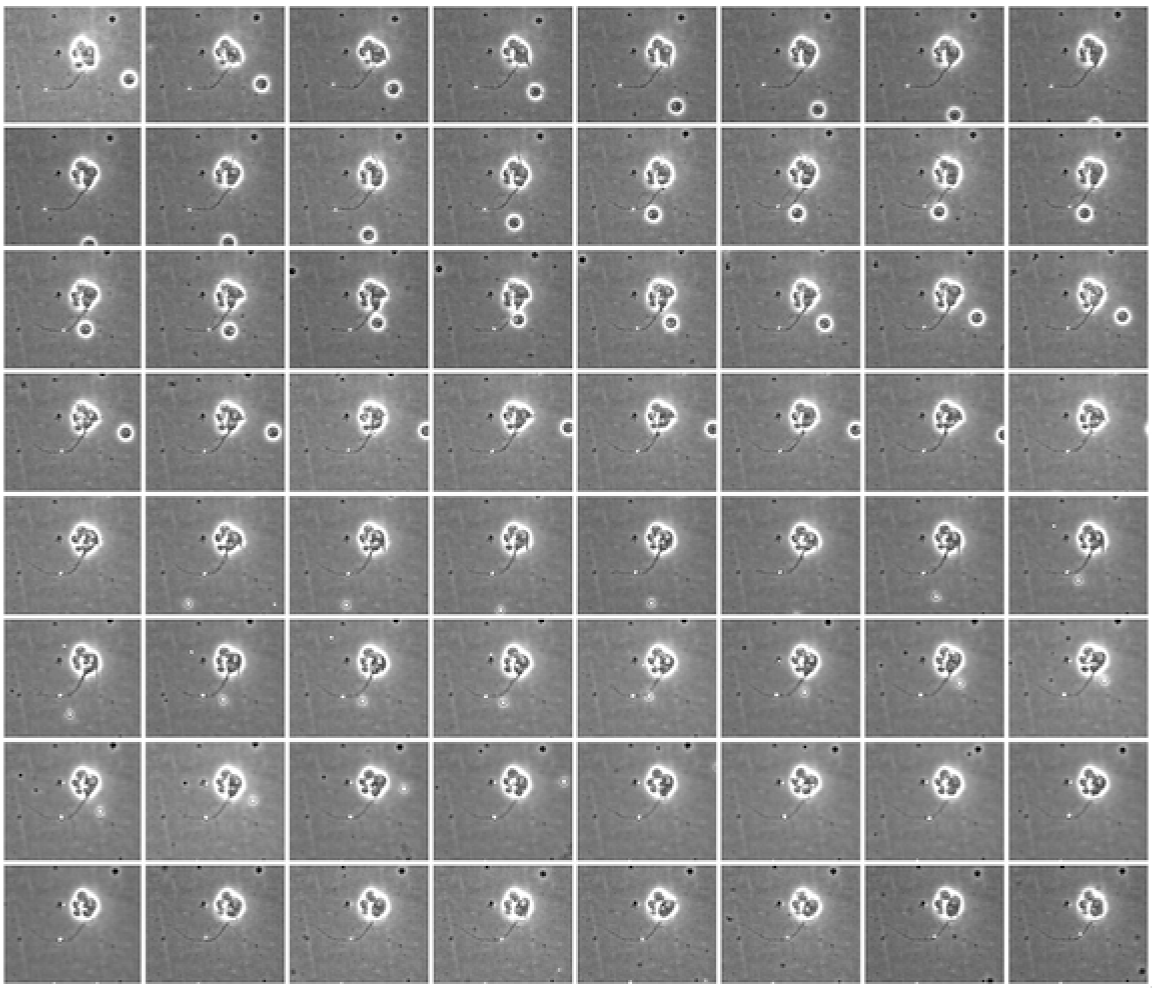

Figure 6.7: Montage of two magnetic beads trying to tow axons grown on a dish.

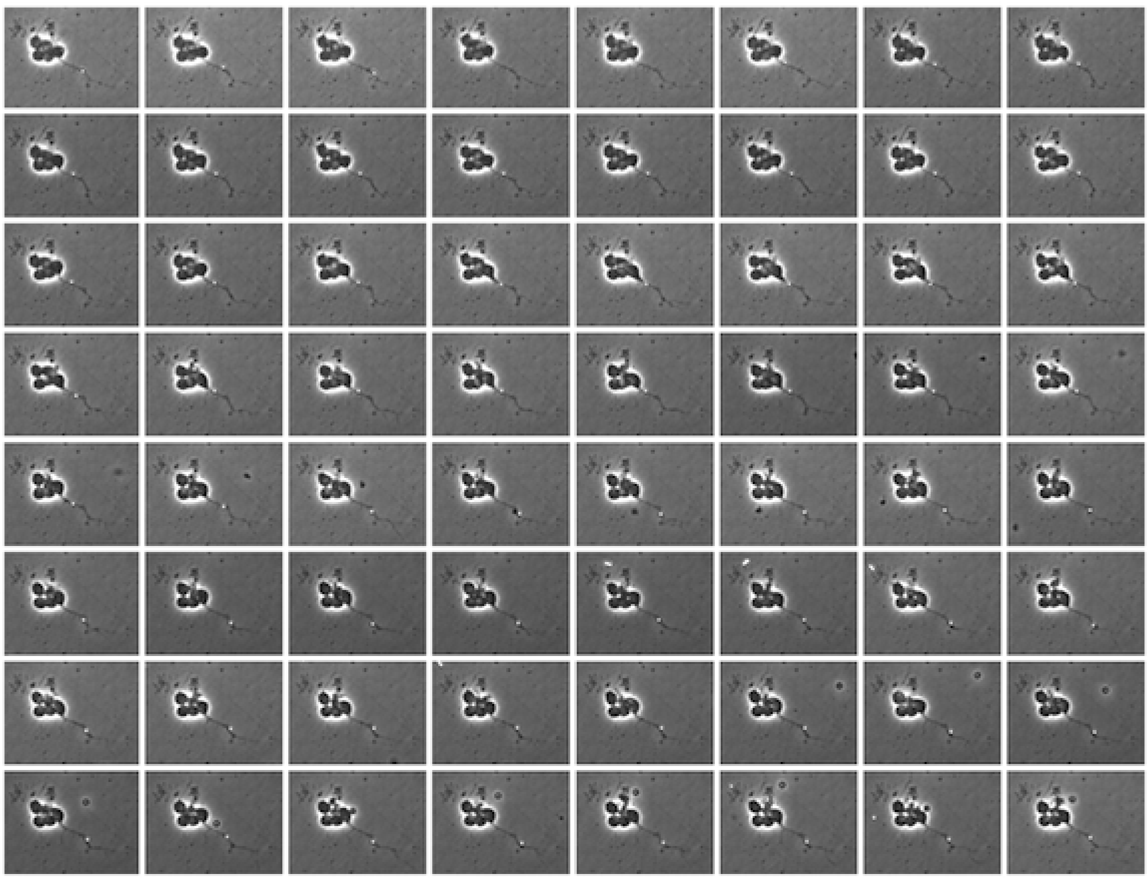

Figure 6.8: Montage of a magnetic bead trying to tow axons grown on a dish. The axon actually pulls the bead toward its body.

The setup is very similar to the previous section, however, instead of using a culture dish we utilized the chips designed and packaged in the previous chapters. The chips were coated and treated with different compounds to increase the growth yield on the silicon substrate. First, for the chips which were previously coated with Parylene-C for insulation and packaging, it was impossible to grow drosophila neurons with the techniques used in sections 6.3.2. This is due to the hydrophobic nature of Parylene-C. As a result, we treated the surface with Poly-L-Ornithine (SIGMA) for 30 minutes prior to platting i.e. placing the embryos on the surface of the chip. Additionally, on some chips we activated the Parylene-C with UV (ultra-violate) light (15 min) and horse/calf serum (3 hours) [79] prior to platting. The result cultures are shown in Fig. 6.9 and 6.10. Based on more than 20 on-chip trials, we estimate that we achieved 20% increase in neuronal growth with these techniques. Epifluorescent microscopy was used to take these photographs. The cultures were pictured 18 hours after platting and they were stained with a dye made by Invitrogen, Vybrant DiI. The staining procedure is similar to what is in the datasheet, however, few modifications were adopted to improve the imaging and the life-span of the axons:

- Dilute 5μL of DiI in 1mL L-15 media. The media has to be supplement free i.e. no serum.
- Remove the media from the culture and add the diluted medium above.
- Incubate for 45 minutes at room temperature.
- Remove the diluted media and carefully wash with PBS 1-3 times.
- Add supplemented L-15 media back again.
- Wait for the cultures to recover (15 minutes) and start imaging and elongation.

In order to elongate the axons, in this experiment we used 2.8μm beads which has more

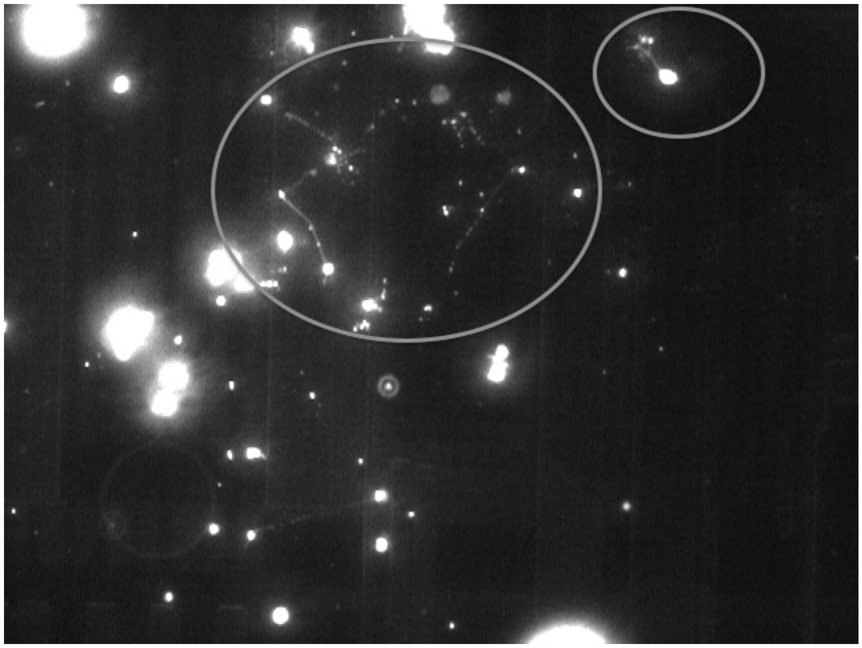

Figure 6.9: A group of neuronal cells grown on a treated surface of Silicon Nitride.

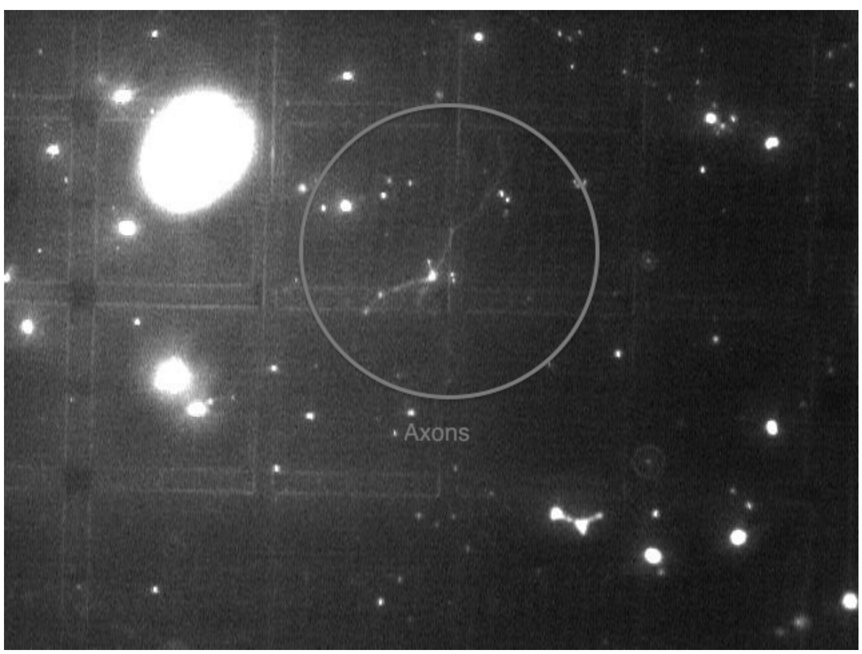

Figure 6.10: A neuronal cell with multiple axon on top of the coil array.

Figure 6.11: On-Chip axonal elongation setup. The open-cavity device makes it easier to deposit small droplets of embryos. The coverslip is placed on top of the plastic package to reduce vibrations and evaporations.

iron content that the previous bead (1.05μm). These beads were coated with the Protein-G then they were deposited as small droplets (5μL) onto the surface of the chip. The package was then sealed with a coverslip, depicted in Fig. 6.11, to improve the clarity and focus by preventing surface tension, evaporation, and vibration. Also, we used the new packaging scheme shown in Fig. 5.9.

Before starting the elongation experiment a grace period (10 min) is observed in order for the beads to bind to the axons and settle at the surface of the chip. The user can use the sensing scheme on-chip to detect where the beads are located or one can use the microscope in the bright-field mode to locate them. If none of the beads were attached to the axons, the user can use the on-chip manipulation mode to move the beads close to an axon to help attaching it to the axon. The grace period (10 min) is observed to create a "good" bond between the bead and the membrane of the axon.

In order to observe the axonal elongation procedure, the beads have to be labeled with a fluorescent dye that is similar, in its wavelength, as the DiI. If the dye is not available then the user has to switch between bright-light filter and fluorescent filters. Fig. 6.12 shows the initial state of the axon before elongation. Fig. 6.13 shows the axon after being elongated with a magnetic bead. The bead is not visible under the fluorescent filter. The experiment was conducted 24 hours after egg lay, and 19 hours after platting. The axon grew 1.7μm in 20 minutes. The length was measured them using imagej[80]. The force of elongation is estimated to be 700pN, based on the previous simulations in section 3.2.4. Additionally, the elongation rate is double the normal rate and it is within the simulated growth for 1nN towing force as shown in Fig. 6.2.

Finally, a second experiment is conducted to initiate a branch out of an axon/bundle. In this experiment the bead is attached to the side of the axon and most likely it caused it to initiate a new branch. Fig. 6.14 shows the initial state of the axon and Fig. 6.15 shows the new branch created. The estimated towing force is 400pN.

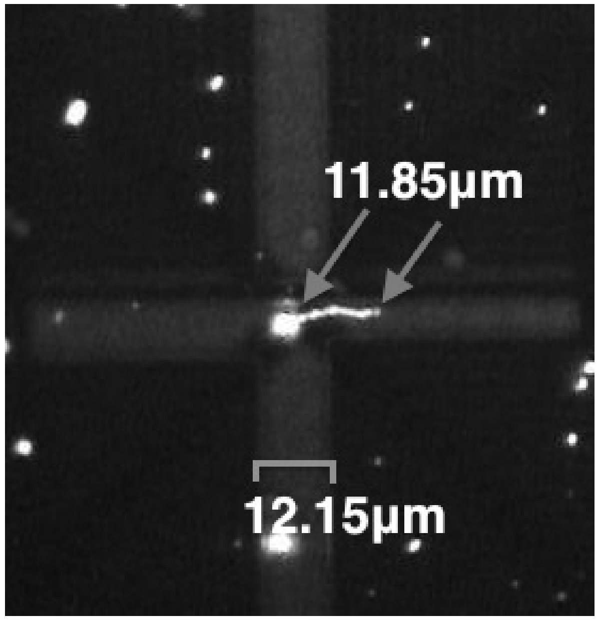

Figure 6.12: On-Chip axonal elongation, initial axon state where the bead is bond to the east of the axon. The bead is not visible under fluorescent filters.

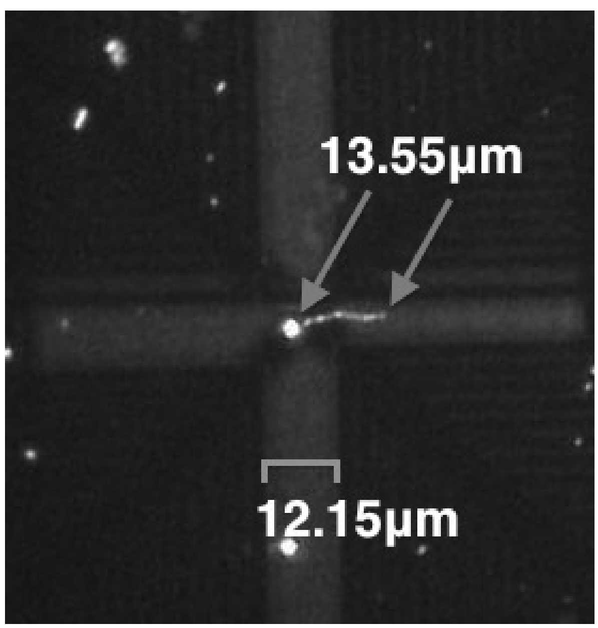

Figure 6.13: On-Chip axonal elongation, final axon state where it elongated 1.7μm in 20 min.

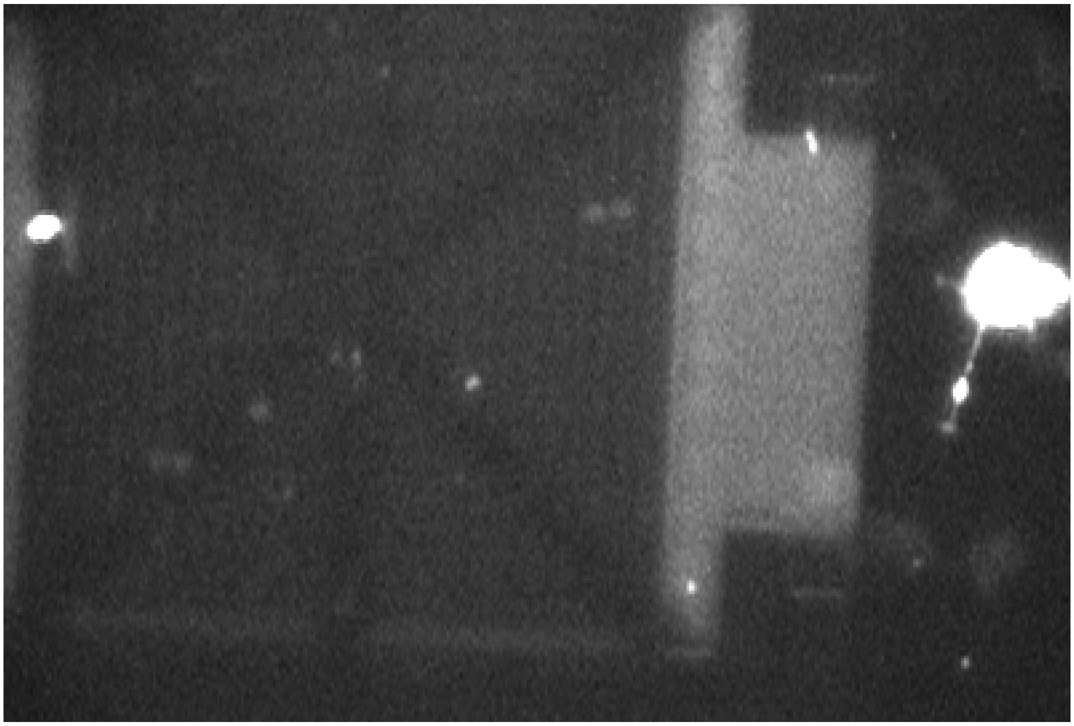

Figure 6.14: On-Chip axonal initiation, initial axon state where the bead is bond to the west of the axon. The bead is not visible under fluorescent filters.

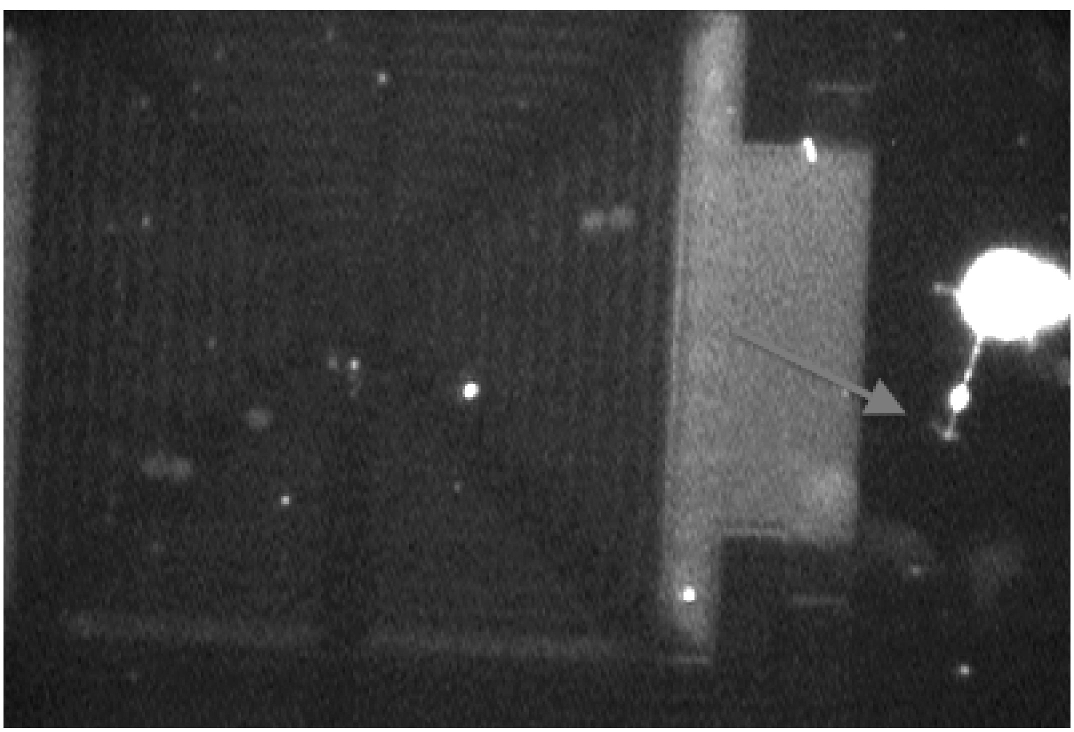

Figure 6.15: On-Chip axonal initiation, final axon state where it branched out after 30 min.

Chapter 7

Conclusions and Future Work

7.1 Summary of Contributions

A lab-on-chip programmable magnetic field generator is implemented, tested, and demonstrated. It can efficiently detect and maneuver biomaterials using magnetic beads without the need of external magnets or special fabrication and packaging processes. Multiple CMOS chips are fabricated and tested for DC/AC actuation and RF sensing. The platforms are suitable for single or collaborative object sensing and manipulation. The designed system features variable magnetic fields, programmable control scheme, different planar inductor designs and array shapes, sizes, and implementations. With these platforms it is possible to dynamically create an unlimited number of magnetic force profiles and contours needed to interact and sense different bio-objects for different bio-applications. Moreover, a novel biomedical application is introduced as a proof of concept. On-chip axonal elongation and initiation is demonstrated by binding magnetic beads to the axons and towing them with localized magnetic forces using the mico-coil array.

7.2 Future Work

Future implementation should include on-chip feedback control to precisely maneuver and manipulate beads. The sensing mechanism used here has to be improved by using a CMOS technology with RF capabilities such as IBM 0.13μm or better. The current 0.5μm CMOS technology suffers in producing inductors with high Q-values. In order to create Q¿5 using the current technology the size of the inductor has to be larger than 400μm which is unfeasible for such applications. Additionally, on-chip temperature sensor should be included to guarantee that the heat generated from the coils does not negatively influence the biological sample on top, and does not alter the oxide layers when using higher currents. Finally, the packaging scheme can be improved to increase reliability by using better insulators and miniaturized 3D printers.

Possible applications for this coil array is (1) micro-robots where the bead can be functionalized to act as a robot controlled by the mico-coil array. These small robots can be used to target specific objects in vitro. (2) On-chip imaging where the array can be used to scan for dielectric material and image their location, the resolution of the imager depends on the size of the coil array and spatial resolution of the LC-CC sensor. A non-uniform gradient can be explored when designing such coil, therefore, any point in the coil can be distinguished based on the shift in frequency at that spatial location. Neighboring coils can be used to correlate the location of the target using the pseudo-parallel scheme introduced in this work. (3) Micro-heaters, the coil array can be used to heat and incubate biological materials by supplying large currents through the coils. A feedback control can be used to adjust/set and program the temperature externally.

APPENDICIES

Appendix A

Maxwell VBS to create and analyze on-chip sensors and actuators for 0.5 CMOS process

```
' Copyright (c) 2011, Faisal T. Abu-Nimeh
' All rights reserved.
' License: BSD 3-Clause License, See license.txt
' CSANN Lab
' Michigan State University
' 80x80 spiral
' 20100803

Dim oAnsoftApp
Dim oDesktop
```

```
Dim oProject
Dim oDesign
Dim oEditor
Dim oModule

' Current in mAmpes
Dim Current
' Outter Spacing Size or Inductor Length
Dim Size

Const boxName = "Box"
Const Units = "um"
Const ViaWidth = 0.6
Const ViaSpacing = 0.6
Const MetalWidth = 1.8
Const MetalSpacing = 1.2
Const SNT = 1  ' values below should be taken from NDA documents
Const SOXT = 1
Const M3T = 1
Const M3M2 = 1
Const M2T = 1
Const M2M1 = 1
Const M1T = 1
```

```
Const M1PLY = 1
Const PLYT = 1
Const TBPSG = 1

Dim N

Current = 40 'mA
Size = 80 ' Length is 80um
N = Int(Size/(2*(MetalWidth+MetalSpacing))) ' Number of Turns
'MsgBox ("loops " & CStr(N))
Set oAnsoftApp = CreateObject("AnsoftMaxwell.
    MaxwellScriptInterface")
Set oDesktop = oAnsoftApp.GetAppDesktop()
oDesktop.NewProject
Set oProject = oDesktop.GetActiveProject
oProject.InsertDesign "Maxwell", "Maxwell Model1", "", ""
Set oDesign = oProject.SetActiveDesign("Maxwell Model1")
Set oEditor = oDesign.SetActiveEditor("3D Modeler")
Set oModule = oDesign.GetModule("BoundarySetup")


oEditor.SetModelUnits Array("NAME:Units Parameter", "Units:=", "um
    ", "Rescale:=", false)
Dim Succ
```

```
' Phase 1 is clockwise winding
' Phase 0 is counter
Succ = createSpiral("metal3_",1,M3T,0)

' via2 -- use last segment position, add length of segment to Y and offset via size from right
oEditor.CreateBox Array("NAME:BoxParameters", _
  "XPosition:=", CStr(Size-((N-1)*MetalSpacing+MetalWidth*(N))+ViaSpacing)&"um", _
  "YPosition:=", CStr(N*(MetalWidth+MetalSpacing)+ViaSpacing)&"um", _
  "ZPosition:=", CStr(-1*(M3M2+M2T))&"um", _
"XSize:=", CStr(ViaWidth)&"um", "YSize:=", CStr(ViaWidth)&"um", "ZSize:=", CStr(M3M2+M2T+M3T)&"um"), _
Array("NAME:Attributes", "Name:=", "via2", "PartCoordinateSystem:=", "Global", "MaterialName:=", "aluminum","SolveInside:=", true)

' bridge
oEditor.CreateBox Array("NAME:BoxParameters", _
  "XPosition:=", CStr(Size-((N-1)*MetalSpacing+MetalWidth*(N)))&"um", _
  "YPosition:=", CStr(N*(MetalWidth+MetalSpacing))&"um", _
```

```
    "ZPosition:=", CStr(-1*(M3M2+M2T))&"um", _
   "XSize:=", CStr(Size/2)&"um", "YSize:=", CStr(MetalWidth)&"um", "ZSize:=", CStr(M2T)&"um"), _
Array("NAME:Attributes", "Name:=", "m2bridge", "PartCoordinateSystem:=", "Global", "MaterialName:=", "aluminum","SolveInside:=", true)

' Create one conducting path
oEditor.Unite Array("NAME:Selections", "Selections:=", "metal3_1,via2,m2bridge"), Array("NAME:UniteParameters", "KeepOriginals:=", false)

' Excite me
'oModule.AssignCurrent Array("NAME:Current1", "Faces:=", Array(658), "Current:=", CStr(Current)&"mA", "IsSolid:=", false, "Point out of terminal:=", false)
'oModule.AssignCurrent Array("NAME:Current2", "Faces:=", Array(40), "Current:=", CStr(Current)&"mA", "IsSolid:=", false, "Point out of terminal:=", true)

' Create Passivation
oEditor.CreateBox Array("NAME:BoxParameters", _
```

```
"XPosition:=", "0um", "YPosition:=", "0um", "ZPosition:=", CStr(-1*(M3M2+M2T+M2M1+M1T+TBPSG))&"um", _
"XSize:=", CStr(Size)&"um", "YSize:=", CStr(Size)&"um", "ZSize:=", CStr(SOXT+M3T+M3M2+M2T+M2M1+M1T+TBPSG)&"um"), _
Array("NAME:Attributes", "Name:=", "SOX", "PartCoordinateSystem:=", _
"Global", "MaterialName:=", "silicon_dioxide", "SolveInside:=", true)
oEditor.CreateBox Array("NAME:BoxParameters", _
"XPosition:=", "0um", "YPosition:=", "0um", "ZPosition:=", CStr(M3T+SOXT)&"um", _
"XSize:=", CStr(Size)&"um", "YSize:=", CStr(Size)&"um", "ZSize:=", CStr(SNT)&"um"), _
Array("NAME:Attributes", "Name:=", "SNT", "PartCoordinateSystem:=", _
"Global", "MaterialName:=", "silicon_nitrate", "SolveInside:=", true)

' Create air box
oEditor.CreateBox Array("NAME:BoxParameters", _
"XPosition:=", CStr(-1*MetalSpacing)&"um", "YPosition:=", CStr(-1*(MetalSpacing+Size))&"um", "ZPosition:=", "-15um", _
```

```
"XSize:=", CStr(Size+2*MetalSpacing)&"um", "YSize:=", CStr(3*Size+2*MetalSpacing)&"um", "ZSize:=", "30um"), _
Array("NAME:Attributes", "Name:=", "air_box", "Color:=", "(200 200 200)", "PartCoordinateSystem:=", "Global", "MaterialName:=", "air", "Transparency:=", 1, "SolveInside:=", true)

' Create non overlapping layers
oEditor.Subtract Array("NAME:Selections", "Blank Parts:=", "air_box", "Tool Parts:=", _
"metal3_1"), Array("NAME:SubtractParameters", "CoordinateSystemID:=", -1, "KeepOriginals:=", _
true)
oEditor.Subtract Array("NAME:Selections", "Blank Parts:=", "SOX", "Tool Parts:=", _
"metal3_1"), Array("NAME:SubtractParameters", "CoordinateSystemID:=", -1, "KeepOriginals:=", _
true)

' Create Setup and Plots
Set oModule = oDesign.GetModule("AnalysisSetup")
oModule.InsertSetup "Magnetostatic", Array("NAME:Setup1", "MaximumPasses:=", 10, "MinimumPasses:=", _
```

```
  2, "MinimumConvergedPasses:=", 1, "PercentRefinement:=", 30, "SolveFieldOnly:=", _
  false, "PercentError:=", 1, "SolveMatrixAtLast:=", true, "UseOutputVariable:=", _
  false, "PreAdaptMesh:=", false, "NonLinearResidual:=", 0.001, "MuNonLinearBH:=", _
  true, "ComputeHc:=", false, "HcNonLinearBH:=", true)
Set oModule = oDesign.GetModule("FieldsReporter")
oModule.CreateFieldPlot Array("NAME:Mag_B1", "SolutionName:=", _
  "Setup1 : LastAdaptive", "QuantityName:=", "Mag_B", "PlotFolder:=", "B", "UserSpecifyName:=", _
  0, "UserSpecifyFolder:=", 0, "IntrinsicVar:=", "", "PlotGeomInfo:=", Array(1, _
  "Volume", "ObjList", 4, "Box1", "metal3_1", "SOX", "SNT"), "FilterBoxes:=", Array( _
  1, ""), Array("NAME:PlotOnVolumeSettings", "PlotIsoSurface:=", true, "CloudDensity:=", _
  0.5, "PointSize:=", 1, "Refinement:=", 0, Array("NAME:Arrow3DSpacingSettings", "ArrowUniform:=", _
  true, "ArrowSpacing:=", 0, "MinArrowSpacing:=", 0, "MaxArrowSpacing:=", 0)))
```

```
Function createSpiral(Name,Phase,Thickness,Z)
   Dim pCount, LeftRight, UpDown, StrX1, StrX2
   pCount=1


   For LeftRight = 0 To (N-1)
      if Phase = 0 then
         StrX1 = CStr(Size-LeftRight*(2*(MetalWidth+MetalSpacing)))
         StrX2 = CStr(Size-LeftRight*(2*(MetalWidth+MetalSpacing))+(MetalWidth+MetalSpacing))
      else
         StrX1 = CStr(Size-LeftRight*(2*(MetalWidth+MetalSpacing))+(MetalWidth+MetalSpacing))
         StrX2 = CStr(Size-LeftRight*(2*(MetalWidth+MetalSpacing)))
      end if
      oEditor.CreateBox Array("NAME:BoxParameters", "XPosition:=", CStr(LeftRight*(MetalWidth+MetalSpacing))&"um", "YPosition:=", CStr(LeftRight*(MetalWidth+MetalSpacing))&"um", "ZPosition:=", CStr(Z)&"um", _
      "XSize:=", StrX1&"um", "YSize:=", CStr(MetalWidth)&"um", "ZSize:=", CStr(Thickness)&"um"), _
      Array("NAME:Attributes", "Name:=", Name & pCount, "PartCoordinateSystem:=", "Global", "MaterialName:=", "aluminum","SolveInside:=", true)
```

```
    pCount=pCount+1
    oEditor.CreateBox Array("NAME:BoxParameters", "XPosition:=",
        CStr(LeftRight*(MetalWidth+MetalSpacing))&"um", "YPosition
        :=", CStr(Size-(LeftRight*MetalSpacing+MetalWidth*(
        LeftRight+1)))&"um", "ZPosition:=", CStr(Z)&"um", _
    "XSize:=", StrX2&"um", "YSize:=", CStr(MetalWidth)&"um", "
        ZSize:=", CStr(Thickness)&"um"), _
    Array("NAME:Attributes", "Name:=", Name & pCount, "
        PartCoordinateSystem:=", "Global", "MaterialName:=", "
        aluminum","SolveInside:=", true)
    pCount=pCount+1
Next

For UpDown = 0 To (N-1)
    if Phase = 0 then
        StrX1 = CStr(UpDown*(MetalWidth+MetalSpacing))
    else
        StrX1 = CStr((UpDown+1)*(MetalWidth+MetalSpacing))
    end if
    oEditor.CreateBox Array("NAME:BoxParameters", "XPosition:=",
        CStr(UpDown*(MetalWidth+MetalSpacing))&"um", "YPosition:=",
         CStr(UpDown*(MetalWidth+MetalSpacing))&"um", "ZPosition:="
        , CStr(Z)&"um", _
```

```
    "XSize:=", CStr(MetalWidth)&"um", "YSize:=", CStr(Size-UpDown*(2*(MetalWidth+MetalSpacing)))&"um", "ZSize:=", CStr(Thickness)&"um"), _
    Array("NAME:Attributes", "Name:=", Name & pCount, "PartCoordinateSystem:=", "Global", "MaterialName:=", "aluminum","SolveInside:=", true)
    pCount=pCount+1
    oEditor.CreateBox Array("NAME:BoxParameters", "XPosition:=", CStr(Size-(UpDown*MetalSpacing+MetalWidth*(UpDown+1)))&"um", "YPosition:=", StrX1&"um", "ZPosition:=",CStr(Z)&"um", _
    "XSize:=", CStr(MetalWidth)&"um", "YSize:=", CStr(Size-UpDown*(2*(MetalWidth+MetalSpacing))-(MetalWidth+MetalSpacing))&"um", "ZSize:=", CStr(Thickness)&"um"), _
    Array("NAME:Attributes", "Name:=", Name & pCount, "PartCoordinateSystem:=", "Global", "MaterialName:=", "aluminum","SolveInside:=", true)
    pCount=pCount+1
  Next
  if (pCount > 1) then
    Boxes = Name & "1"
    pieces = 2
    Do While pieces<pCount
      Boxes = Boxes & ","& Name & pieces
```

```
      pieces=pieces+1
    Loop
    oEditor.Unite Array("NAME:Selections", "Selections:=", Boxes),
        Array("NAME:UniteParameters", "KeepOriginals:=", false)
  End if
  createSpiral = true
End Function

Function createShield(Name, Thickness ,Z)
  Dim pCount, shieldN, numBars
  pCount=1

  shieldN = Int(Size/(MetalWidth+MetalSpacing))
  'MsgBox ("loops " & CStr(shieldN))
  For numBars = 0 To (shieldN -1)
    oEditor.CreateBox Array("NAME:BoxParameters", "XPosition:=", "
        0um", "YPosition:=", CStr(numBars*(MetalWidth+MetalSpacing)
        )&"um", "ZPosition:=", CStr(Z)&"um", _
    "XSize:=", Size&"um", "YSize:=", CStr(MetalWidth)&"um", "ZSize
        :=", CStr(Thickness)&"um"), _
    Array("NAME:Attributes", "Name:=", Name & pCount, "
        PartCoordinateSystem:=", "Global", "MaterialName:=", "
        aluminum","SolveInside:=", true)
```

```
      pCount=pCount+1
   Next
   createShield = true
End Function
```

BIBLIOGRAPHY

BIBLIOGRAPHY

[1] H. Townsend, “Method of magnetic separation,” 1891, US Patent 453,317.

[2] C. T. T. R. H. Sanders, “Process of magnetic separation and apparatus therefore,” 1893, US Patent 499,253.

[3] X. Wetherill, “Method of and apparatus for magnetic separation,” 1896, US Patent 555,792.

[4] H. Lee, Y. Liu, D. Ham, and R. Westervelt, “Integrated cell manipulation system—cmos/microfluidic hybrid,” *Lab on a Chip*, vol. 7, no. 3, pp. 331–337, 2007.

[5] M. Gijs, F. Lacharme, and U. Lehmann, “Microfluidic applications of magnetic particles for biological analysis and catalysis,” *Chemical Reviews*, vol. 110, no. 3, pp. 1518–1563, Mar 2010.

[6] Y. Moser, T. Lehnert, and M. Gijs, “On-chip immuno-agglutination assay with analyte capture by dynamic manipulation of superparamagnetic beads,” *Lab on a Chip*, Jan 2009.

[7] H. Lee, A. Purdon, and R. Westervelt, “Micromanipulation of biological systems with microelectromagnets,” *Magnetics, IEEE Transactions on*, vol. 40, no. 4, pp. 2991–2993, 2004.

[8] H. Lee, Y. Liu, R. Westervelt, and D. Ham, “Ic/microfluidic hybrid system for magnetic manipulation of biological cells,” *Solid-State Circuits, IEEE Journal of*, vol. 41, no. 6, pp. 1471–1480, 2006.

[9] U. Lehmann, M. Sergio, S. Pietrocola, E. Dupont, C. Niclass, M. Gijs, and E. Charbon, “Microparticle photometry in a cmos microsystem combining magnetic actuation and in

situ optical detection," *Sensors and Actuators B: Chemical*, vol. 132, no. 2, pp. 411–417, 2008.

[10] W. Altman, J. Moreland, S. Russek, and V. Bright, "Optimization of spin-valve parameters for magnetic bead trapping and manipulation," *Journal of Magnetism and Magnetic Materials*, vol. 322, no. 21, pp. 3236–3239, 2010.

[11] Z. Zhang, Y. Huang, and C.-H. Menq, "Actively controlled manipulation of a magnetic microbead using quadrupole magnetic tweezers," *Robotics, IEEE Transactions on*, vol. 26, no. 3, pp. 531 – 541, 2010.

[12] A. Rida, V. Fernandez, and M. Gijs, "Long-range transport of magnetic microbeads using simple planar coils placed in a uniform magnetostatic field," *Applied Physics Letters*, 2003.

[13] S.-J. Han, H. Yu, B. Murmann, N. Pourmand, and S. Wang, "A high-density magnetoresistive biosensor array with drift-compensation mechanism," *Solid-State Circuits Conference, 2007. ISSCC 2007. Digest of Technical Papers. IEEE International*, pp. 168 – 594, Feb 2007.

[14] Y. Liu, N. Sun, H. Lee, R. Weissleder, and D. Ham;, "Cmos mini nuclear magnetic resonance system and its application for biomolecular sensing," *Solid-State Circuits Conference, 2008. ISSCC 2008. Digest of Technical Papers. IEEE International*, pp. 140 – 602, Feb 2008.

[15] K. Skucha, P. Liu, M. Megens, J. Kim, and B. Boser, "A compact Hall-effect sensor array for the detection and imaging of single magnetic beads in biomedical assays," *Solid-State Sensors, Actuators and Microsystems Conference (TRANSDUCERS), 2011 16th International*, pp. 1833–1836, 2011.

[16] P.-A. Besse, G. Boero, M. Demierre, V. Pott, and R. Popovic, "Detection of a single magnetic microbead using a miniaturized silicon hall sensor," *Applied Physics Letters*, vol. 80, no. 22, pp. 4199–4201, 2002.

[17] U. Lehmann, M. Sergio, E. Dupont, and E. Labonne, "Actuation and detection of magnetic microparticles in a bioanalytical microsystem with integrated cmos chip," *Nanosystems Design and Technology*, Jan 2009.

[18] H. Wang, Y. Chen, A. Hassibi, A. Scherer, and A. Hajimiri, "A frequency-shift CMOS magnetic biosensor array with single-bead sensitivity and no external magnet," *Solid-State Circuits Conference - Digest of Technical Papers, 2009. ISSCC 2009. IEEE International*, pp. 438–439, 2009.

[19] H. Wang, C. Sideris, and A. Hajimiri, "A frequency-shift based CMOS magnetic biosensor with spatially uniform sensor transducer gain," *Custom Integrated Circuits Conference (CICC), 2010 IEEE*, pp. 1–4, 2010.

[20] H. Wang, S. Kosai, C. Sideris, and A. Hajimiri, "An ultrasensitive CMOS magnetic biosensor array with correlated double counting noise suppression," *Microwave Symposium Digest (MTT), 2010 IEEE MTT-S International*, pp. 616–619, 2010.

[21] F. Abu-Nimeh and F. Salem, "Integrated magnetic array for bio-object sensing and manipulation," *IEEE Biomedical Circuits and Systems Conference*, Nov 2010.

[22] ——, "Electro-magnetic sensing and actuation array on silicon substrate platforms," *IEEE Nanotechnology Materials and Devices Conference*, Oct 2010.

[23] J. Black, "Electromigration—a brief survey and some recent results," *Electron Devices, IEEE Transactions on*, vol. 16, no. 4, pp. 338 – 347, 1969.

[24] C. Hu and Q. Lu, "A unified gate oxide reliability model," *Reliability Physics Symposium Proceedings, 1999. 37th Annual. 1999 IEEE International*, pp. 47 – 51, 1999.

[25] J. Keane, X. Wang, D. Persaud, and C. Kim, "An all-in-one silicon odometer for separately monitoring hci, bti, and tddb," *Solid-State Circuits, IEEE Journal of*, vol. 45, no. 4, pp. 817–829, 2010.

[26] A. Neumann, T. Reske, M. Held, K. Jahnke, C. Ragoß, and H. R. Maier, "Comparative investigation of the biocompatibility of various silicon nitride ceramic qualities in vitro," *Journal of Materials Science: Materials in Medicine*, vol. 15, pp. 1135–1140, 2004.

[27] P. George, A. Lyckman, D. LaVan, A. Hegde, Y. Leung, R. Avasare, C. Testa, P. Alexander, R. Langer, and M. Sur, "Fabrication and biocompatibility of polypyrrole implants suitable for neural prosthetics," *Biomaterials*, vol. 26, no. 17, pp. 3511–3519, 2005.

[28] A. Hoogerwerf and K. Wise, "A three-dimensional microelectrode array for chronic neural recording," *Biomedical Engineering, IEEE Transactions on*, vol. 41, no. 12, pp. 1136 – 1146, 1994.

[29] T. Jochum, T. Denison, and P. Wolf, "Integrated circuit amplifiers for multi-electrode intracortical recording," *Journal of Neural Engineering*, vol. 6, no. 1, p. 012001, Jan 2009.

[30] Philips.com. (2011, Jan) Next generation point-of-care testing. [Online]. Available: http://www.newscenter.philips.com/main/standard/news/backgrounders/2010/20100107_handheld_diagnostics.wpd

[31] A. Bausch, F. Ziemann, A. Boulbitch, and K. Jacobson, "Local measurements of viscoelastic parameters of adherent cell surfaces by magnetic bead microrheometry," *Biophysical Journal*, Jan 1998.

[32] G. P. Hatch and R. E. Stelter, "Magnetic design considerations for devices and particles used for biological high-gradient magnetic separation (hgms) systems," *Journal of Magnetism and Magnetic Materials*, Jan 2001.

[33] Q. A. Pankhurst, J. Connolly, S. K. Jones, and J. Dobson, "Applications of magnetic nanoparticles in biomedicine," *Journal of Physics D: Applied Physics*, vol. 36, no. 13, p. R167, 2003.

[34] X. Zhu, K. Han, and G. Li, "Magnetic nanoparticles applied in electrochemical detection of controllable dna hybridization," *Anal Chem*, vol. 78, no. 7, pp. 2447–9, Apr 2006.

[35] MicroMod. (2010, Dec) Nanomag-d. [Online]. Available: http://www.micromod.de/scripts/p1.asp?sid=567178210&lng=e

[36] Invitrogen. (2010, Nov) Dynal beads myone. [Online]. Available: http://products.invitrogen.com/ivgn/product/35601

[37] Ademtech. (2010, Dec) Bio-adembeads protein g. [Online]. Available: http://www.ademtech.com/products.aspx

[38] A. Wooding, M. Kilner, and D. Lambrick, "Studies of the double surfactant layer stabilization of water-based magnetic fluids," *Journal of colloid and interface science*, vol. 144, no. 1, pp. 236–242, 1991.

[39] A.-H. Lu, E. L. Salabas, and F. Schüth, "Magnetic nanoparticles: Synthesis, protection, functionalization, and application," *Angewandte Chemie International Edition*, vol. 46, no. 8, pp. 1222–1244, 2007.

[40] Y. Jun, J. Lee, and J. Cheon, "Chemical design of nanoparticle probes for high-performance magnetic resonance imaging," *Angewandte Chemie International Edition*, vol. 47, no. 28, pp. 5122–5135, 2008.

[41] H. Lee, D. Ham, and R. M. Westervelt, *CMOS biotechnology.* Springer-Verlag New York Inc, 2007.

[42] C. Seeton, "Viscosity–temperature correlation for liquids," *Tribology Letters*, vol. 22, no. 1, pp. 67–78, 2006.

[43] P. Kennedy, *Flow analysis of injection molds.* Hanser Munich, 1995.

[44] R. Wirix-Speetjens, W. Fyen, K. Xu, J. D. Boeck, and G. Borghs, "A force study of on-chip magnetic particle transport based on tapered conductors," *Magnetics, IEEE Transactions on*, vol. 41, no. 10, pp. 4128–4133, 2005.

[45] E. Verwey, J. Overbeek, and K. van Nes, *Theory of the stability of lyophobic colloids: the interaction of sol particles having an electric double layer.* Elsevier New York, 1948.

[46] B. Derjaguin and L. Landau, "Theory of stability of highly charged lyophobic sols and adhesion of highly charged particles in solutions of electrolytes," *Acta Physicochim. URSS*, vol. 14, pp. 633–52, 1941.

[47] V. Parsegian, *Van der Waals forces: a handbook for biologists, chemists, engineers, and physicists.* Cambridge University Press, 2006.

[48] S. Behrens and D. Grier, "The charge of glass and silica surfaces," *The Journal of Chemical Physics*, vol. 115, p. 6716, 2001.

[49] C. J. Van Oss, M. K. Chaudhury, and R. J. Good, "Interfacial lifshitz-van der waals and polar interactions in macroscopic systems," *Chemical Reviews*, vol. 88, no. 6, pp. 927–941, 1988. [Online]. Available: http://pubs.acs.org/doi/abs/10.1021/cr00088a006

[50] J. Gregory, "Approximate expressions for retarded van der Waals interaction," *Journal of Colloid and Interface Science*, vol. 83, no. 1, pp. 138–145, 1981.

[51] G. Kar, S. Chander, and T. S. Mika, "The potential energy of interaction between dissimilar electrical double layers," *Journal of Colloid and Interface Science*, vol. 44, no. 2, pp. 347 – 355, 1973.

[52] E. Reiner and C. Radke, "Double layer interactions between charge-regulated colloidal surfaces: pair potentials for spherical particles bearing ionogenic surface groups," *Advances in Colloid and Interface Science*, vol. 47, pp. 59 – 147, 1993. [Online]. Available: http://www.sciencedirect.com/science/article/B6V5F-44J18J8-29/2/539f491f25c63a96eba33f9b82331d48

[53] C. Liu, T. Stakenborg, S. Peeters, and L. Lagae, "Cell manipulation with magnetic particles toward microfluidic cytometry," *Journal of Applied Physics*, vol. 105, no. 10, p. 102014, 2009.

[54] M. Jackson, *Molecular and cellular biophysics*. Cambridge University Press, 2006.

[55] R. Tilley, *Understanding solids: the science of materials*. Wiley, 2004.

[56] BangsLabs. (2010, Dec) Polymer microspheres. [Online]. Available: http://www.bangslabs.com/products/polymer_microspheres

[57] H. Kaeslin, *Digital integrated circuit design: from VLSI architectures to CMOS fabrication*. Cambridge University Press, 2008.

[58] T. Lee, *The design of CMOS radio-frequency integrated circuits*. Cambridge University Press, 2004.

[59] A. M. Niknejad. (2010, May) Analysis and simulation of spiral inductors and transformers for ics. [Online]. Available: http://rfic.eecs.berkeley.edu/$\sim$niknejad/asitic.html

[60] Nanosurf. (2011, Jan) The nanosurf easyscan 2 afm. [Online]. Available: http://www.nanosurf.com/index.cfm?content=040220&spr=en

[61] AppNano. (2011, Jan) Technical specifications sheet, probe model: Magt-hm. [Online]. Available: http://www.appnano.com/images/pdfs/MAGT-HM.pdf

[62] L. Li, W. Qureshi, X. Liu, and A. Mason, "Amperometric instrumentation system with on-chip electrode array for biosensor application," *Biomedical Circuits and Systems Conference (BioCAS), 2010 IEEE*, pp. 294 –297, nov. 2010.

[63] F. Abu-Nimeh and F. Salem, "Digital class e power amplifier for the rf band," *Mechatronics and Automation, Proceedings of the 2006 IEEE International Conference on*, pp. 1548 – 1552, May 2006.

[64] P. Cruise, C.-M. Hung, R. Staszewski, O. Eliezer, S. Rezeq, K. Maggio, and D. Leipold, "A digital-to-rf-amplitude converter for gsm/gprs/edge in 90-nm digital cmos," *Radio Frequency integrated Circuits (RFIC) Symposium, 2005. Digest of Papers. 2005 IEEE*, pp. 21 – 24, Jun 2005.

[65] F. Abu-Nimeh and F. Salem, “Cmos integrated electro-magnetic force actuator,” *Circuits and Systems, 2006. MWSCAS '06. 49th IEEE International Midwest Symposium on*, vol. 2, pp. 395 – 398, Jul 2006.

[66] D. Ham and A. Hajimiri, “Virtual damping in oscillators,” in *Custom Integrated Circuits Conference, 2002. Proceedings of the IEEE 2002*, 2002, pp. 213–216.

[67] A. Hajimiri, “Concepts and methods in optimization of integrated LC VCOs,” *Solid-State Circuits, IEEE Journal of*, vol. 36, no. 6, pp. 896–909, 2001.

[68] A. Hajimiri and T. Lee, “Design issues in CMOS differential LC oscillators,” *Solid-State Circuits, IEEE Journal of*, vol. 34, no. 5, pp. 717–724, 1999.

[69] J. Barthel, “Motion Control of Magnetic Beads on a CMOS Chip,” *Unpublished Report*, 2010.

[70] A. Beyzavi and N. Nguyen, “Modeling and optimization of planar microcoils,” *Journal of Micromechanics and Microengineering*, vol. 18, p. 095018, 2008.

[71] NeuroNexus. (2011, Jan) Probe packages. [Online]. Available: http://www.neuronexustech.com/

[72] J. Zheng, P. Lamoureux, V. Santiago, T. Dennerll, R. E. Buxbaum, and S. R. Heidemann, “Tensile regulation of axonal elongation and initiation.” *Journal of Neuroscience*, vol. 11, no. 4, pp. 1117–1125, Apr. 1991.

[73] T. J. Dennerll, P. Lamoureux, R. E. Buxbaum, and S. R. Heidemann, “The cytomechanics of axonal elongation and retraction,” *The Journal of cell biology*, vol. 109, no. 6 Pt 1, pp. 3073–3083, Dec. 1989.

[74] J. Zheng, R. E. Buxbaum, and S. R. Heidemann, “Measurements of growth cone adhesion to culture surfaces by micromanipulation.” *The Journal of cell biology*, vol. 127, no. 6 Pt 2, pp. 2049–2060, Dec. 1994.

[75] M. O'Toole, R. Latham, R. M. Baqri, and K. E. Miller, “Modeling mitochondrial dynamics during in vivo axonal elongation.” *Journal of theoretical biology*, vol. 255, no. 4, pp. 369–377, Dec. 2008.

[76] B. Sicaeros and D. K. O'Dowd, “Preparation of neuronal cultures from midgastrula stage Drosophila embryos.” *Journal of visualized experiments : JoVE*, no. 5, p. 226, 2007.

[77] S. Heidemann, M. Reynolds, K. Ngo, and P. Lamoureux, "The culture of chick forebrain neurons," *Methods in cell biology*, vol. 71, pp. 51–65, 2003.

[78] P. Lamoureux, S. R. Heidemann, N. R. Martzke, and K. E. Miller, "Growth and elongation within and along the axon." *Developmental neurobiology*, vol. 70, no. 3, pp. 135–149, Feb. 2010.

[79] E. Delivopoulos, A. F. Murray, N. K. MacLeod, and J. C. Curtis, "Guided growth of neurons and glia using microfabricated patterns of parylene-C on a SiO2 background." *Biomaterials*, vol. 30, no. 11, pp. 2048–2058, Apr. 2009.

[80] M. Abràmoff, P. Magalhães, and S. Ram, "Image processing with imagej," *Biophotonics international*, vol. 11, no. 7, pp. 36–42, 2004.